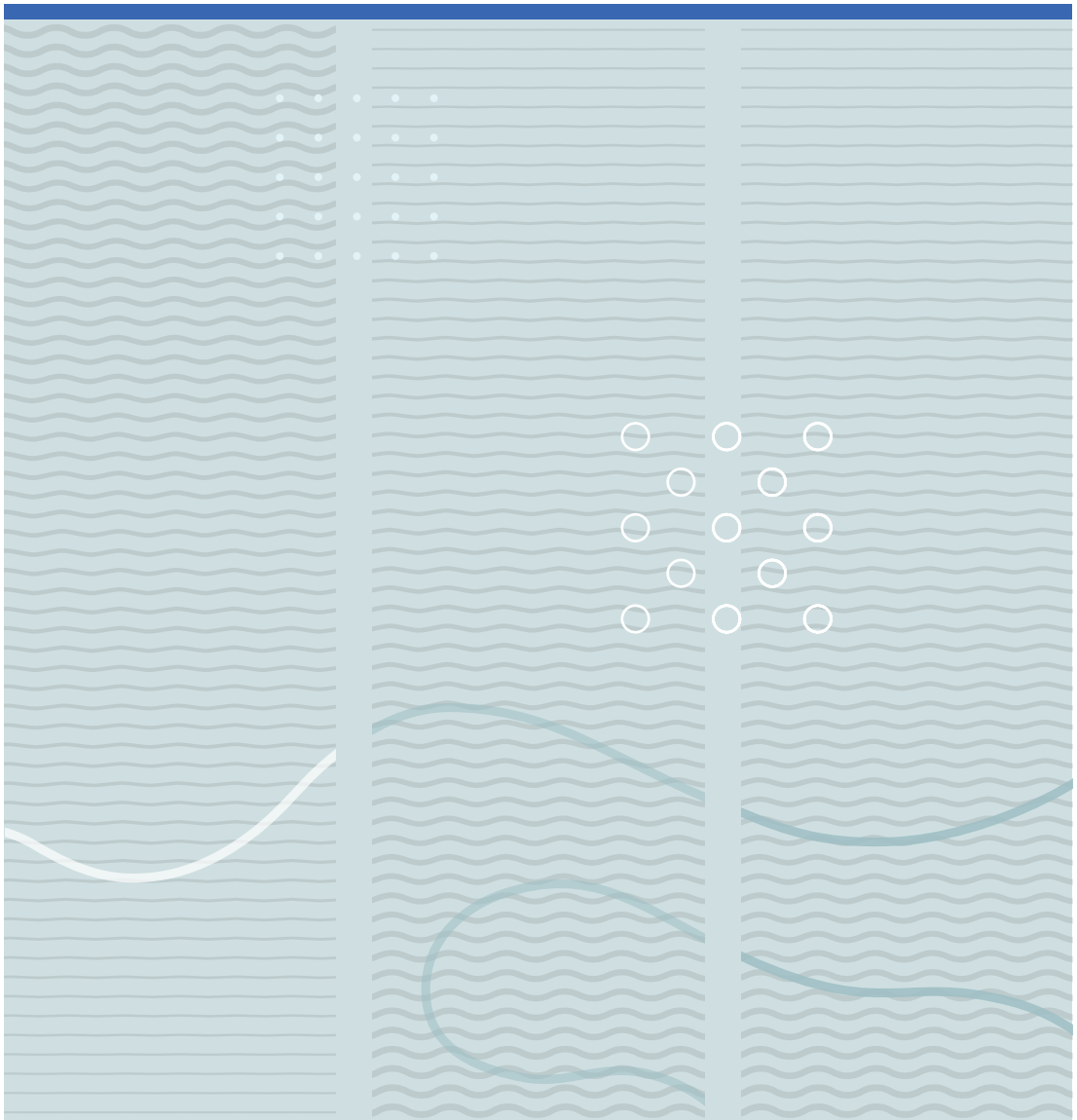


Xiao Fan

Preparation of novel metal oxides/hydroxides materials and their applications in supercapacitors





Xiao Fan

**Preparation of novel metal oxides/hydroxides
materials and their applications in supercapacitors**

A PhD dissertation in
Applied micro- and nanosystems

© Xiao Fan, 2021

Faculty of Technology, Natural Sciences and Maritime Studies
University of South-Eastern Norway
Horten, 2021

Doctoral dissertations at the University of South-Eastern Norway no. 89

ISSN: 2535-5244 (print)

ISSN: 2535-5252 (online)

ISBN: 978-82-7860-468-7 (print)

ISBN: 978-82-7860-467-0 (online)



This publication is licensed with a Creative Commons license. You may copy and redistribute the material in any medium or format. You must give appropriate credit, provide a link to the license, and indicate if changes were made. Complete license

terms at <https://creativecommons.org/licenses/by-nc-sa/4.0/deed.en>

Print: University of South-Eastern Norway

Preface

This thesis is submitted in partial fulfilment of the requirements for the degree of Philosophiae Doctor (PhD) at University of South-Eastern Norway (USN). The thesis is based on the work carried out at Department of Microsystems (IMS) from August 2016 to June 2020. This work is financially supported by the China Scholarship Council (CSC, 201506930018), the Research Council of Norway (RCN, 221860/F60) and the Norwegian Micro- and Nano- Fabrication Facility (NorFab, 245963).

First, I would like to gratefully acknowledge my supervisors, Prof. Xuyuan Chen, Prof. Per Ohlckers and Prof. Einar Halvorsen, who led me for the whole PhD process, for their encyclopedic knowledge, comprehensive guide, thoughtful help, firm trust and kind encouragement. Specially, they always gave me in time feedback and solution when I was confused, even on holiday. It is no doubt that I would never reach the final stage without their support. I also want to thank for assist by Pai, Kang, Chengjun and Yingge, who also work in micro energy team with me, and by Zekija, Thomas, Tayyib, Anh Tuan and Birgitte, who are in charge of the laboratory.

Secondly, I specially appreciate Prof. Muhammad Nadeem Akram, Prof. Tao Dong, Prof. Per Ohlckers and Prof. Terje Finstad (University of Oslo). Through their PhD courses, I broadened my horizon. My gratitude also goes to two PhD advisers Kristin and Aina, other colleagues Ying, Laxma, Yelzhas, Avisek, Zengxing, Fan and Shuai, Embassy of China in Norway and Chinese Service Center for Scholarly Exchange (CSCSE).

Last, my family deserve a particular gratitude. Thank you for providing me a harbour of love. It is a great pity that my departed paternal grandparents and maternal grandfather fail to witness the significant day and I want you to know that I miss you so much.

Thanks everyone in the Assessment Committee and I sincerely wish you enjoy reading it.

Abstract

Supercapacitors, as next-generation efficient, safe and clean energy storage devices with superior power density, fast charge/discharge rate, excellent temperature adaptability and remarkable service life, significantly balance the conventional capacitors and the batteries and have been adopted in many fields. Compared with electric double-layer capacitors, pseudocapacitors can produce a higher specific capacitance to satisfy the ever-growing demand, consequently becoming the research hotspot. Co_3O_4 , $\text{Ni}(\text{OH})_2$ and $\text{Co}(\text{OH})_2$, in view of overwhelming theoretical specific capacitances, modest cost and environmental friendliness, have been extensively recognized as the most promising electrode materials and triggered numerous efforts.

However, currently, the achieved specific capacitances of Co_3O_4 electrodes in previous contributions are still lower than the theoretical value. Besides, the generally accompanying poor rate performances further hinder the application. To address the issue, the hollow Co_3O_4 spheres with high porosity and thin-wall feature were synthesized. The as-fabricated Co_3O_4 electrode delivers a high specific capacitance of 988 F/g at 1 A/g and only 6.4% of its initial value decays at 20 A/g. Via analysis of the formation mechanism of zeolitic imidazolate framework-67, the size adjustment in preparation of hollow Co_3O_4 nanoboxes was obtained, which offers novel perspective and approach for optimization of hollow Co_3O_4 . The hollow Co_3O_4 nanoboxes electrode exhibits large specific capacitances of 1832.7 and 1324.5 F/g at 1 and 20 A/g, respectively.

Recently, the Ni-Co binary hydroxide, which outperforms the single hydroxide thanks to the virtues of stronger layer orientation, increased active sites, reduced resistance and so on, have sparked numerous attentions as a promising route to further enhance the performances of $\text{Ni}(\text{OH})_2$ and $\text{Co}(\text{OH})_2$ based electrodes. Unfortunately, due to undesirable morphology and involved binder, the progress to date is only in partial fulfilment of the requirements of high performance supercapacitors. Aiming at the defect, a morphology-controlled synthesis to grow Ni-Co binary hydroxide on nickel foam directly (binder-free) was proposed, by which excellent overall supercapacitors

performances in terms of specific capacitance (2807 F/g at 1 A/g), rate capability (2222 F/g at 20 A/g) and cycling stability, together with comparable loading mass and facile fabricated method were obtained. In addition, the supercapacitors behaviors of flower-like ZnWO₄, a potential alternative electrode material, were investigated.

Keywords: supercapacitors; pseudocapacitors; Co₃O₄; hollow; thin-wall; size adjustment; Ni-Co binary hydroxide; morphology-controlled; binder-free

List of publications

Journal Papers

Article 1

Fan, X., Sun, Y., Ohlckers, P., & Chen, X. (2019). Porous Thin-Wall Hollow Co_3O_4 Spheres for Supercapacitors with High Rate Capability. *Applied Sciences*, 9(21), 4672. DOI: 10.3390/app9214672

Article 2

Fan, X., Ohlckers, P., & Chen, X. (2020). Tunable Synthesis of Hollow Co_3O_4 Nanoboxes and Their Application in Supercapacitors. *Applied Sciences*, 10(4), 1208. DOI: 10.3390/app10041208

Article 3

Fan, X., Ohlckers, P., & Chen, X. (2020). One-Step and Morphology-Controlled Synthesis of Ni-Co Binary Hydroxide on Nickel Foam for High-Performance Supercapacitors. *Applied Sciences*, 10(11), 3814. DOI: 10.3390/app10113814

Conference Paper

Fan, X., & Chen, X. (2019). Facile synthesis of NFL- ZnWO_4 for pseudocapacitor applications. *MATEC Web of Conferences*, 272, 01005. DOI: 10.1051/matecconf/201927201005

List of abbreviations

1D	one-dimensional
ACs	activated carbons
CE	counter electrode
CNTs	carbon nanotubes
CV	cyclic voltammetry
EDLCs	electric double layer capacitors
EDX	energy-dispersive X-ray
EIS	electrochemical impedance spectroscopy
GCD	galvanostatic charge/discharge
IHP	inner Helmholtz plane
LDH	layered double hydroxide
MOFs	metal-organic frameworks
NF	nickel foam
NMP	n-methyl-2-pyrrolidone
OHP	outer Helmholtz plane
PSCs	pseudocapacitors
PVDF	polyvinylidene fluoride
R_{ct}	charge transfer resistance
RE	reference electrode
RGO	reduced graphene oxide
SC	specific capacitance
SEM	scanning electron microscope
TMO/Hs	transition metal oxides/hydroxides
W	Warburg element
WE	working electrode
XPS	X-ray photoelectron spectroscopy
XRD	X-ray powder diffraction

ZIF zeolitic imidazolate framework

List of Figures and Tables

Figure 1-1 Energy consumption by energy source of United States in 2009 (Copyright U.S. Energy Information Administration).

Figure 1-2 Energy consumption by energy source of United States in 2019 (Copyright U.S. Energy Information Administration).

Figure 1-3 Publications of supercapacitors indexed by Web of Science Core Collection (2009 to 2019).

Figure 1-4 Ragone plots of conventional capacitors, supercapacitors and batteries [23] (Copyright 2014 Elsevier).

Figure 1-5 Representative applications of supercapacitors: (a) energy storage type street light, (b) power supply for wind turbine pitch, (c) high power crane, (d) cold start of heavy vehicle, (e) energy recovery system, and (f) electrical vehicles.

Figure 1-6 Models of EDL: (a) Helmholtz model, (b) Gouy-Chapman model, and (c) Stern model [39] (Copyright 2009 The Royal Society of Chemistry).

Figure 1-7 (a) Rectangular curves in CV test and (b) triangular plots in GCD measurement for EDL capacitance [47] (Copyright 2017 The Authors of Ref. 47).

Figure 1-8 Schematic diagram of EDLCs [48] (Copyright 2018 Elsevier).

Figure 1-9 Types of pseudocapacitive mechanisms: (a) underpotential deposition, (b) redox, and (c) intercalation [51] (Copyright 2014 The Royal Society of Chemistry).

Figure 1-10 Schematic CV for a MnO_2 electrode [57] (Copyright 2008 Nature Publishing Group).

Figure 1-11 (a) Crystallite size effect of LiCoO_2 [65] (Copyright 2007 American Chemical Society) and (b) CV curves of Ni(OH)_2 [66] (Copyright 2013 Macmillan Publishers Limited).

Figure 1-12 Schematic diagram of PsCs [48] (Copyright 2018 Elsevier).

Figure 1-13 SEM images of the (a) wood carbon monolith [73] (Copyright 2011 Elsevier), (b) fullerene-like carbon decorated CNTs network [74] (Copyright 2017 Elsevier), (c)

graphene material [83] (Copyright 2009 American Chemical Society), and TEM image of the (d) RGO sample [84] (Copyright 2010 Elsevier).

Figure 1-14 HRTEM image of the (a) hydrous RuO₂ nanodots [87] (Copyright 2004 The Electrochemical Society) and TEM image of the (b) highly porous structured MnO₂ [89] (Copyright 2011 American Chemical Society).

Figure 1-15 SEM images of the (a) Co₃O₄ nanowires [90] (Copyright 2014 WILEY-VCH Verlag GmbH & Co. KGaA), (b) Co₃O₄ nanorods [91] (Copyright 2017 Elsevier), (c) 3D-nanonet hollow structured Co₃O₄ [96] (Copyright 2014 American Chemical Society), and (d) hollow Co₃O₄ nanowires [97] (Copyright 2011 The Royal Society of Chemistry).

Figure 1-16 SEM images of the (a) Ni(OH)₂ nanospheres [66] (Copyright 2013 Macmillan Publishers Limited), (b) Ni(OH)₂ nanosheets [99] (Copyright 2014 Elsevier), (c) Ni-Co binary hydroxide microspheres [113] (Copyright 2012 The Royal Society of Chemistry), and (d) flower-like Ni-Co binary hydroxide [102] (Copyright 2015 Elsevier).

Figure 2-1 Schematic illustration of three-electrode configuration.

Figure 3-1 (a) XRD patterns and (b) EDX spectrum of Co₃O₄, XPS spectra of Co₃O₄: (c) Co 2p and (d) O 1s, SEM images of (e) precursors and (f) Co₃O₄.

Figure 3-2 (a) CV curves and (b) corresponding SCs, (c) discharge curves and (d) corresponding SCs, (e) EIS plot and (f) cycling performance of Co₃O₄ electrode.

Figure 3-3 XRD patterns of Co₃O₄ (-1,-2,-3).

Figure 3-4 SEM images of (a) ZIF-67-1, (b) ZIF-67-2, (c) ZIF-67-3, (d) Co-LDH-1, (e) Co-LDH-2, (f) Co-LDH-3, (g) Co₃O₄-1, (h) Co₃O₄-2, and (i) Co₃O₄-3.

Figure 3-5 (a) CV curves at 5 mV/s and (b) discharge curves at 1 A/g of Co₃O₄ (-1,-2,-3) electrodes, (c) CV curves at different scan rates and (d) discharge curves at different current densities of Co₃O₄-2 electrode.

Figure 3-6 (a) SCs based on GCD tests, (b) Nyquist plots and (c) enlarged view of high frequency region of Co₃O₄ (-1,-2,-3) electrodes, (d) equivalent circuit, and (e) cycling performance of Co₃O₄-2 electrode.

Figure 3-7 SEM images of samples at Ni/Co ratios of (a) bare NF, (b) 9:1, (c) 7:3, (d) 5:5, (e) 3:7, and (f) 1:9.

Figure 3-8 XRD patterns of $\text{Ni}_{1-x}\text{Co}_x(\text{OH})_2$.

Figure 3-9 XPS spectra of $\text{Ni}_{0.5}\text{Co}_{0.5}(\text{OH})_2$: (a) survey spectrum, (b) Ni 2p, (c) Co 2p, and (d) O 1s.

Figure 3-10 (a) CV curves at 2 mV/s and (b) GCD curves at 1 A/g of $\text{Ni}_{1-x}\text{Co}_x(\text{OH})_2$ electrodes, (c) CV curves at different scan rates and (d) GCD curves at different current densities of $\text{Ni}_{0.5}\text{Co}_{0.5}(\text{OH})_2$ electrode.

Figure 3-11 (a) SCs based on GCD tests of $\text{Ni}_{1-x}\text{Co}_x(\text{OH})_2$ electrodes, (b) Nyquist plots and (c) enlarged view of high frequency region of $\text{Ni}_{0.7}\text{Co}_{0.3}(\text{OH})_2$, $\text{Ni}_{0.5}\text{Co}_{0.5}(\text{OH})_2$ and $\text{Ni}_{0.3}\text{Co}_{0.7}(\text{OH})_2$ electrodes, (d) equivalent circuit, and (e) cycling performance of $\text{Ni}_{0.5}\text{Co}_{0.5}(\text{OH})_2$ electrode.

Figure 3-12 (a) SEM image, (b) XRD patterns, XPS spectra: (c) Zn 2p, (d) W 4f and (e) O 1s, (f) discharge curves and (g) corresponding SCs of flower-like ZnWO_4 .

Table 1-1 Main characteristics of conventional capacitors, supercapacitors and battery.

Table 2-1 Main chemicals in this work.

Table 2-2 Main experimental instruments and equipments in this work.

Table 3-1 SC and rate performance of Co_3O_4 based electrode materials.

Table 3-2 SCs at low and high current densities of Co_3O_4 based electrode materials.

Table of contents

1 Introduction	1
1.1 Overview of supercapacitors	2
1.2 Energy storage mechanism.....	5
1.2.1 EDLCs.....	5
1.2.2 PsCs	8
1.3 Current state of the art for the electrode materials	11
1.3.1 Carbon based materials	11
1.3.2 TMO/Hs.....	13
1.4 Research focus	17
2 Experimental details	21
2.1 Chemicals	21
2.2 Instruments and equipments	22
2.3 Material characterizations.....	22
2.4 Electrochemical measurements	23
3 Summary of main research results	27
3.1 Overview	27
3.2 Porous thin-wall Co_3O_4 spheres for supercapacitors.....	28
3.2.1 Sample preparation	28
3.2.2 Material characterizations	28
3.2.3 Supercapacitors behaviors.....	30
3.2.4 Discussion.....	31
3.3 Tunable synthesis of hollow Co_3O_4 nanoboxes	33
3.3.1 Sample preparation	33
3.3.2 Material characterizations	33
3.3.3 Supercapacitors behaviors.....	35
3.3.4 Discussion.....	37
3.4 Morphology-controlled synthesis of Ni-Co binary hydroxide	38
3.4.1 Sample preparation	38
3.4.2 Material characterizations	38

3.4.3 Supercapacitors behaviors.....	41
3.4.4 Discussion.....	43
3.5 Flower-like ZnWO ₄ for supercapacitors.....	43
3.5.1 Sample preparation	43
3.5.2 Material characterizations and supercapacitors behaviors	44
4 Conclusion and future work	47
References	49
Article I	63
Article II	75
Article III	89
Article IV	105

1 Introduction

With the rapid development of industry, the consumption of traditional energy sources such as natural gas, coal and petroleum explodes [1-4]. For example, in 2018, the consumption of petroleum has already exceeded 100 million barrels per day (data from Organization of the Petroleum Exporting Countries). The non-renewable energy sources confront with depletion and consequent energy crisis have become an unavoidable problem all over the world. Meanwhile, undeniably, the strong dependence on traditional energy sources also results in a series of serious problems like pollution, global warming and even geopolitical concerns, which significantly restricts the further development of global economy and modern society [5-8].

Therefore, developing renewable energy sources to alternate or supplement the non-renewable energy sources, further assuaging the challenge in sustainable development of energy sources, is extremely imperious. The United States was taken as an example. The share of total of renewables increased to 11% in 2019, while in 2009, the renewables only accounted for 8%, as displayed in Figure 1-1 and Figure 1-2, respectively. The renewables mainly focus on hydropower, wind, biomass, solar and geothermal. Obviously, owing to the intermittent nature, it is difficult to utilize the renewable energy source directly [9-12]. Hence, developing efficient energy storage devices or systems, ensuring stable and continuous energy supply, is also a prime goal.

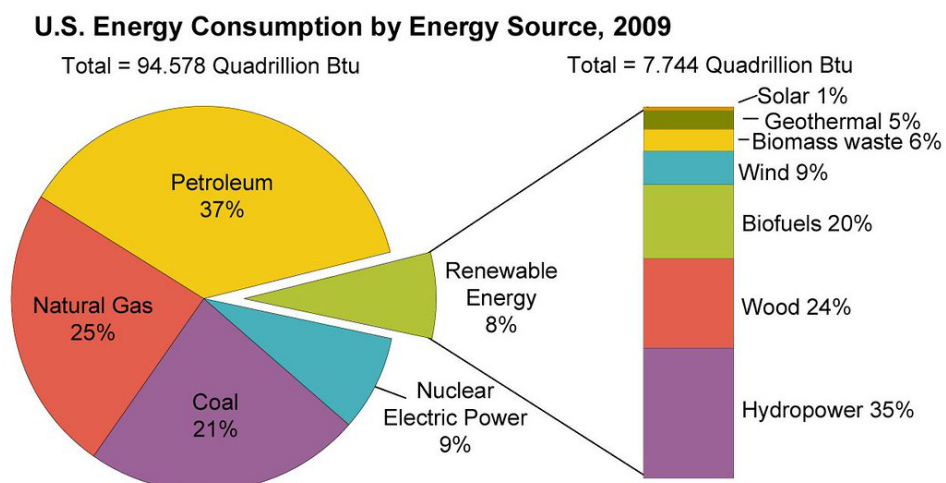


Figure 1-1 Energy consumption by energy source of United States in 2009 (Copyright U.S. Energy Information Administration).

U.S. primary energy consumption by energy source, 2019

total = 100.2 quadrillion British thermal units (Btu)

total = 11.4 quadrillion Btu

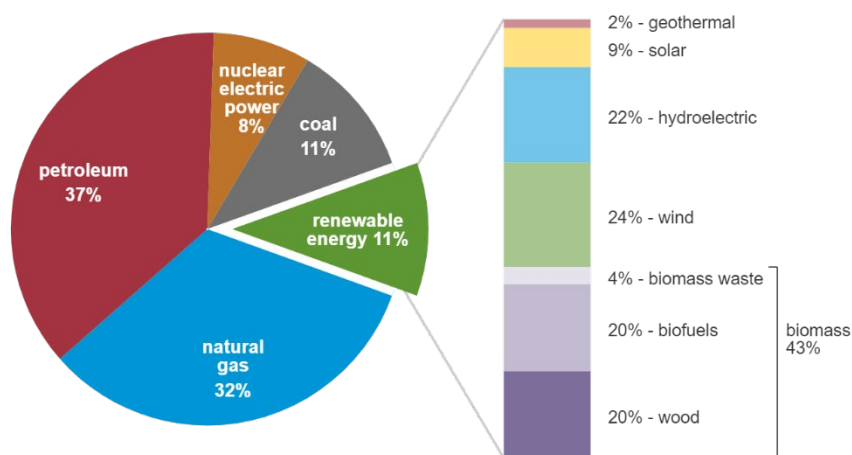


Figure 1-2 Energy consumption by energy source of United States in 2019 (Copyright U.S. Energy Information Administration).

1.1 Overview of supercapacitors

Supercapacitors, as next-generation energy storage devices, significantly balance the conventional capacitors and the batteries and attract numerous attentions in the past decade [13-22]. Only in 2019, the papers of supercapacitors indexed by Web of Science Core Collection were over 4600, as proven by Figure 1-3.

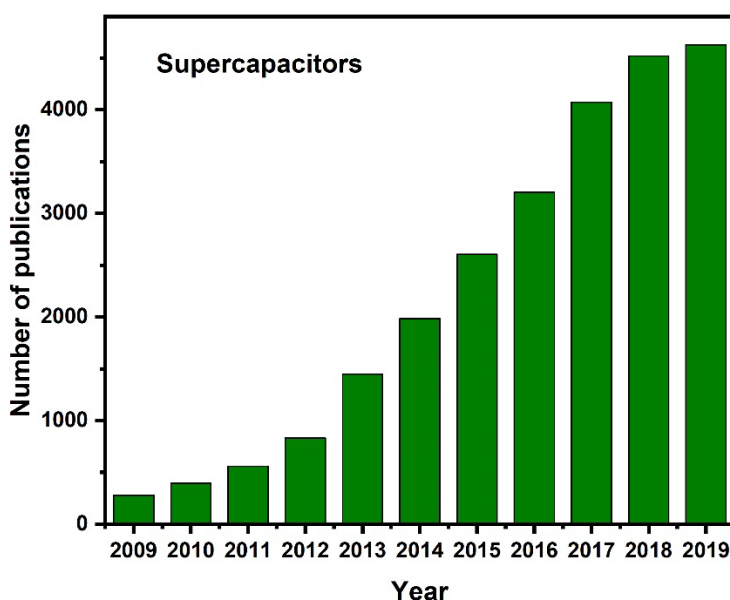


Figure 1-3 Publications of supercapacitors indexed by Web of Science Core Collection (2009 to 2019).

As seen in Figure 1-4, the power density of supercapacitors is higher than that of batteries while the energy density of supercapacitors is higher than that of conventional capacitors [23]. Apart from those features, supercapacitors also deliver many unparalleled advantages which are pivotal for industrial mass production and widespread commercial applications. First, supercapacitors can be charged and discharged in very short time (second or minute level), which is impossible for batteries [24,25]. The second noteworthy point is the working temperature. As a Nordic country, Norway has a long winter with cold temperature. In some areas, the period of minimum temperature below $-10\text{ }^{\circ}\text{C}$ even are up to 5 months (data from Norwegian Meteorological Institute). When temperature is below $0\text{ }^{\circ}\text{C}$, in most cases the discharge capacity of batteries reduce sharply, while supercapacitors can still display high performance at $-40\text{ }^{\circ}\text{C}$ [26-29]. Last, we pay attention to the cycle life. Benefited from the energy storage mechanism, the service life of supercapacitors can beyond 10,000 and electrode swelling (often occurs in batteries) is neglectable [30-33]. Table 1-1 summarized the main characteristics of conventional capacitors, supercapacitors and battery.

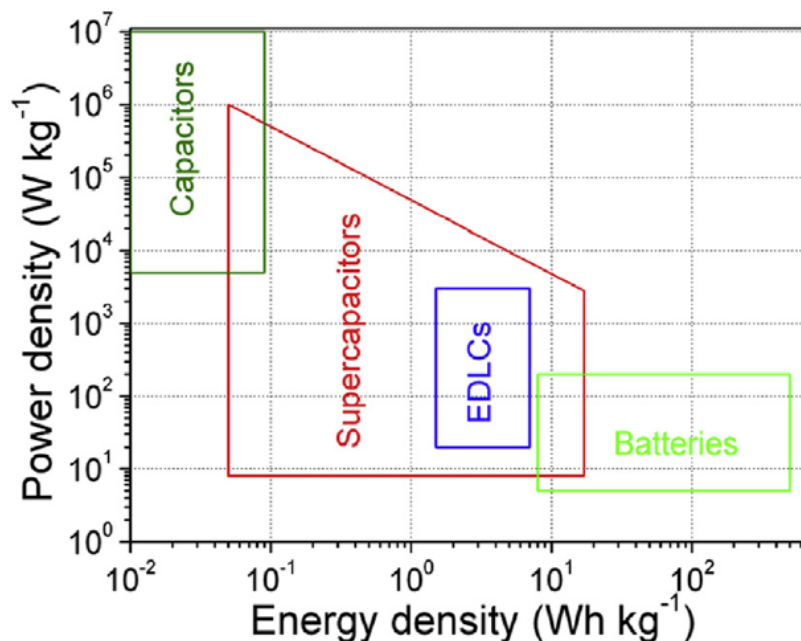


Figure 1-4 Ragone plots of conventional capacitors, supercapacitors and batteries [23] (Copyright 2014 Elsevier).

Table 1-1 Main characteristics of conventional capacitors, supercapacitors and battery.

Characteristics	Conventional capacitors	Supercapacitors	Battery
specific power (W/kg)	$\gg 10,000$	500-10,000	< 1000
specific energy (Wh/kg)	< 0.1	1-10	10-100
Working temperature ($^{\circ}\text{C}$)	-40-85	-40-70	0-40
charge time	negligible	s or min level	1-5 h
discharge time	negligible	s or min level	0.3-3 h
service life (cycles)	infinite	$> 10,000$	~ 1000

Thanks to series unique characteristics mentioned above, supercapacitors have been applied in many fields (Figure 1-5), such as energy storage type street light, power supply for wind turbine pitch, high power crane, cold start of heavy vehicle, energy recovery system, electrical vehicles for stop-go driving model, and so forth [34,35]. Back during Shanghai World Expo in 2010, 61 supercapacitor buses were already launched and the goal of “Zero Emission” in park was achieved successfully (data from Ministry of Science and Technology of China). In addition, according to the prediction by ID TechEx Ltd, the global market for supercapacitors will be as high as 6.5 billion dollars in 2024.

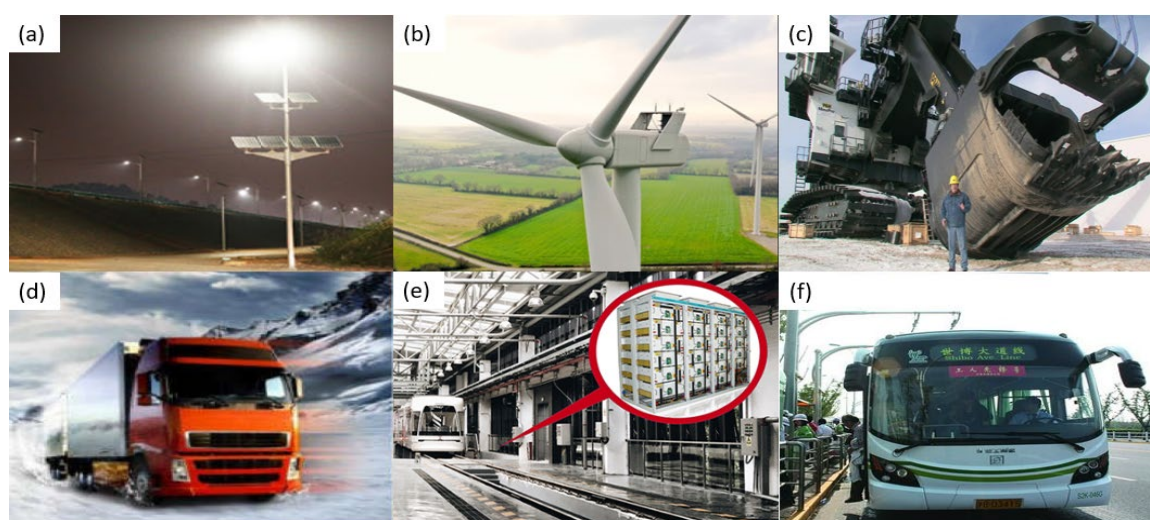


Figure 1-5 Representative applications of supercapacitors: (a) energy storage type street light, (b) power supply for wind turbine pitch, (c) high power crane, (d) cold start of heavy vehicle, (e) energy recovery system, and (f) electrical vehicles.

1.2 Energy storage mechanism

According to energy storage mechanism, supercapacitors can be classified in two types: electric double layer capacitors (EDLCs) and pseudocapacitors (PsCs).

1.2.1 EDLCs

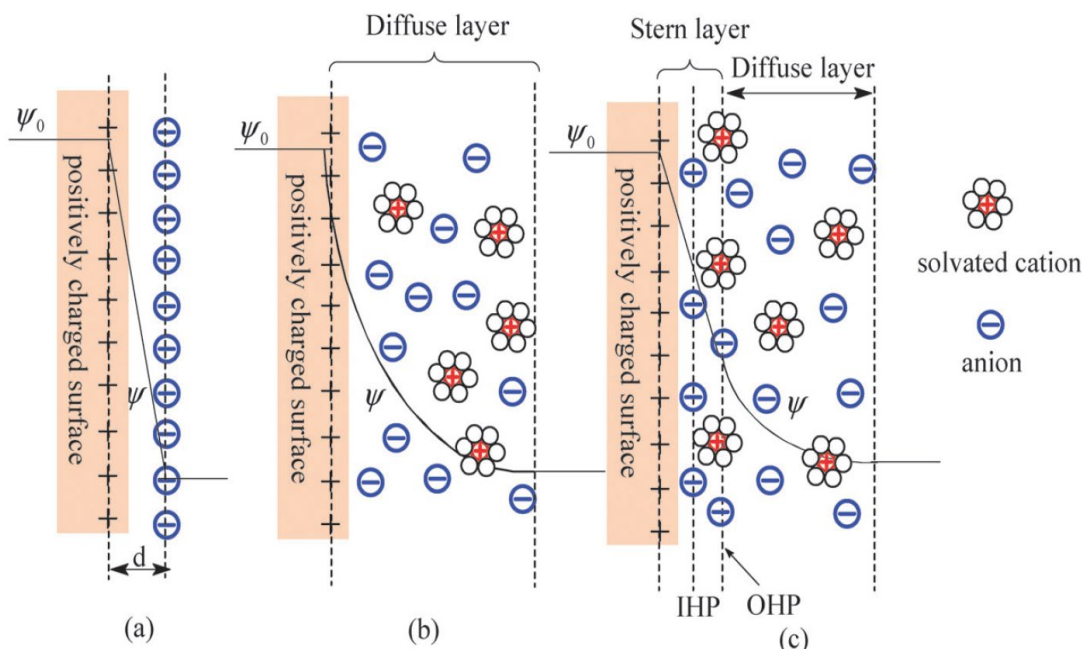


Figure 1-6 Models of EDL: (a) Helmholtz model, (b) Gouy-Chapman model, and (c) Stern model [39] (Copyright 2009 The Royal Society of Chemistry).

As early as 1879, Hermann Von Helmholtz first proposed EDL theory. In Helmholtz model, a layer of negative charges is formed on the charged conductor in electrolyte (as a compact layer) to counterbalance the positive charges under a finite distance (termed as d , surface of the conductor to center of the ions) [36-39], as illustrated in Figure 1-6a. Considering the influence of applied potential and electrolyte concentration, Louis Georges Gouy in 1910 and David Leonard Chapman in 1913 revised the simple Helmholtz model. The Gouy-Chapman model (Figure 1-6b) shows that the opposite ionic charges appear to neutralize the charged conductor, whereas the ions tend to distribute in electrolyte rather than adhere on the surface of conductor, displaying a diffuse layer with thickness [39-43]. In 1924, Stern model combining the aforementioned Helmholtz model and Gouy-Chapman model was put forward by Otto Stern and subsequently further modified by David C. Grahame. Briefly, the Stern model (Figure 1-6c) contains

Stern layer and diffuse layer, where Stern layer is divided into inner Helmholtz plane (IHP) and outer Helmholtz plane (OHP), corresponding to specifically or non-specifically adsorbed ions, and the region beyond OHP is diffuse layer [39, 44-46]. As of today, the Stern model is widely recognized as one approaching to the reality.

The EDL capacitance, which can be assumed to follow that of a parallel-plate capacitor model, is defined by Equation (1) [47]:

$$C = \frac{Q}{V} = \frac{\epsilon_r \epsilon_0 A}{d} \quad (1)$$

where C is the EDL capacitance; Q is the total charge; V is the applied voltage; ϵ_r is the dielectric constant of electrolyte; ϵ_0 is the permittivity of vacuum; d is the effective thickness of EDL (*i.e.* the Debye length); A is the effective area of electrode accessible to electrolyte ions. Based on Equation (1), the charging current is given by Equation (2) [47]:

$$I = \frac{dQ}{dt} = C \frac{dV}{dt} \quad (2)$$

where I is the charging current; Q is the total charge; t is the charging time; C is the EDL capacitance; V is the applied voltage. If the applied voltage varied with time is expressed by Equation (3) [47]:

$$V = V_0 + vt \quad (3)$$

where V is the applied voltage; V_0 is the initial voltage; v is the sweep rate; t is the time, the Equation (2) can be further described as Equation (4) [47]:

$$I = Cv \quad (4)$$

where I is the response current; C is the EDL capacitance; v is the sweep rate. Hence, rectangular curve in cyclic voltammetry (CV) test and triangular plot in galvanostatic charge/discharge (GCD) measurement are expected, as displayed in Figure 1-7a and Figure 1-7b, respectively. The principle and process of CV and GCD were illustrated in detail in Chapter 2.

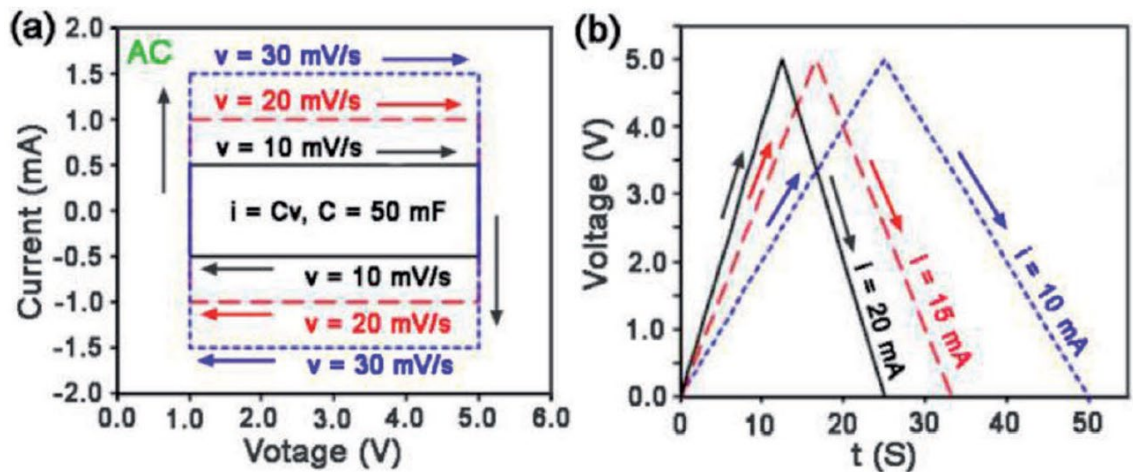


Figure 1-7 (a) Rectangular curves in CV test and (b) triangular plots in GCD measurement for EDL capacitance [47] (Copyright 2017 The Authors of Ref. 47).

Figure 1-8 shows the schematic diagram of EDLCs based on EDL theory. Two electrode are adhered on current collectors and immersed in given electrolyte solution containing a separator. The separator allows ionic permeation and more importantly can avoid possible short circuit. In charged process, anions and cations concentrate on positive and negative electrodes, respectively. In contrast, in discharge process, the motion of electrons from negative to positive electrodes is triggered via external circuit. In addition to that, the anions and cations in electrolyte mix again [48,49].

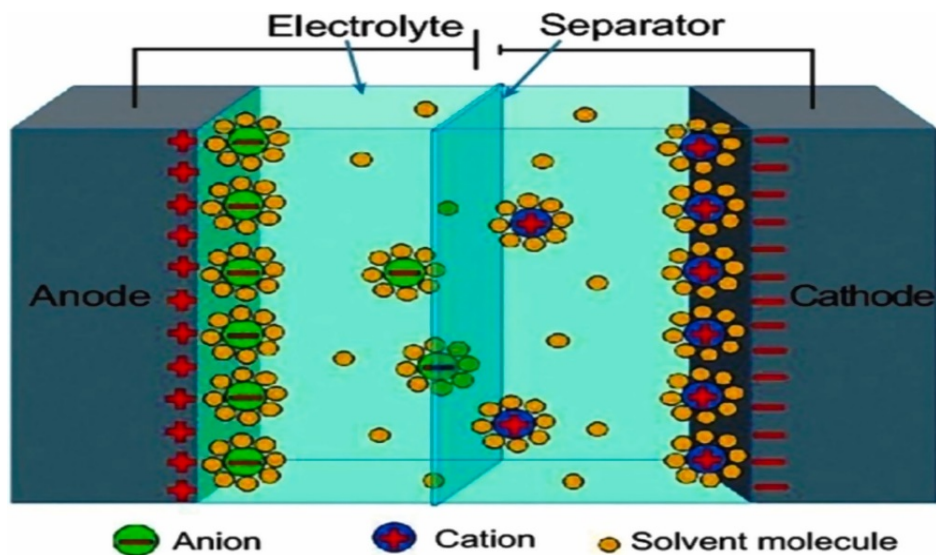


Figure 1-8 Schematic diagram of EDLCs [48] (Copyright 2018 Elsevier).

1.2.2 PsCs

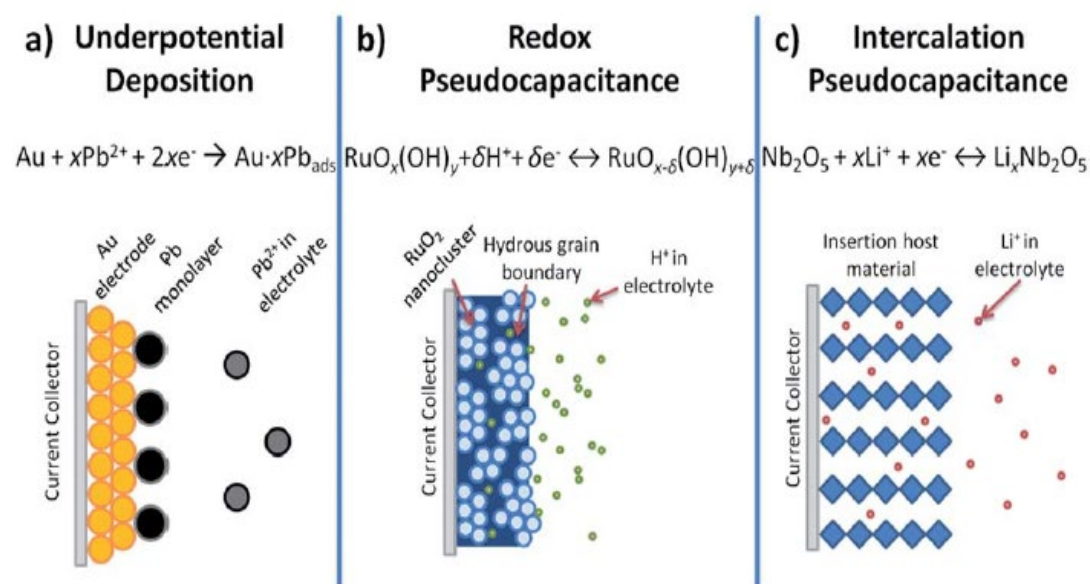


Figure 1-9 Types of pseudocapacitive mechanisms: (a) underpotential deposition, (b) redox, and (c) intercalation [51] (Copyright 2014 The Royal Society of Chemistry).

Figure 1-9 displays three pseudocapacitive mechanisms described by Brian Evans Conway in 1960s [50,51]. PsCs can produce a high SC, which is 10-100 times higher than that of EDLCs, to satisfy the ever-growing demand and gradually become the research hotspot [52-56]. Even though different types of processes and materials are involved, the electrochemical signatures of the three mechanisms still occur similarity and can be illustrated by Equation (5) [57]:

$$E = E^0 - \frac{RT}{nF} \ln\left(\frac{X}{1-X}\right) \quad (5)$$

where E is the electrode potential referred to a reference electrode; R is the ideal gas constant; T is the temperature; n is the number of electrons transferred for redox reactions occurring in the electrode; F is the Faraday constant; X is the fractional coverage of surface or inner structure of the active material. Based on Equation (5), the capacitance is defined by Equation (6) [57]:

$$C = \left(\frac{nF}{m}\right) \frac{X}{E} \quad (6)$$

where m is the molecular weight of active material. Because nonlinear relationship of E and X , the capacitance is not constant and thus is termed as pseudocapacitance [57]. In generally, conventional pseudocapacitive materials such as RuO_2 and MnO_2 (redox reactions occur at the surface) based electrodes display rectangular CV curve, linear GCD curve and fast kinetics, which are close to the characteristics of EDLCs [58-62]. Patrice Simon and Yury Georgievich Gogotsi in their influential literature entitled “Materials for electrochemical capacitor” [57] explained that this phenomenon was led by successive multiple surface redox reactions, as shown in Figure 1-10, and their theory is widely recognized so far. Based on it, some scientists think that the RuO_2 and MnO_2 cover the gap of EDLCs and battery [63,64].

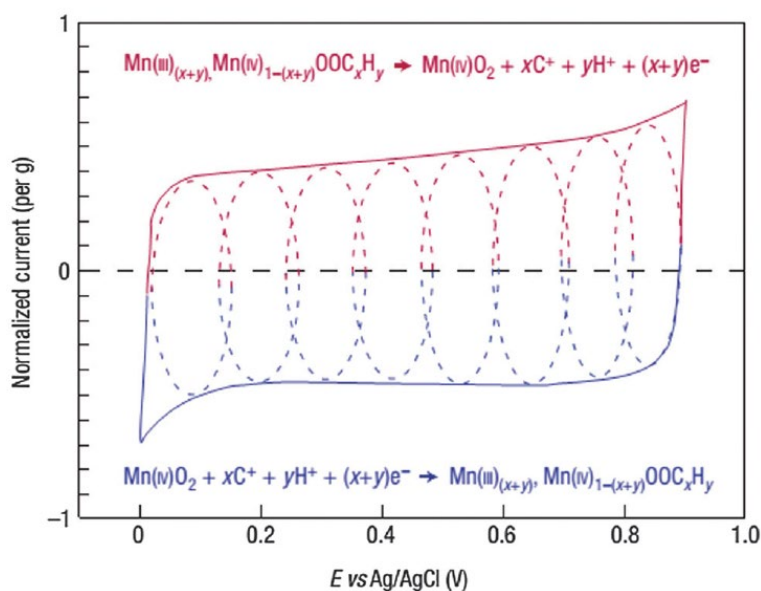


Figure 1-10 Schematic CV for a MnO_2 electrode [57] (Copyright 2008 Nature Publishing Group).

Recent researches further complete the traditional definition, in which the LiCoO_2 (battery material) and Ni(OH)_2 are most representative. As exhibited in Figure 1-11a, the plateaus in GCD measurement generally slop accompanied by the reduction of LiCoO_2 dimension and it is interesting to find that the plateau disappear at 6 nm LiCoO_2 , which means 6 nm LiCoO_2 deliver a typical pseudocapacitive behavior [65]. Similarly, in the case of layered Ni(OH)_2 , the obvious redox peaks in CV test were discovered (Figure 1-11b) but the kinetics was found to be quite rapid [66]. In summary, some materials exhibit obvious redox peaks in CV curve and non-linear line in GCD curve, different from

the features of RuO_2 and MnO_2 but similar to those of battery. On the other, better performances compared with battery in kinetics and reversibility are obtained (close to typical pseudocapacitive behaviors), which fails to be simply cataloged into traditional definition. In view of this, some scientists suggest that the mentioned phenomena bridge the gap of classical pseudocapacitive behaviors and battery behaviors [51,65-68]. Figure 1-12 shows the schematic diagram of PsCs. Of particular note is that EDLCs charge mechanism also exists in PsCs, but its contribution is negligible.

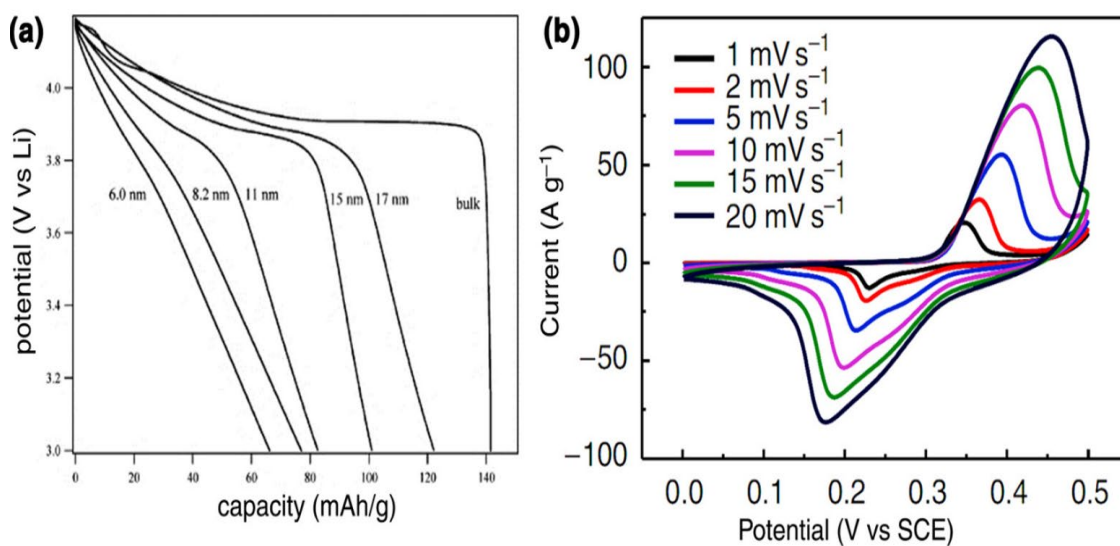


Figure 1-11 (a) Crystallite size effect of LiCoO_2 [65] (Copyright 2007 American Chemical Society) and (b) CV curves of Ni(OH)_2 [66] (Copyright 2013 Macmillan Publishers Limited).

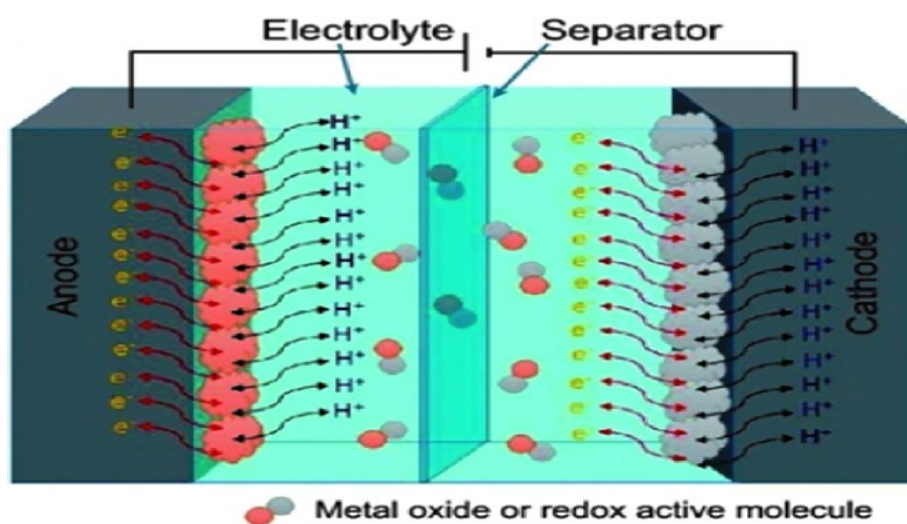


Figure 1-12 Schematic diagram of PsCs [48] (Copyright 2018 Elsevier).

1.3 Current state of the art for the electrode materials

The electrode materials play a main role in supercapacitors and their features such as morphology, structure, specific surface area, crystallinity and conductivity greatly influence the performances. EDLCs commonly utilize carbon based materials and PsCs employ transition metal oxides/hydroxides (TMO/Hs) as electrode materials.

1.3.1 Carbon based materials

In general, the conductivity, surface area and porosity of carbon based materials as the electrode materials of supercapacitors are critical to the performances [39,69]. Currently, activated carbons (ACs) are mostly widely used active materials for the supercapacitors electrodes and already commercialized in markets. A standard procedure to prepare ACs usually is divided into carbonization and activation [24,70,71]. The precursor like wood is converted to amorphous carbons and high surface area is reached via physical (under oxidizing atmosphere at 700-1200 °C) or chemical activation (through activating agents at 400-700 °C) [39,72]. For example, the wood carbon monolith (Figure 1-13a) synthesized by Liu *et al.* (poplar wood as precursor and HNO₃ solution as chemical) shows a specific capacitance (SC) of 234 F/g at 5 mA/cm² in 2 M KOH [73]. A general trend summarized from previous studies suggests that the pores narrower than 2 nm (*i.e.* micropores) deliver a significant impact on capacitance than the higher surface area with pores larger than 2 nm (*i.e.* mesopores or macropores). The pore size can be tailored by changing the parameters of activation such as temperature, concentration, time and frequency, which provides the reference for optimization.

The discovery of carbon nanotubes (CNTs) is a milestone in research of carbon materials. In relevant field of supercapacitors, thanks to their desirable porosity, CNTs are widely recognized as promising active electrode materials for supercapacitors and spark lots of attentions. Recently, many efforts were devoted to fabricate dense CNTs forest. For instance, compact fullerene-like carbon decorated CNTs (Figure 1-13b) were achieved on silicon taper nanorod scaffold, reported by micro energy team of USN. The as-fabricated electrode displays a high SC of 192 mF/cm² at 1 mV/s in 1 M H₂SO₄ [74].

Compared with ACs, the surface area of CNTs is relatively small. 2-3 times of initial surface area can be obtained via chemical activation [75,76]. According to report by Frackowiak *et al.*, the surface area of the sample is found to be as high as 1035 m²/g after KOH activation, while the value only reaches 430 m²/g before activation [77].

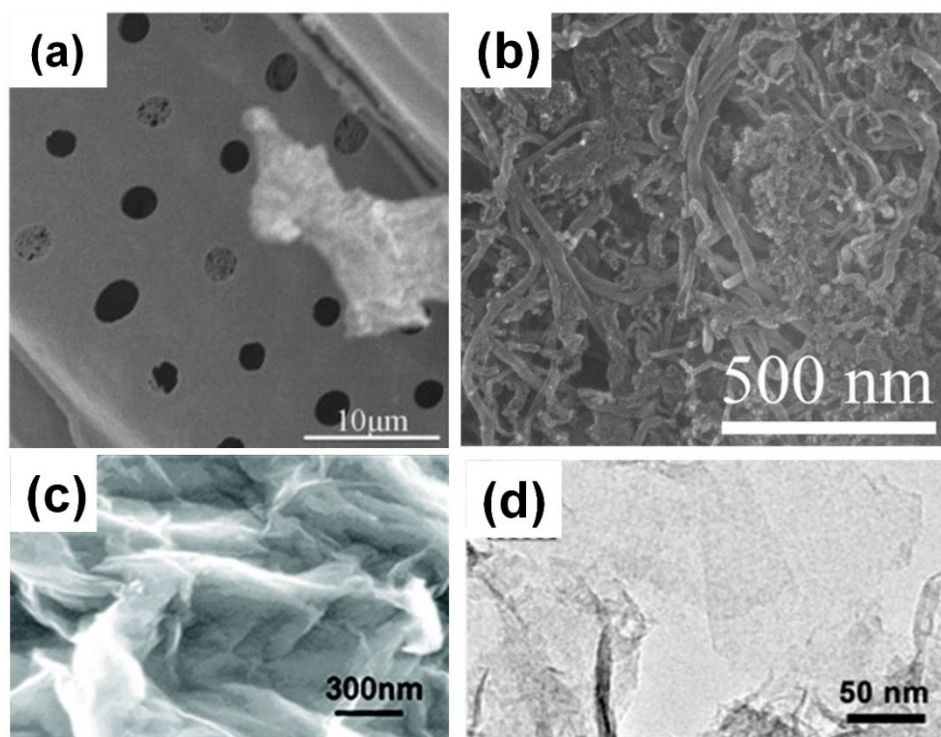


Figure 1-13 SEM images of the (a) wood carbon monolith [73] (Copyright 2011 Elsevier), (b) fullerene-like carbon decorated CNTs network [74] (Copyright 2017 Elsevier), (c) graphene material [83] (Copyright 2009 American Chemical Society), and TEM image of the (d) RGO sample [84] (Copyright 2010 Elsevier).

In comparison with ACs and CNTs, graphene possesses the largest specific surface area (a mono-layer is 2620 m²/g) [78-80]. According to reports, the theoretical SC of graphene is about 550 F/g if the entire surface area is completely utilized [81]. However, in real fabricated supercapacitors, the achieved SCs are far lower than the theoretical value, which is mainly attributed to re-stacking of graphene. For instance, Vivekchand *et al.* synthesized graphenes by three different approaches. The maximum SC value only reaches up to 117 F/g [82]. The graphene (Figure 1-13c) prepared by Wang *et al.* displays a SC of 205 F/g [83]. Besides, the tedious preparation pathway also severely limits its mass production. Reduced graphene oxide (RGO) with low agglomeration seems to be

a good solution. For example, the RGO (Figure 1-13d) prepared by Chen *et al.* exhibits a SC of 348 F/g at 0.2 A/g in 1 M H₂SO₄ [84].

1.3.2 TMO/Hs

Among various pseudocapacitive materials, RuO₂ is the most explored one. The earliest study of RuO₂ in PsCs can be traced back to 1975 [63,64]. So to speak, the electrochemical properties of RuO₂ inspired the theory of PsCs. RuO₂ has a high theoretical SC of around 1000 F/g. What is more, it possesses an overwhelming potential window of 1.2 V, in which three oxidation states (Ru²⁺, Ru³⁺, Ru⁴⁺) are accessible [24]. The value of structural water was verified in subsequent researches. The theoretical SC of RuO₂·0.5H₂O reaches to 1360 F/g [51,65,85,86]. Besides, a high SC of 1340 F/g at 25 mV/s was obtained by hydrous RuO₂ (Figure 1-14a) synthesized by Hu *et al.* [87]. Moreover, hydrogen-inserted hydrous RuO₂ (denoted as H_xRuO₂·xH₂O) and ruthenic acid (denoted as H_xRuO_{2+y}·zH₂O) were investigated and further expanded utilization of Ru [64]. Despite the virtues of RuO₂ and achieved remarkable progress, for the moment its applications only focus on some specific areas such as aerospace and military since its inferior position in cost and environment friendliness [24,51]. Therefore, it is necessary to seek cost-effective materials without environment harmfulness as alternatives.

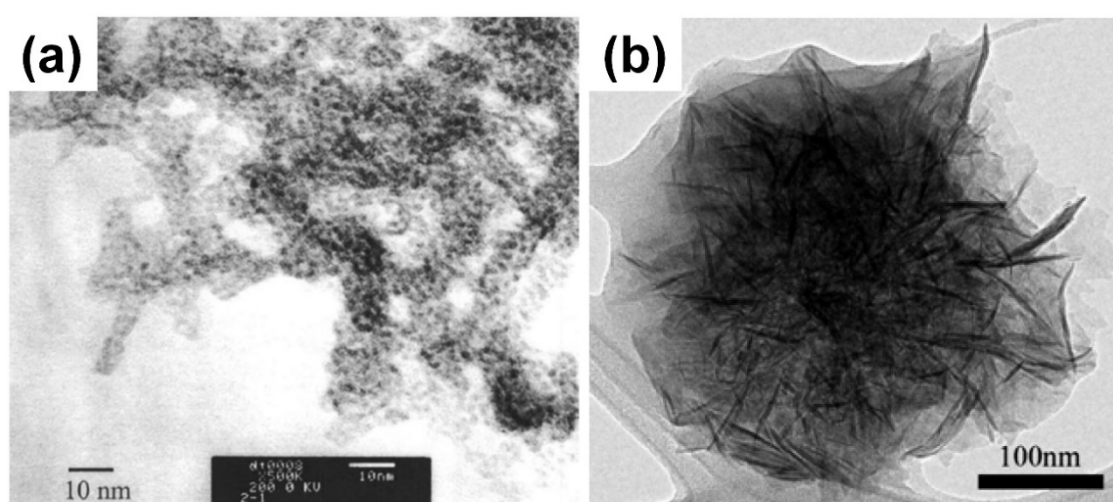
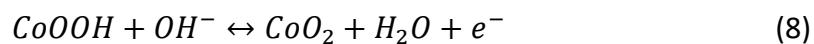
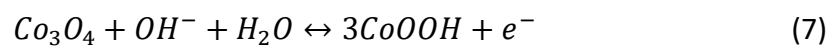


Figure 1-14 HRTEM image of the (a) hydrous RuO₂ nanodots [87] (Copyright 2004 The Electrochemical Society) and TEM image of the (b) highly porous structured MnO₂ [89] (Copyright 2011 American Chemical Society).

MnO₂ is widely considered as a promising alternative of RuO₂ due to its low cost, non-toxic and abundant resources. As early as 1999, Lee *et al.* already investigated its pseudocapacitive properties [88]. The charge storage generates within thin layer of the MnO₂ surface. This gives rise to the capacitance lower than its theoretical value (1100-1300 F/g) [24], particularly occurring in thick electrodes. By hard working for many years, to date, the achieved pseudocapacitive SC of MnO₂ based electrode is over 1000 F/g. For example, an ultrahigh SC of 1230 F/g based on the mass of MnO₂ (Figure 1-14b) was produced by a sponge supercapacitor, reported by Chen *et al* [89]. The various strategies developed for MnO₂ electrodes jointly demonstrate that the nanostructuring is a highly effective approach for accessing all storage sites of MnO₂. Nevertheless, the relatively low theoretical SC still excludes MnO₂ from wide applications [33,35].

In recent years, tremendous efforts have been devoted to inexpensive and environmentally-friendly materials, such as Co₃O₄, Ni(OH)₂ and Co(OH)₂, thanks to their superior theoretical SCs. For example, Wang *et al.* reported Co₃O₄ nanowires (Figure 1-15a) with the SC of 977 F/g at 2 A/g [90]. The Co₃O₄ nanorods (Figure 1-15b) synthesized by Guo *et al.* exhibit a SC of 739 F/g at 5 mV/s [91]. Intuitively, the produced SCs are far lower than theoretical value of 3560 F/g [92]. The redox reactions are illustrated by Equation (7) and (8) [93,94].



Besides, except for low SCs, the rate performances of as-fabricated Co₃O₄ electrodes are extremely poor. Like above mentioned Co₃O₄ nanowires, compared with the initial SC at 2 A/g, only 49.5% of SC was maintained at 10 A/g, while for Co₃O₄ nanorods, from 5 to 100 mV/s, the loss of SC reached up to 47.5%. Constructing hollow Co₃O₄ is widely recognized as a good approach, since hollow structure is able to serve as a “reservoir”, giving rise to efficient ions diffusion at high scan rate and current density [95,96]. For instance, the 3D-nanonet hollow structured Co₃O₄ (Figure 1-15c) reported by Wang *et al.* delivers a rate capability of 72% at 15 A/g (739 F/g at 1 A/g) [96]. The hollow Co₃O₄

nanowires (Figure 1-15d) prepared by Xia *et al.* show a SC of 599 F/g at 2 A/g and 73% of the SC is retained at 40 A/g [97]. Even so, there is plenty of room for further performance improvement of Co_3O_4 .

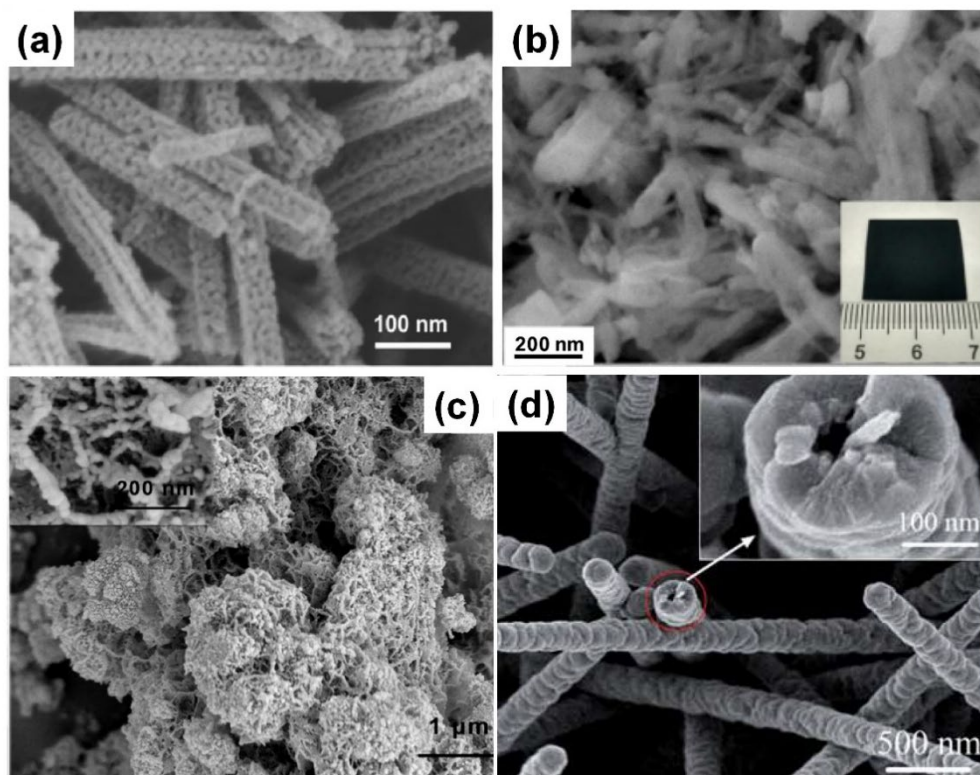
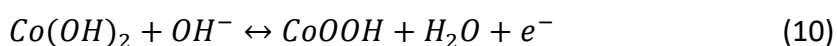
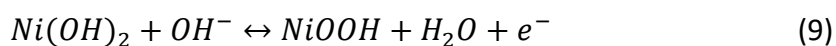


Figure 1-15 SEM images of the (a) Co_3O_4 nanowires [90] (Copyright 2014 WILEY-VCH Verlag GmbH & Co. KGaA), (b) Co_3O_4 nanorods [91] (Copyright 2017 Elsevier), (c) 3D-nanonet hollow structured Co_3O_4 [96] (Copyright 2014 American Chemical Society), and (d) hollow Co_3O_4 nanowires [97] (Copyright 2011 The Royal Society of Chemistry).

$\text{Ni}(\text{OH})_2$ and $\text{Co}(\text{OH})_2$ also possess ultrahigh theoretical SCs [98] and have triggered many efforts. The satisfied SCs were reached in previous contributions. For example, $\text{Ni}(\text{OH})_2$ nanospheres (Figure 1-16a) synthesized by Li *et al.* [66] and $\text{Ni}(\text{OH})_2$ nanosheets (Figure 1-16b) prepared by Xiong *et al.* [99] exhibit SCs of 2188 F/g (1 mV/s) and 2384.3 F/g (1 A/g), respectively; $\text{Co}(\text{OH})_2$ films fabricated by Zhou *et al.* display a SC of 2646 F/g at 8 A/g [100]. The redox reactions are expressed by Equations (9), (10) and (11) [101,102].



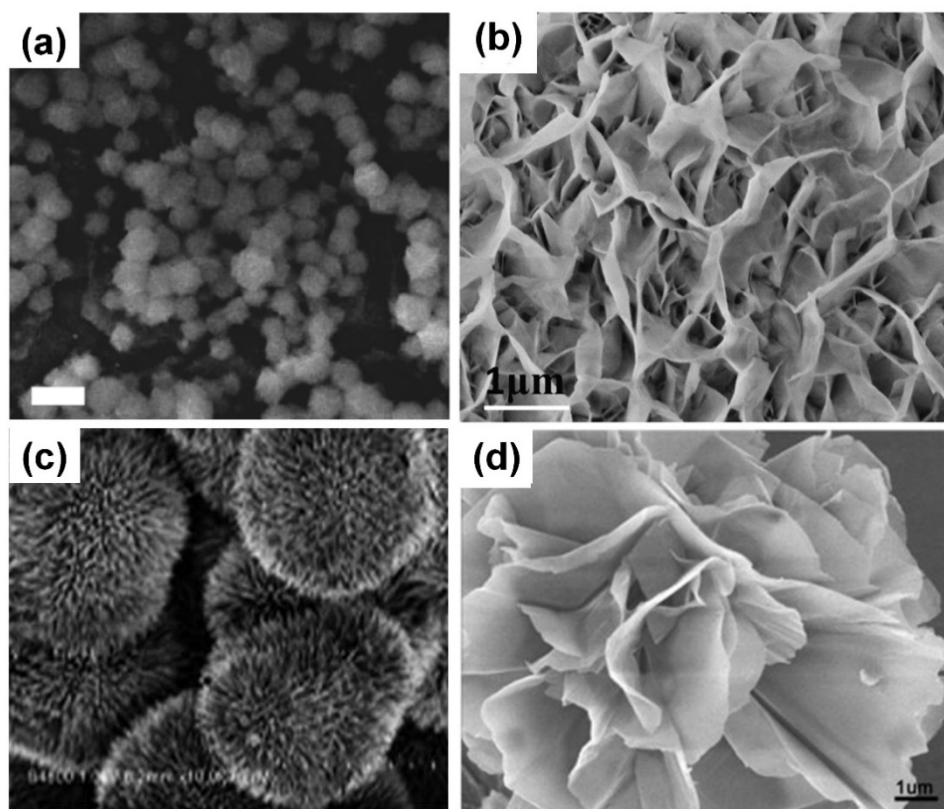
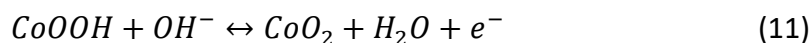


Figure 1-16 SEM images of the (a) Ni(OH)₂ nanospheres [66] (Copyright 2013 Macmillan Publishers Limited), (b) Ni(OH)₂ nanosheets [99] (Copyright 2014 Elsevier), (c) Ni-Co binary hydroxide microspheres [113] (Copyright 2012 The Royal Society of Chemistry), and (d) flower-like Ni-Co binary hydroxide [102] (Copyright 2015 Elsevier).

The remarkable SCs so far were produced, however, low mass loading is a problem. For example, the mass loading for above mentioned Ni(OH)₂ nanospheres and Ni(OH)₂ nanosheets are only 0.1 μg and 0.01 mg, which severely hinders their commercial use. Recently, Ni-Co binary hydroxide was investigated, which was found with unique characteristics such as stronger layer orientation, increased redox active sites, and reduced resistivity [103-107], and consequently widely considered as a promising route for achieving high SCs at high loading mass. Unfortunately, because of undesirable morphology [108,109] and involved binder for loading onto the electrode [110,111], to date the performance of supercapacitors made of Ni-Co binary hydroxide needs further improvement. For example, the Ni-Co binary hydroxide nanosheets reported by Chen *et al.* [112] and microspheres (Figure 1-16c) synthesized by Tao *et al.* [113] present SCs of 2682 F/g and 2275.5 F/g at 3 A/g and 1 A/g, respectively. But the decrease of SCs at high

current is drastic (1706 F/g at 20 A/g and 1007.8 F/g at 25 A/g correspond to nanosheets and microspheres). For the flower-like Ni-Co binary hydroxide (Figure 1-16d) developed by Zhang *et al.*, the capacitance loss is more than 25% after 3000 cycles [102]. In addition, in certain cases, the loading mass is still unsatisfied and complex routes also preclude them from practical applications. To sum up, at present, to utilize the advantages of the novel Ni-Co binary hydroxide for making high performance supercapacitors, there must be massive research efforts to optimize its fabrication process for desirable morphology, as well as binder free electrode.

1.4 Research focus

Nowadays, further improving the performance of supercapacitors as energy storage devices of high energy density with no compromising their high power density is urgent to satisfy the ever-growing demand. Based on overview of recent progress as summarized above, it was found that the electrode materials are crucial for high-energy density supercapacitors, among which PsCs materials with large number of the redox centers have been proven promising for achieving high-energy density supercapacitors. Hence, in this thesis we will investigate and synthesize PsCs materials for approaching high-performance supercapacitors. Among various TMO/Hs utilized in PsCs, Co_3O_4 and Ni-Co binary hydroxide stand out owing to their unparalleled advantages. Our work thus focuses on optimizing Co_3O_4 and Ni-Co binary hydroxide. Additionally, we also strive for potential alternative electrode material.

The morphology and structure features, which directly determine the available surface area, active sites, ions diffusion/permeation and electrons transportation, play an important role in PsCs performance of active material. As the first strategy to improve the performance of Co_3O_4 and Ni-Co binary hydroxide, our effort will focus on synthesizing materials with desirable morphologies. Material with porous and nanosheet configurations in general will provide large surface areas and therefore provide efficient redox reactions. Fabrication of Co_3O_4 with porous hollow spheres/nanoboxes has been explored, as well as fabrication of Ni-Co binary hydroxide with nanosheets encapsulated with nanowires has been investigated.

The high electrical conductivity and effective surface area supporting the redox reaction will enhance the functionality of PsCs material for high-energy density supercapacitors. As the second strategy, we develop the technology for loading PsCs material in a way to realize the binder-free electrode which will reduce the electron transfer impedance and avoid the block of surface for redox reaction. We have proposed a one-step synthesis, by which Ni-Co binary hydroxide was grown on the active electrode directly.

To be specific, as mentioned earlier, fabricating hollow structure is an effective approach to overcome the drawbacks in previous applications of Co_3O_4 . Hence, metal-organic frameworks (MOFs), in which zeolitic imidazolate framework (ZIF)-67 as self-sacrificial template is most representative, was introduced. In general, fabrication of MOFs is divided into three steps: synthesis of dodecahedral diamond ZIF-67, conversion to hollow Co-layered double hydroxide (LDH), and preparation of hollow Co_3O_4 . However, if the approach are to move forward towards application, there are three significant issues must be addressed. As the first, it is important to control Co_3O_4 crystallinities for high-rate capability and SC performance. . In this thesis, by controlling the concentration of $\text{C}_4\text{H}_6\text{N}_2$ we will are able to prepare different types of crystalline Co_3O_4 . As a consequence, outstanding rate performance (a 93.6% capacitance retention from 1 A/g to 20 A/g) and excellent SC (1832.7 F/g at 1 A/g) were achieved, respectively. As the second, it is difficult to systematically design the size of ZIF-67 at present, which fails to further enhance the electrochemical performance. Aiming at solving this problem, the formation mechanism of ZIF-67 was studied. A theory, which stepwise formation process of ZIF-67 is divided into nucleation phase and growth stage, was proposed and verified by the phenomenon that the average size of ZIF-67 increases with the decrease of $\text{C}_4\text{H}_6\text{N}_2/\text{Co}(\text{NO}_3)_2$ ratio in initial precipitation reaction. The third critical issue is to maintain the morphology during the conversion of precursor to Co_3O_4 . It was found that the temperature plays an important role. Accordingly, different temperatures were set in heat treatment so that the final achieved Co_3O_4 was able to effectively inherit the morphology (negligible size contraction and few broken pieces). Briefly, this sectional work was inspired by the first strategy. Namely, improve the supercapacitors performance of Co_3O_4 by synthesizing desirable morphology.

Despite the progress made in Co_3O_4 study, achieving higher SC to satisfy the increasing demands is still a pursuant goal. The aforementioned synergistic contributions in Ni-Co binary hydroxide have the potential to reach this and thus sparked our interest. It is well-known that the morphological evolution at various Ni/Co ratio, which is ascribed to the competition of Ni and Co cations for hydroxide radicals, is inevitable. Considering that the most electroactive sites generated by valence interchange or charge hopping between cations generally is obtained at intermediate Ni/Co ratio, the morphology providing a largest surface area should be obtained at the specific ratio. Meanwhile, facing towards practical application, the topics of binder-free, high loading mass and facile fabricated method are clearly three of considerable importance. Hence, there are several challenges needed to be taken up. In traditional ways, besides Ni^{2+} and Co^{2+} , only single OH^- source was involved in synthesis of Ni-Co binary hydroxide. In this work, a novel one-step method was proposed, in which NH_4F was introduced to tailor the morphology. We are able to achieve a desirable morphology at the specific Ni/Co ratio, demonstrating an ultrahigh SC. The work and results have formed a major part of chapter 3. As the effort for investigation of potential alternative electrode material, the supercapacitors behaviours of ZnWO_4 were also explored, the research results are published in a conference, and presented in detail in 3.5 in the thesis.

2 Experimental details

2.1 Chemicals

The main chemicals in this work were listed in Table 2-1.

Table 2-1 Main chemicals in this work.

Name	Chemical formula	Manufacturer
ethanol	C_2H_5OH	VWR Chemicals
methanol	CH_3OH	MERCK
hydrochloric acid	HCl	VWR Chemicals
cobalt nitrate hexahydrate	$Co(NO_3)_2 \cdot 6H_2O$	Sigma Aldrich
2-methylimidazole	$C_4H_6N_2$	Sigma Aldrich
nickel nitrate hexahydrate	$Ni(NO_3)_2 \cdot 6H_2O$	Sigma Aldrich
urea	$CO(NH_2)_2$	Sigma Aldrich
ammonium fluoride	NH_4F	MERCK
zinc nitrate hexahydrate	$Zn(NO_3)_2 \cdot 6H_2O$	Sigma Aldrich
sodium tungstate dihydrate	$Na_2WO_4 \cdot 2H_2O$	Sigma Aldrich
acetylene black	C	Alfa Aesar
PVDF	$-(C_2H_2F_2)_n-$	Sigma Aldrich
NMP	C_5H_9NO	Sigma Aldrich
potassium hydroxide	KOH	MERCK
potassium chloride	KCl	Sigma Aldrich
NF	Ni	Vale

2.2 Instruments and equipments

The main experimental instruments and equipments in this work were listed in Table 2-2.

Table 2-2 Main experimental instruments and equipments in this work.

Name	Model	Company
electronic balance	SI-234	Denver Instrument
electronic balance	AE200	Mettler
ultrasonic bath	FB15051	Fisher Scientific
magnetic stirrer with heater	M21/1	Framo Gerätetechnik
centrifuge	MiniSpin plus	Eppendorf AG
Teflon-lined stainless-steel autoclave	HR	HuoTong Experimental Instrument
furnace	LHT 02/17	Nabertherm
tube furnace	MSL	MTI Corporation
SEM	SU3500	Hitachi
SEM	SU8230	Hitachi
EDX system	-	EDAX Ametek
X-ray diffractometer	EQUINOX 1000	Thermo Fisher
X-ray diffractometer	DRIGC-Y 2000A	Aolong Radiative Instrument
X-ray photoelectron spectrometer	ESCALAB 250Xi	Thermo Fisher
electrochemical workstation	IM6	Zahner

2.3 Material characterizations

The surface morphological characterization was conducted on scanning electron microscope (SEM), in which a narrow beam of electrons scans the surface of sample and the emitted secondary electrons produce the image [33,35]. Energy-dispersive X-ray (EDX) system (usually equipped on SEM) was used to characterize the elemental composition. Based on the intensity and distribution measurement of the sample's

emitted X-rays, excited by interaction of incident X-rays and sample, the specific element can be determined [33,35]. The principle of XRD is that when a monochromatic beam of X-rays incidents to the sample, via analysis of intensity and location of X-ray diffraction (obeying the Bragg's law) peaks in XRD patterns, the crystal structure can be confirmed. In this thesis, Cu-K α radiation ($\lambda = 1.5406 \text{ \AA}$) was employed in XRD. Further, the crystallite size was calculated according to Scherrer equation [114,115]. X-ray photoelectron spectroscopy (XPS) was performed to reveal the chemical status. The typical XPS spectrum is plotted by the binding energy of detected photoelectrons (excited by X-rays) as the horizontal and the intensity of detected photoelectrons as the ordinate [64]. In this work, monochromatic Al K α excitation was used in XPS.

2.4 Electrochemical measurements

Because of high porosity, surface area and conductivity, nickel foam (NF) was used as the current collector. In electrode fabrication process, the synthesized material (Co₃O₄, ZnWO₄ in this study), acetylene black (conductive agent), and polyvinylidene fluoride (PVDF, binder) were thoroughly ground in n-methyl-2-pyrrolidone (NMP) solution (dispersing agent), and the obtained slurry was pressed on NF. The systematical electrochemical assessments were characterized on an electrochemical workstation under three-electrode configuration at room temperature, in which the as-fabricated electrode, Pt net/wire, and Ag/AgCl (3.5 M KCl) were served as working electrode (WE), counter electrode (CE) and reference electrode (RE), respectively, and 2 M KOH solution was employed as electrolyte. The schematic illustration of three-electrode configuration was displayed in Figure 2-1. Of special interest is the synthesized Ni-Co binary hydroxide grown on NF could be utilized as WE without electrode fabrication process.

CV is extensively used technique for electrochemical analysis. In CV assessment, the given potential is conducted amid the WE and RE, where the potential of WE sweeps to set value and backs to initial value (linear response vs. time, reflected by scan rate), and the current is measured amid the WE and CE [64,116,117]. The current vs. the potential of WE is plotted as CV curve. Based on CV curves at various scan rate, capacitive nature

of the electroactive material can be determined and the SC is given by Equation (12) [118]:

$$C = \frac{\int i(V)dV}{2mv\Delta V} \quad (12)$$

where C (F/g) is the specific capacitance; $\int i(V) dV$ (V·A) is the integrated area of the CV curve; m (g) is the mass of the active material; v (V/s) is the scan rate; ΔV (V) is the potential window.

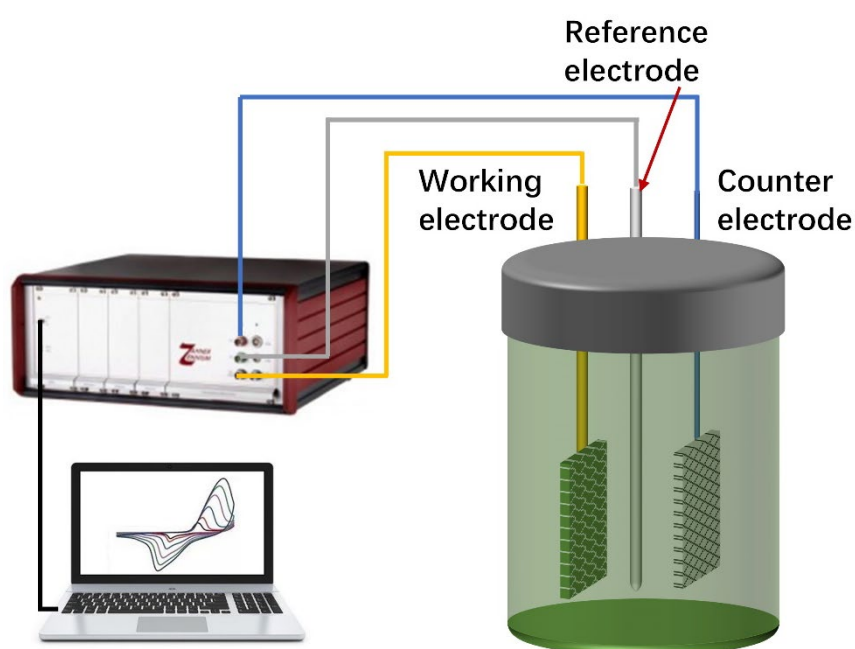


Figure 2-1 Schematic illustration of three-electrode configuration.

Compared with CV measurement, the SC calculated from GCD test is closer to real performance. In GCD assessment, a constant charge current is applied on WE until the potential reaches to a set value, then a constant discharge current (equal magnitude of charge current) is conducted on WE until the potential backs to original value [64,116,117]. The potential of WE vs. time is plotted as GCD curve. The SC is defined by Equation (13) [118]:

$$C = \frac{It}{m\Delta V} \quad (13)$$

where C (F/g) is the specific capacitance; I (A) is the discharging current; m (g) is the mass of the active material; ΔV (V) is the potential window.

The electrochemical impedance spectroscopy (EIS) measurement was conducted in this study at open circuit potential with a perturbation of 5 mV. In generally, the obtained Nyquist plot comprises a semicircle (high frequency range) and a straight line (low frequency region). Specifically, the diameter of the semicircle corresponds to charge transfer resistance (R_{ct}) and the slop of line reflects the ion diffusion [52,119,120]. Moreover, the intrinsic resistances which are determined by the ion conductivity in electrolyte and the electron conductivity of active material, and the contact resistances generated at the both interfaces of the electrolyte/active material and the active material/current collector, are summarized as R_s . The value of R_s is given by the intersection of Nyquist plot and real axis [96,121,122].

The durability performance of the electrode, which is reflected by the capacitance retention after long term cycles, is crucial in practical application. Repetitive GCD tests were conducted on the fabricated electrode in this study. The coulombic efficiency is calculated by Equation (14) [96]:

$$\eta = \frac{t_d}{t_c} \quad (14)$$

where η (%) is the coulombic efficiency; t_d (s) is the discharging time; t_c (s) is the charging time.

3 Summary of main research results

3.1 Overview

As mentioned above, Co_3O_4 and Ni-Co binary hydroxide have been proven promising electrode materials. Previous contributions still remain a short barrel to fulfil the requirements of high performance supercapacitors in terms of SC, rate and cycling. Synthesizing desirable morphology and structure of the aforementioned materials and developing binder-free electrode were proposed as two strategies to improve the performances of Co_3O_4 and Ni-Co binary hydroxide as active materials for supercapacitors electrodes.

Based on the first strategy, the following works were done: (1) hollow Co_3O_4 spheres with porous and thin-wall nature were synthesized from ZIF-67 precursors; (2) the formation mechanism of ZIF-67 was further investigated. Via initial precipitation reaction, the sizes of precursors could be well controlled; (3) unique morphology of nanosheets encapsulated with nanowires was obtained in synthesis of Ni-Co binary hydroxide. Benefited from desirable morphologies and structures, which provided large specific surface areas, increased redox active sites, facile ions diffusion and electrons transportation, the improved supercapacitors performances were achieved successfully.

According to the second strategy, a one-step method was developed in preparation of Ni-Co binary hydroxide. The active material in the unique morphology was grown on the current collector directly without in virtues of binder, which led to a good electric contact.

Besides, the supercapacitors behaviors of ZnWO_4 , a potential alternative electrode material, were also explored. In this Chapter, the experiments, characterizations, measurements and discussions were briefly illustrated below and the full-length papers were enclosed at the end of the thesis.

3.2 Porous thin-wall Co_3O_4 spheres for supercapacitors

3.2.1 Sample preparation

A facile method consisting of precipitation, solvothermal and annealing reactions was employed, as described below:

- (1) 0.437 g $\text{Co}(\text{NO}_3)_2 \cdot 6\text{H}_2\text{O}$ was dissolved in 20 mL methanol. 0.616 g $\text{C}_4\text{H}_6\text{N}_2$ was dissolved in 20 mL methanol;
- (2) The $\text{C}_4\text{H}_6\text{N}_2$ methanol solution was added to $\text{Co}(\text{NO}_3)_2$ methanol solution dropwise. The precipitates were obtained after ultrasonic bath of the mixed solution for 20 min;
- (3) 0.175 g $\text{Co}(\text{NO}_3)_3 \cdot 6\text{H}_2\text{O}$ was added to precipitate (0.02 g) methanol (15 mL) solution. The mixture was transferred to a Teflon-lined stainless-steel autoclave and heated at 120 °C for 1 h;
- (4) The final samples were obtained through annealing reaction at 400 °C for 2 h.

3.2.2 Material characterizations

The XRD patterns of the sample were shown in Figure 3-1a. The highlighted sharp peak located at 36.9°, and the rest seven diffraction peaks located at 19°, 31.3°, 38.6°, 44.9°, 55.8°, 59.5°, and 65.4°, are consistent with the Co_3O_4 [123]. In EDX spectrum seen in Figure 3-1b, the peaks correspond to Co and O. No other elements are pointed out, verifying the high purity of the sample. The high resolution XPS spectra of Co 2p and O 1s were depicted in Figure 3-1c and Figure 3-1d, respectively. For Co 2p, the peaks at binding energies of 779.4 and 794.4 eV stand for Co^{3+} and the peaks at 780.4 and 795.7 eV identify Co^{2+} [120]. For O 1s, three peaks at 529.9, 530.9 and 532 eV can be ascribed to oxygen, hydroxyl groups and absorbed water, respectively [96,124]. The SEM images under high magnification of the precursors and the Co_3O_4 were exhibited in Figure 3-1e and Figure 3-1f, respectively. The heat treatment at high temperature conducted on the precursors barely damage the architecture and the Co_3O_4 shows uniform spherical structure (diameter of 500 to 600 nm) with highly porous characteristic. Moreover, from

a broken piece, the hollow nature and thin-wall feature of the Co_3O_4 spheres can be confirmed.

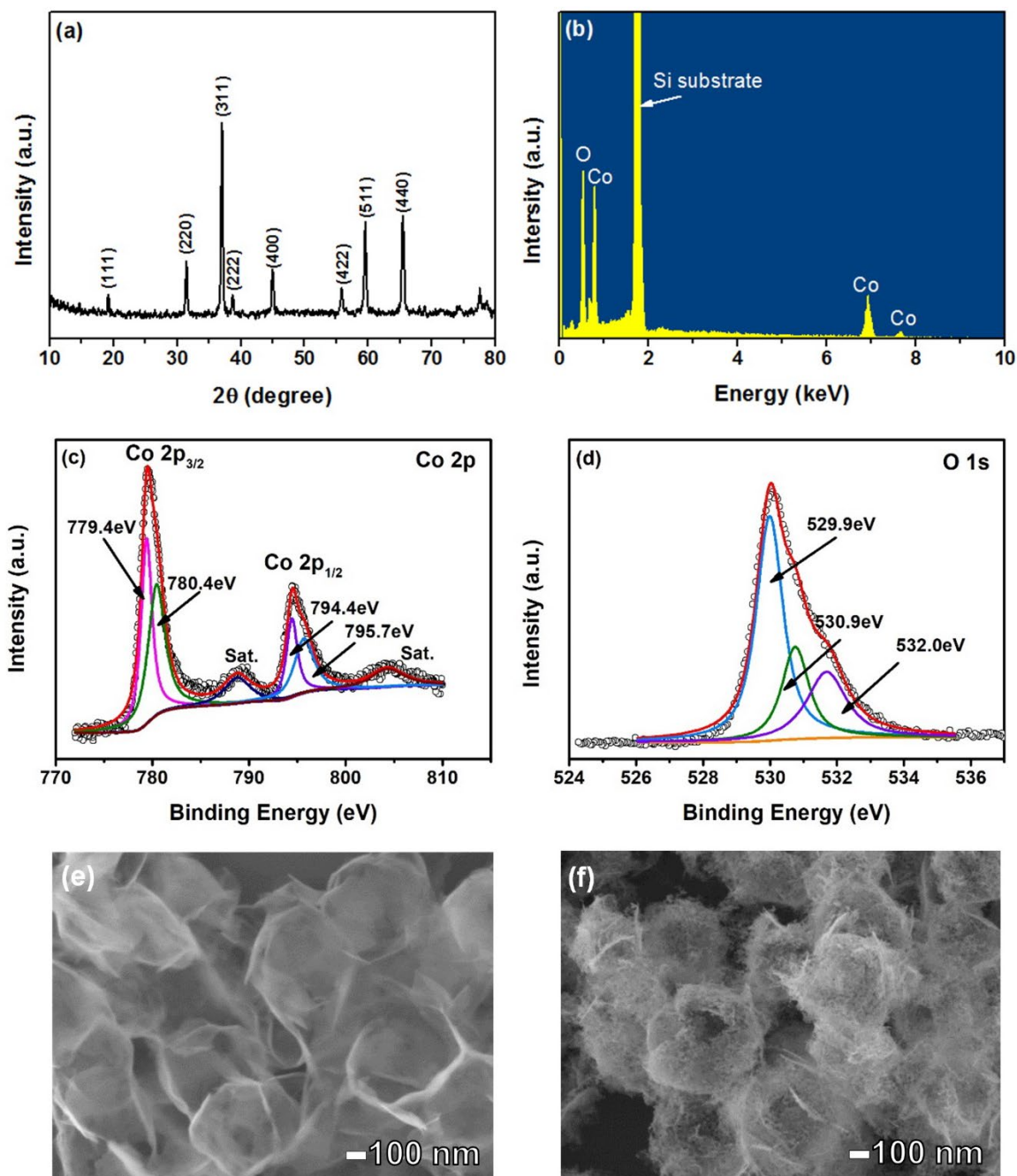


Figure 3-1 (a) XRD patterns and (b) EDX spectrum of Co_3O_4 , XPS spectra of Co_3O_4 : (c) Co 2p and (d) O 1s, SEM images of (e) precursors and (f) Co_3O_4 .

3.2.3 Supercapacitors behaviors

The CV curves of as-prepared Co_3O_4 electrode were achieved at scan rates from 5 to 100 mV/s, as plotted in Figure 3-2a. The potential window was set as 0 to 0.55 V. All highly symmetrical curves exhibit two pairs of redox peaks, completely differing from rectangular shape, which corresponds to two faradic redox processes illustrated by Equation (7) and (8). The increase of scan rates arises the shift of peak position, anodic peak to higher potential while cathodic peak to lower potential, further indicating the pseudocapacitive characteristics of the synthesized Co_3O_4 [94,125]. It is noteworthy that the change of scan rate remarkably affects the current response and fails to cause obvious distortion of CV curves. The desirable phenomena reveal rapid response and excellent reversible process, and imply a good rate capability [126]. The SCs based on CV curves were presented in Figure 3-2b. Intuitively, the boost of scan rates gives rise to attenuation of capacitance values, since limited diffusion of OH^- ions at high scan rate or current density lead to relatively insufficient active material in redox reaction [127]. The high SC of 948.9 F/g is produced at scan rate of 5 mV/s and only decays to 900.6 F/g at 100 mV/s.

Figure 3-2c shows the discharge curves tested at current densities from 1 to 20 A/g. Unlike straight line for EDLCs, two plateaus, which were generated by redox reactions expressed by aforementioned Equation (7) and (8), exist in all curves. Particularly, even at high current density of 20 A/g, the plateaus still can be observed, also suggesting the good rate performance. With the increase of current densities from 1 A/g to 20 A/g, the initial SC of 988 F/g fades to 925 F/g, representing a 93.6% capacitance retention, as displayed in Figure 3-2d. The EIS study was performed in frequency range of 100 mHz to 100 kHz (Figure 3-2e). The Co_3O_4 electrode delivers a low R_s of 0.52 Ω . In high frequency region, the plot displays a semicircle with small diameter (inset of Figure 3-2e), equivalent to a low R_{ct} , while in low frequency range, the plot shows a straight line close to imaginary axis, demonstrating a valid electrolyte diffusion. High capacitance retention of 96.6% and coulombic efficiency over 95% can be achieved even after 6000 cycles (GCD process at 20 A/g), as shown in Figure 3-2f.

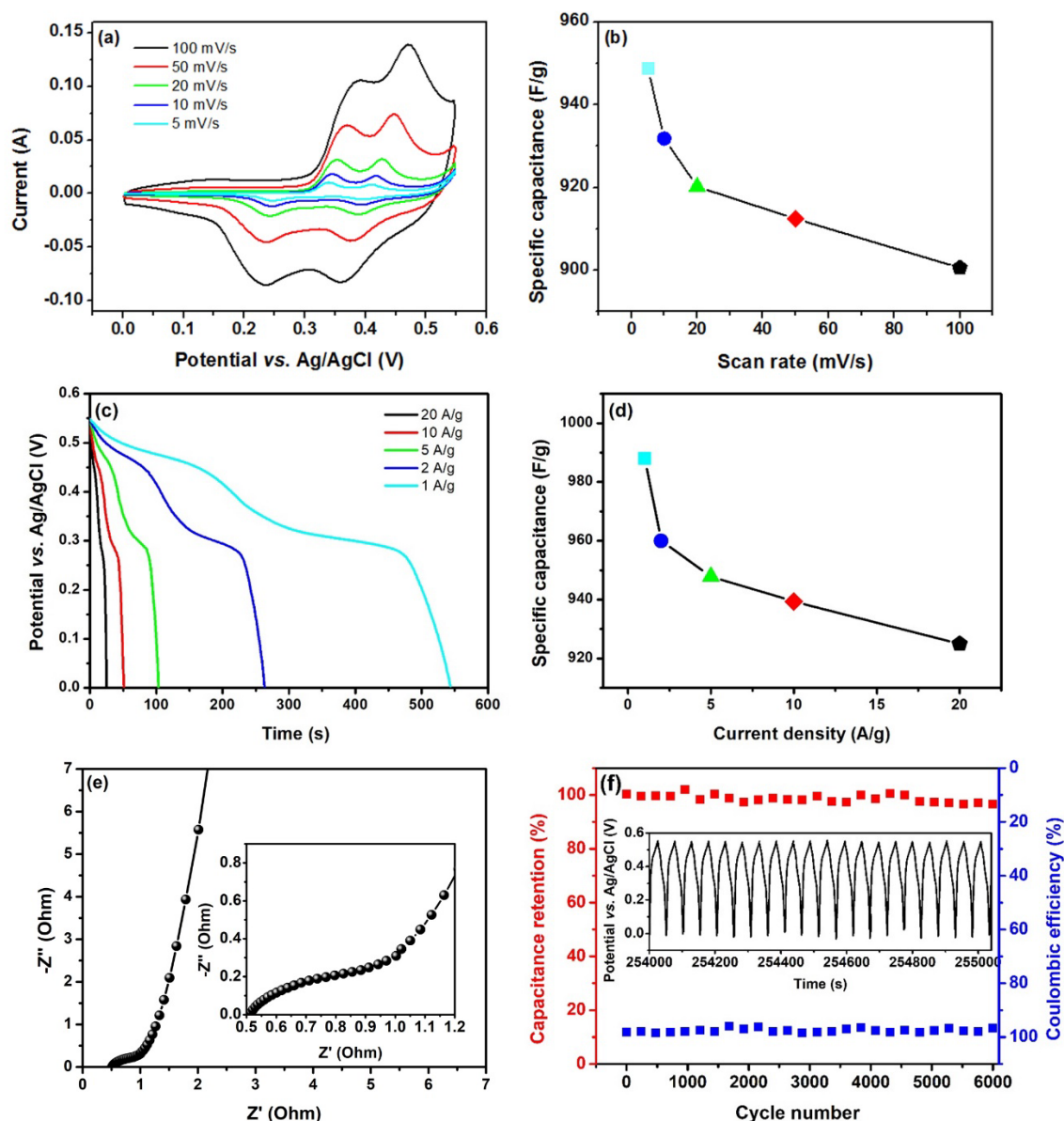


Figure 3-2 (a) CV curves and (b) corresponding SCs, (c) discharge curves and (d) corresponding SCs, (e) EIS plot and (f) cycling performance of Co_3O_4 electrode.

3.2.4 Discussion

Table 3-1 lists this work and other representative previous literatures. The Co_3O_4 electrode in this study satisfies the need of high SC, at both low and high current densities. The impressive electrochemical behaviors can be attributed to the following merits of as-synthesized Co_3O_4 : (1) the spherical morphology was well maintained in conversion of precursor to Co_3O_4 (few broken pieces); (2) the thin-wall shell is constructed by numerous nanoparticles, therefore offering increased active sites and

ensuring facile ion permeation and electron transportation; (3) the hollow nature provides a large available surface and inner area, and more importantly, can act as “ions reservoir”. The accommodated OH⁻ guarantee a relatively effective ion diffusion at high scan rate and current density. Besides, the long-term cycling stability (96.6% capacitance retention after 6000 cycles) is also competitive.

Table 3-1 SC and rate performance of Co₃O₄ based electrode materials.

Material	Specific capacitance ^a /Current density ^b	Rate capability ^c /Current density ^b	Ref.
hollow Co ₃ O ₄ spheres	342.1/0.5	69/10	[125]
hollow Co ₃ O ₄ flowers	210/0.5	86/10	[125]
hollow Co ₃ O ₄ dodecahedron	1100/1.25	40/12.5	[128]
hollow Co ₃ O ₄ nanowires	599/2	73/40	[97]
hollow Co ₃ O ₄ boxes	278/0.5	63/5	[129]
Co ₃ O ₄ spheres	261.1/0.5	42/5	[130]
Co ₃ O ₄ nanowires	977/2	49.5/10	[90]
Co ₃ O ₄ nanoflakes	450/1	81/ 20	[131]
Co ₃ O ₄ nanobooks	590/0.5	71.4/8	[132]
carbon incorporated Co ₃ O ₄	978.9/0.5	31/15	[133]
Mn doped Co ₃ O ₄	668.4/1	62/10	[120]
Au decorated Co ₃ O ₄	681/0.5	58/10	[134]
Co ₃ O ₄ /NiO	1236.7/1	67.7/20	[135]
CoO/Co ₃ O ₄	451/1	68.3/20	[136]
hollow Co ₃ O ₄ spheres	988/1	93.6/20	Ours

^a unit: F/g; ^b unit: A/g; ^c unit: %

3.3 Tunable synthesis of hollow Co_3O_4 nanoboxes

3.3.1 Sample preparation

Precipitation, solvothermal and annealing reactions were involved in the process:

- (1) The $\text{C}_4\text{H}_6\text{N}_2$ methanol solution under different molarities of 0.273, 0.102 or 0.068 M was added to 0.04 M $\text{Co}(\text{NO}_3)_2$ methanol solution. The mixed solution was kept static for 24 h. For convenient clarification, the precipitates were labelled as ZIF-67-1, ZIF-67-2 and ZIF-67-3, respectively;
- (2) 0.05 g ZIF-67 (-1, -2, -3) was dispersed in 0.01 M $\text{Co}(\text{NO}_3)_2$ methanol solution. After vigorous stirring for 10 min, the mixture was transferred to a Teflon-lined stainless-steel autoclave and kept at 120 °C for 1 h. The precipitates were denoted as Co-LDH-1, Co-LDH-2 and Co-LDH-3, respectively;
- (3) The Co-LDH (-1, -2, -3) was calcinated at 500 °C for 2 h, converting to Co_3O_4 (-1, -2, -3).

3.3.2 Material characterizations

Figure 3-3 displays the XRD patterns of the final products. The identified diffraction peaks indexed to (220), (311), (400), (511) and (440) planes at corresponding 2θ values, are in good agreement with the Co_3O_4 [126]. The crystallite sizes of Co_3O_4 -1, Co_3O_4 -2 and Co_3O_4 -3 were determined to be 23.6, 20 and 24.3 nm on the basis of Scherrer equation.

Figure 3-4a-c displays the SEM images of ZIF-67 (-1,-2,-3) synthesized from precipitation reaction. The average of ZIF-67-1, ZIF-67-2, and ZIF-67-3 are around 0.39, 1.98, and 3.28 μm . Clearly, the low concentration of $\text{C}_4\text{H}_6\text{N}_2$ contributed to large size of ZIF-67. Next, the solvothermal reaction resulted in conversion of ZIF-67 to Co-LDH, accompanying with a significant morphological evolution (vertical growing of nanosheets on the surface of ZIF-67), and the hollow structure appeared, which was caused by the dissolution of inner Co (Figure 3-4d-f). After heat treatment of Co-LDH, the hollow Co_3O_4 nanoboxes with different sizes were obtained, as observed from Figure 3-4g-i.

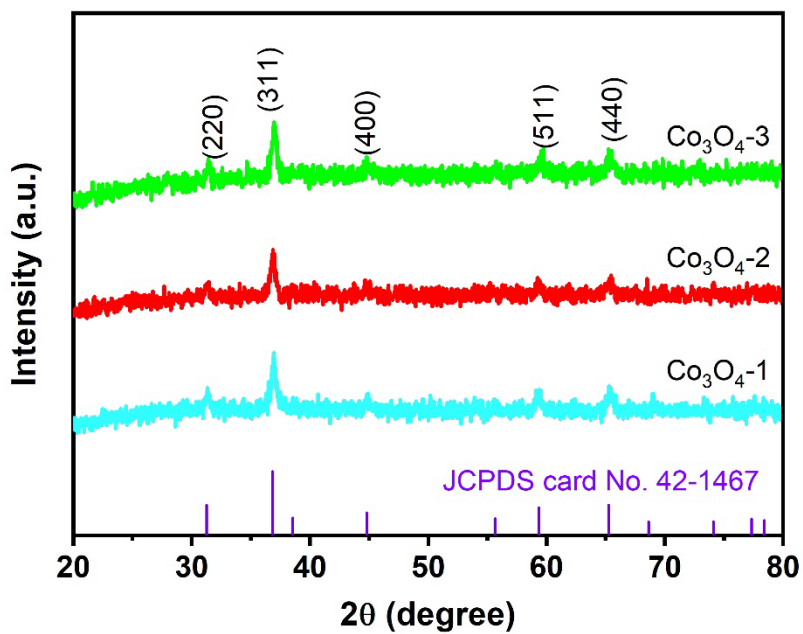


Figure 3-3 XRD patterns of Co_3O_4 (-1,-2,-3).

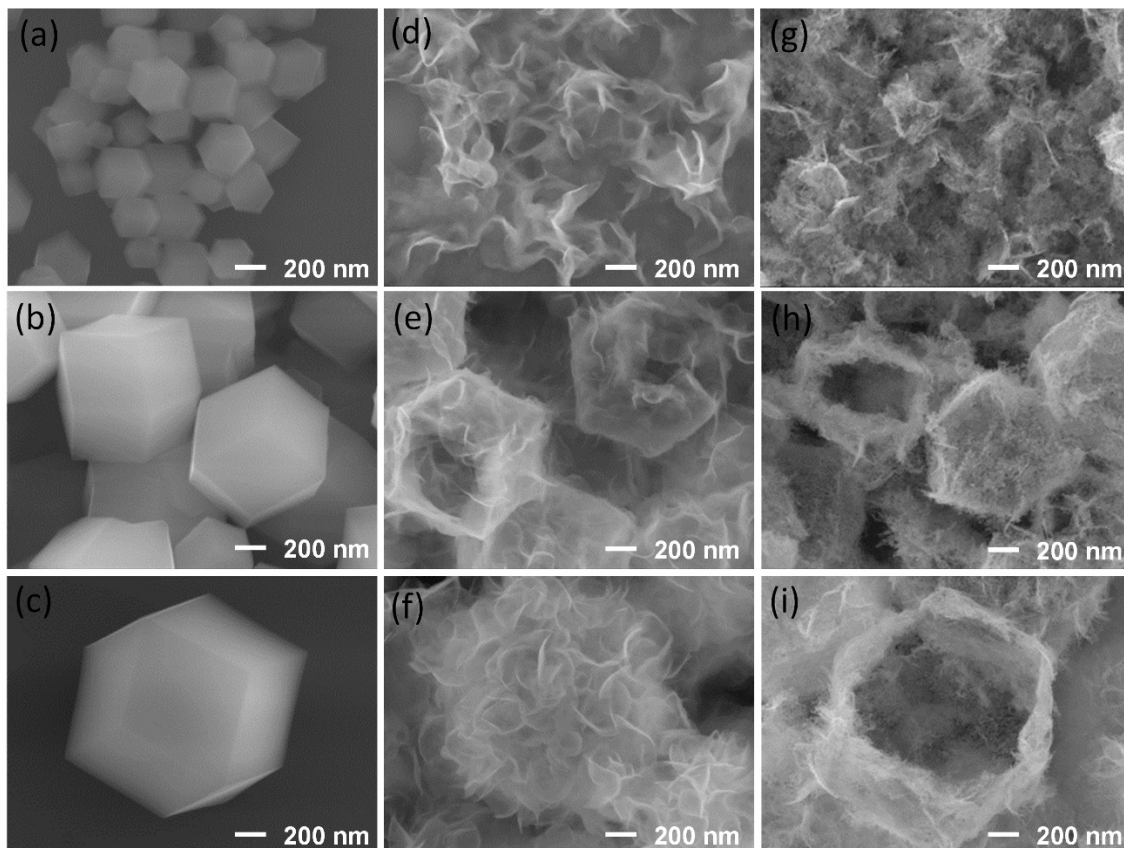


Figure 3-4 SEM images of (a) ZIF-67-1, (b) ZIF-67-2, (c) ZIF-67-3, (d) Co-LDH-1, (e) Co-LDH-2, (f) Co-LDH-3, (g) Co_3O_4 -1, (h) Co_3O_4 -2, and (i) Co_3O_4 -3.

3.3.3 Supercapacitors behaviors

The CV and GCD measurements were characterized in a potential window of 0-0.65 V. Figure 3-5a and Figure 3-5b present the CV curves at scan rate of 5 mV/s and discharge curves at current density of 1 A/g of Co_3O_4 (-1,-2,-3) electrodes, respectively. Pairs of peaks in CV curves together with evident plateaus in discharge curves jointly suggest the pseudocapacitive behaviours of as-fabricated Co_3O_4 (-1,-2,-3). In addition, in comparison of three electrodes, the Co_3O_4 -2 electrode offers largest curvilinear integrated area (CV assessment) and longest discharge time (GCD assessment). Based on Equation (12) and (13), it is can be concluded that the Co_3O_4 -2 electrode is able to deliver highest SC. The CV curves at scan rates ranging from 5-100 mV/s and discharge curves at current densities ranging from 1-20 A/g of the Co_3O_4 -2 electrode further confirms the pseudocapacitive features, as recorded in Figure 3-5c and Figure 3-5d.

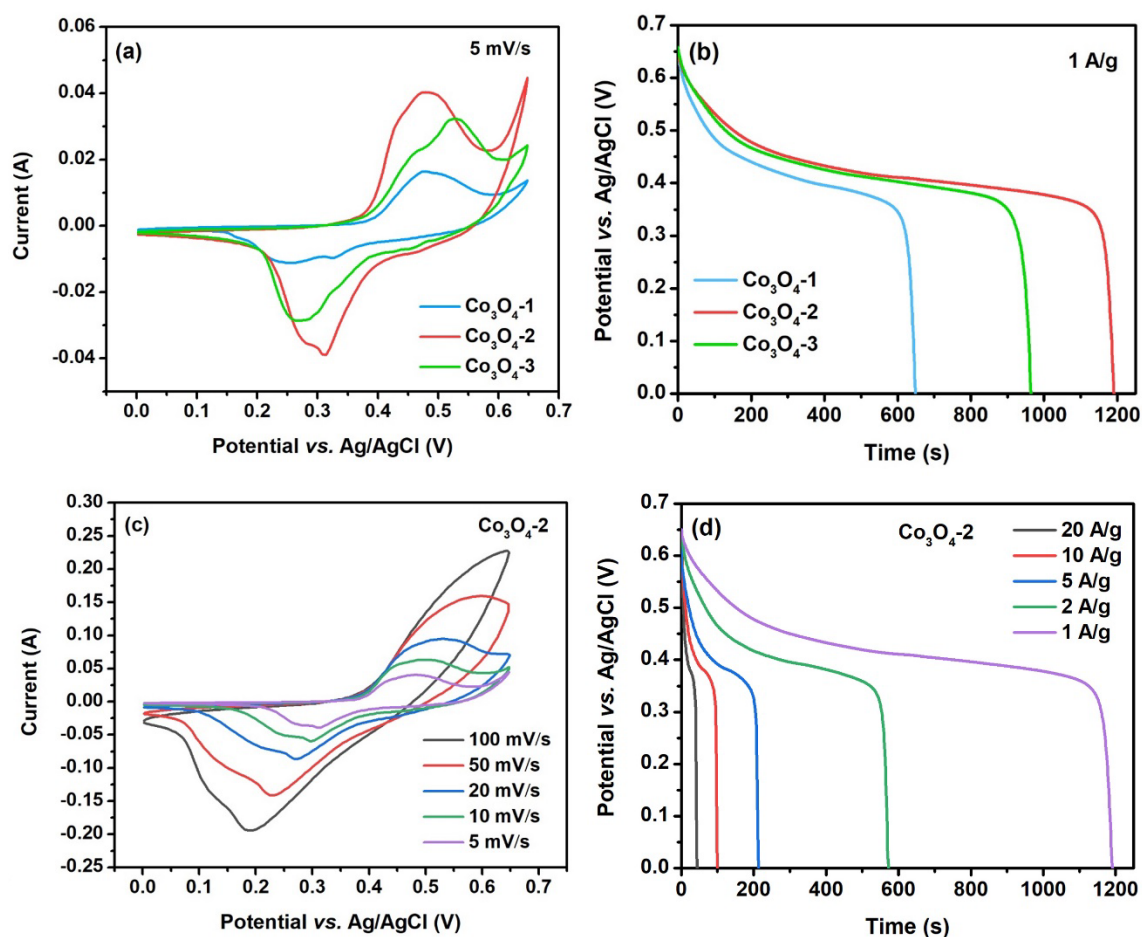


Figure 3-5 (a) CV curves at 5 mV/s and (b) discharge curves at 1 A/g of Co_3O_4 (-1,-2,-3) electrodes, (c) CV curves at different scan rates and (d) discharge curves at different current densities of Co_3O_4 -2 electrode.

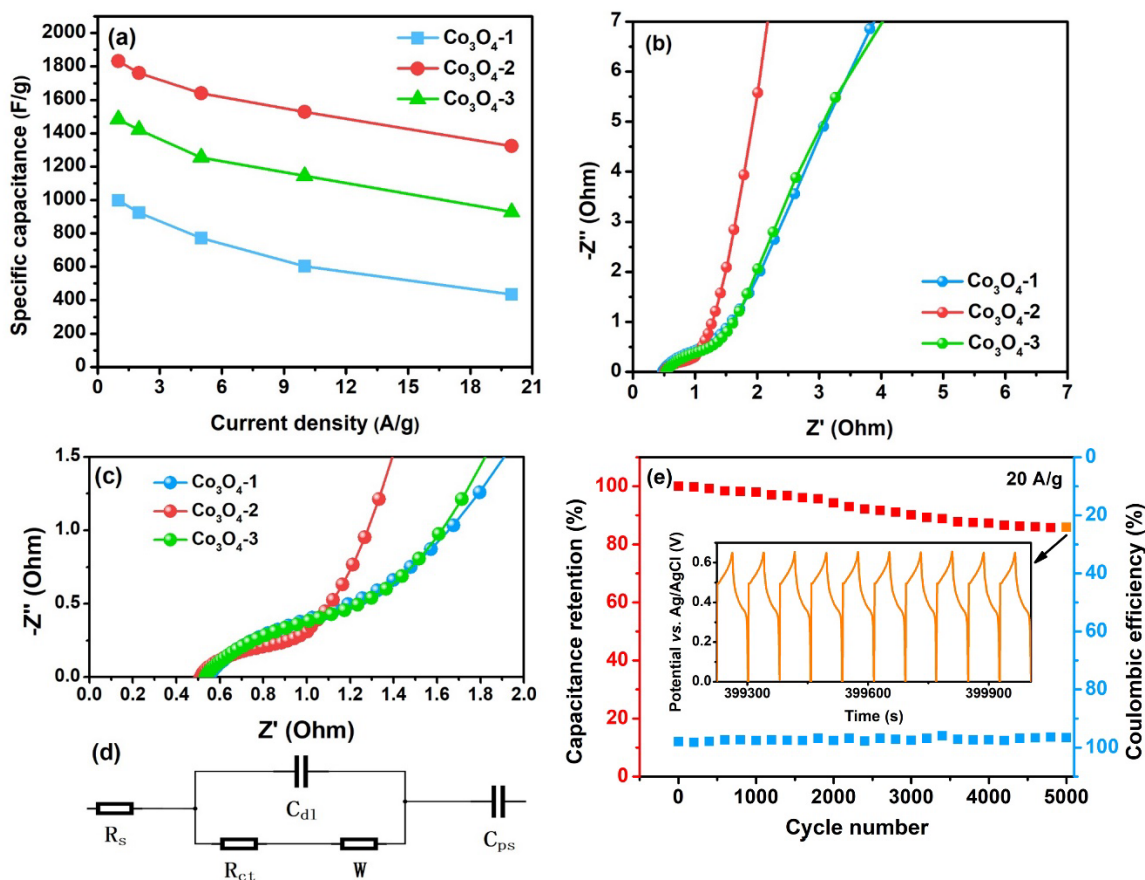


Figure 3-6 (a) SCs based on GCD tests, (b) Nyquist plots and (c) enlarged view of high frequency region of Co_3O_4 (-1,-2,-3) electrodes, (d) equivalent circuit, and (e) cycling performance of Co_3O_4 -2 electrode.

The SCs as a function of current densities for Co_3O_4 (-1,-2,-3) electrodes were exhibited in Figure 3-6a. Benefit from hollow structure of as-synthesized Co_3O_4 , the inevitable fading tendency of SCs accompanied with increase of current densities is not drastic. The fabricated Co_3O_4 -2 electrode shows the high SCs of 1832.7 and 1324.5 F/g at 1 and 20 A/g, respectively, which means 72.3% of its original capacitance is maintained. The Nyquist plots of Co_3O_4 (-1,-2,-3) electrodes characterized in frequency range of 100 mHz to 100 kHz were recorded in Figure 3-6b. The R_s values for each Co_3O_4 electrode are approximately equal due to R_s accounts for intrinsic and interface resistances. In contrast, as seen in Figure 3-6c (enlarged view of high frequency region), the Co_3O_4 -2 possesses smaller R_{ct} and larger slope than that of Co_3O_4 -1 and Co_3O_4 -3, which well coincides with its remarkable performances in CV and GCD evaluations. The equivalent circuit consisting R_s , R_{ct} , C_{dl} , Warburg element (W) and C_{ps} was illustrated in Figure 3-6d. The durability investigation (repetitive GCD tests at 20 A/g for 5000 cycles) conducted

on the Co_3O_4 -2 electrode demonstrates excellent capacitance retention of 85.9% and coulombic efficiency over 95%, as exhibited in Figure 3-6e.

3.3.4 Discussion

Table 3-2 SCs at low and high current densities of Co_3O_4 based electrode materials.

Material	Specific capacitance ^a / Low current density ^b	Specific capacitance ^a / High current density ^b	Ref.
hollow Co_3O_4 3D-nanonet	739/1	533/15	[96]
hollow Co_3O_4 spheres	474.8/1	377.4/10	[127]
hollow Co_3O_4 corals	527/1	412/10	[139]
hollow Co_3O_4 nanotubes	1006/1	512/10	[93]
hollow Co_3O_4 cages	948.9/1	536.8/40	[94]
Co_3O_4 spheres	837.7/1	783.7/10	[140]
Co_3O_4 nanosheets	1121/1	873/25	[141]
Co_3O_4 nanoplates	355.6/0.4	230/4	[142]
Co_3O_4 nanofibers	340/1	296/10	[143]
Mn doped Co_3O_4	773/1	485/16	[144]
$\text{Co}_3\text{O}_4/\text{CoMoO}_4$	1902/1	1200/10	[145]
$\text{Co}_3\text{O}_4/\text{Ni}(\text{OH})_2$	1306.3/1.2	600/12.1	[146]
graphene/ Co_3O_4	1765/1	1266/20	[147]
$\text{NiO}/\text{Co}_3\text{O}_4/\text{MnO}_2$	1055.3/0.2	727.4/4	[148]
hollow Co_3O_4 nanoboxes	1832.7/1	1324.5/20	Ours

^a unit: F/g; ^b unit: A/g

In this study, the sizes of the hollow Co_3O_4 nanoboxes can be controlled by tailoring the concentration of $\text{C}_4\text{H}_6\text{N}_2$ thanks to the formation mechanism of ZIF-67 divided into two phases: nucleation and growth. Specifically, in nucleation stage, the high concentration of $\text{C}_4\text{H}_6\text{N}_2$ corresponds to the fast nucleation rate, as a consequence giving rise to the small unit cell. In growth stage, particles grew around the cell and the ZIF-67 was formed

[137,138]. For Co_3O_4 -2 and Co_3O_4 -3, structures were well inherited in subsequent solvothermal reaction and calcination process, while For Co_3O_4 -1, mass structures collapsed, significantly affecting the electrochemical performances. Compared with Co_3O_4 -3, the Co_3O_4 -2 delivers relatively small size and thin shell, contributing to better supercapacitors behaviours. Beyond expectation, the SC of Co_3O_4 -2 electrode at 20 A/g, going up to 1324.5 F/g, is higher than that of some Co_3O_4 electrodes in previous literatures at 1 A/g, as illustrated in Table3-2.

3.4 Morphology-controlled synthesis of Ni-Co binary hydroxide

3.4.1 Sample preparation

Ni-Co binary hydroxide was grown on nickel foam through a one-step process, as illustrated below:

- (1) NF as a substrate was sequentially pretreated with 6 M HCl, deionized water and ethanol;
- (2) 5mmol mixture of $\text{Ni}(\text{NO}_3)_2 \cdot 6\text{H}_2\text{O}$ and $\text{Co}(\text{NO}_3)_2 \cdot 6\text{H}_2\text{O}$ under concentration ratios of 9:1, 7:3, 5:5, 3:7 and 1:9, 2 mmol NH_4F , 6 mmol $\text{CO}(\text{NH}_2)_2$ were dissolved in 50 mL deionized water;
- (3) The precursor solution and NF were transferred to a Teflon-lined stainless-steel autoclave and kept at 120 °C for 8 h. For convenience, the final products were named as $\text{Ni}_{1-x}\text{Co}_x(\text{OH})_2$ ($x=0.1, 0.3, 0.5, 0.7$ and 0.9).

3.4.2 Material characterizations

The SEM image of bare NF (Figure 3-7a) reveals the NF possesses a highly porous 3D network. As observed from Figure 3-7b-f, the binary material displays a distinct morphological evolution. Specifically, when Ni is dominant (Figure 3-7b), the composite exhibits flower-like structures. At Ni/Co ratio of 7:3 (Figure 3-7c), the flower-like structures were replaced by nanosheet structures. Next, an integrated geometry (nanosheets encapsulated with nanowires) was obtained at intermediate ratio (Figure 3-7d). The morphology evolved to nanowire at Ni/Co ratio of 3:7 (Figure 3-7e) and partial

nanowires aggregated at greater Co content (Figure 3-7f). The morphological change is attributed to the competition of Ni^{2+} and Co^{2+} for OH^- in synthesis process [149].

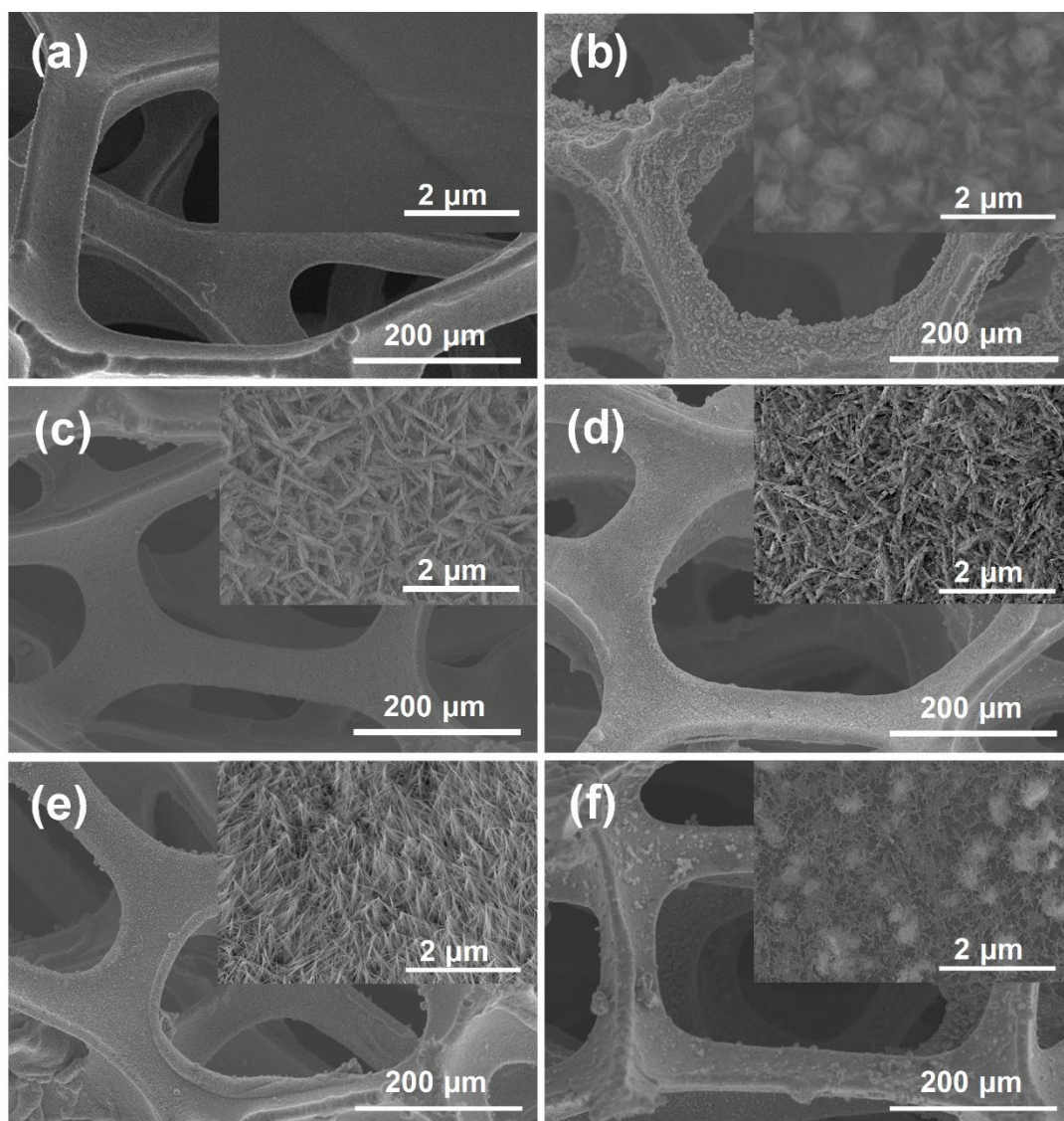


Figure 3-7 SEM images of samples at Ni/Co ratios of (a) bare NF, (b) 9:1, (c) 7:3, (d) 5:5, (e) 3:7, and (f) 1:9.

The XRD patterns of all samples were depicted in Figure 3-8, where the diffraction peaks can be indexed to the $\text{Ni}(\text{OH})_2$ (JCPDS No.14-0117) and the $\text{Co}(\text{OH})_2$ (JCPDS No. 30-0443). At greater Co to Ni ratio, partial peaks became weaker or dim because of the low crystallinity of $\text{Ni}_{0.3}\text{Co}_{0.7}(\text{OH})_2$ and $\text{Ni}_{0.1}\text{Co}_{0.9}(\text{OH})_2$ [150]. The XPS was conducted on $\text{Ni}_{0.5}\text{Co}_{0.5}(\text{OH})_2$. Briefly, in typical survey spectrum (Figure 3-9a), C (due to air exposure), Ni, Co and O were observed. Further, the peaks of Ni $2p_{3/2}$ and Ni $2p_{1/2}$ at 855.6 and 873.5 eV with energy gap of 17.9 eV (Figure 3-9b), the peaks of Co $2p_{3/2}$ and Co $2p_{1/2}$ at

781.4 and 796.9 eV with energy gap of 15.5 eV (Figure 3-9c), the peak at 531.1 eV (Figure 3-9d) identify Ni²⁺, Co²⁺ and OH⁻, respectively [4,151-153].

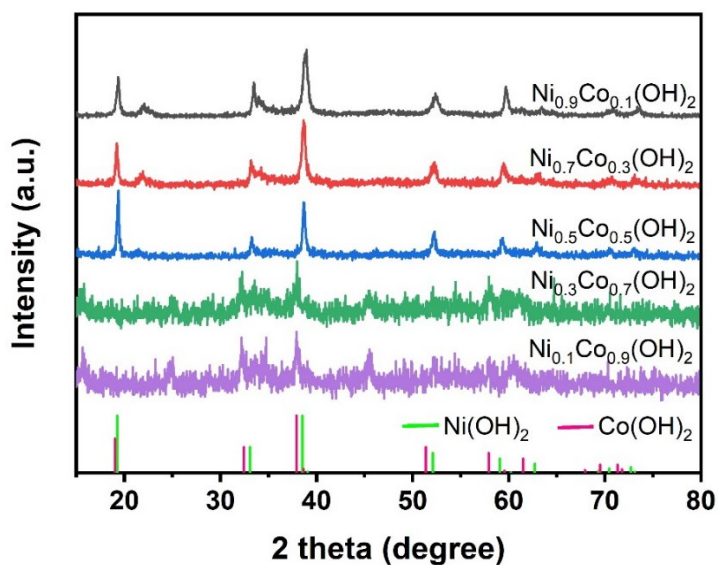


Figure 3-8 XRD patterns of Ni_{1-x}Co_x(OH)₂.

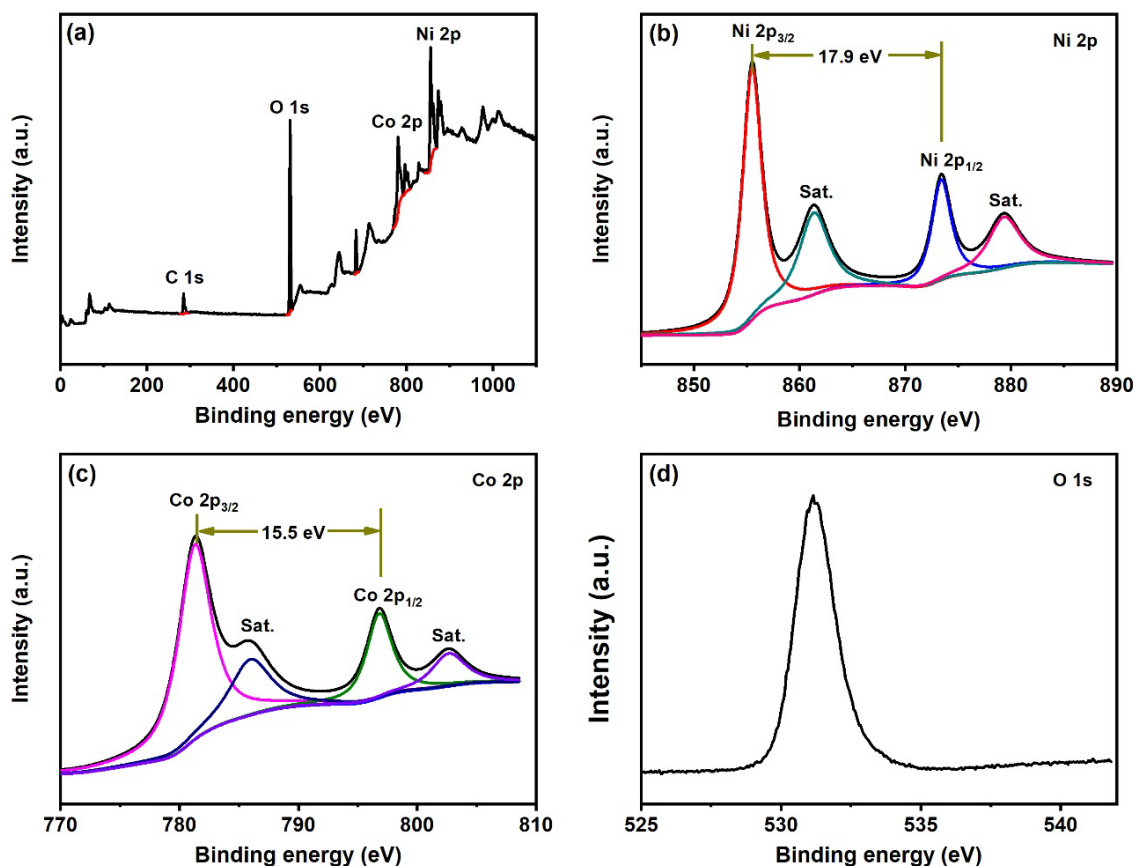


Figure 3-9 XPS spectra of Ni_{0.5}Co_{0.5}(OH)₂: (a) survey spectrum, (b) Ni 2p, (c) Co 2p, and (d) O 1s.

3.4.3 Supercapacitors behaviors

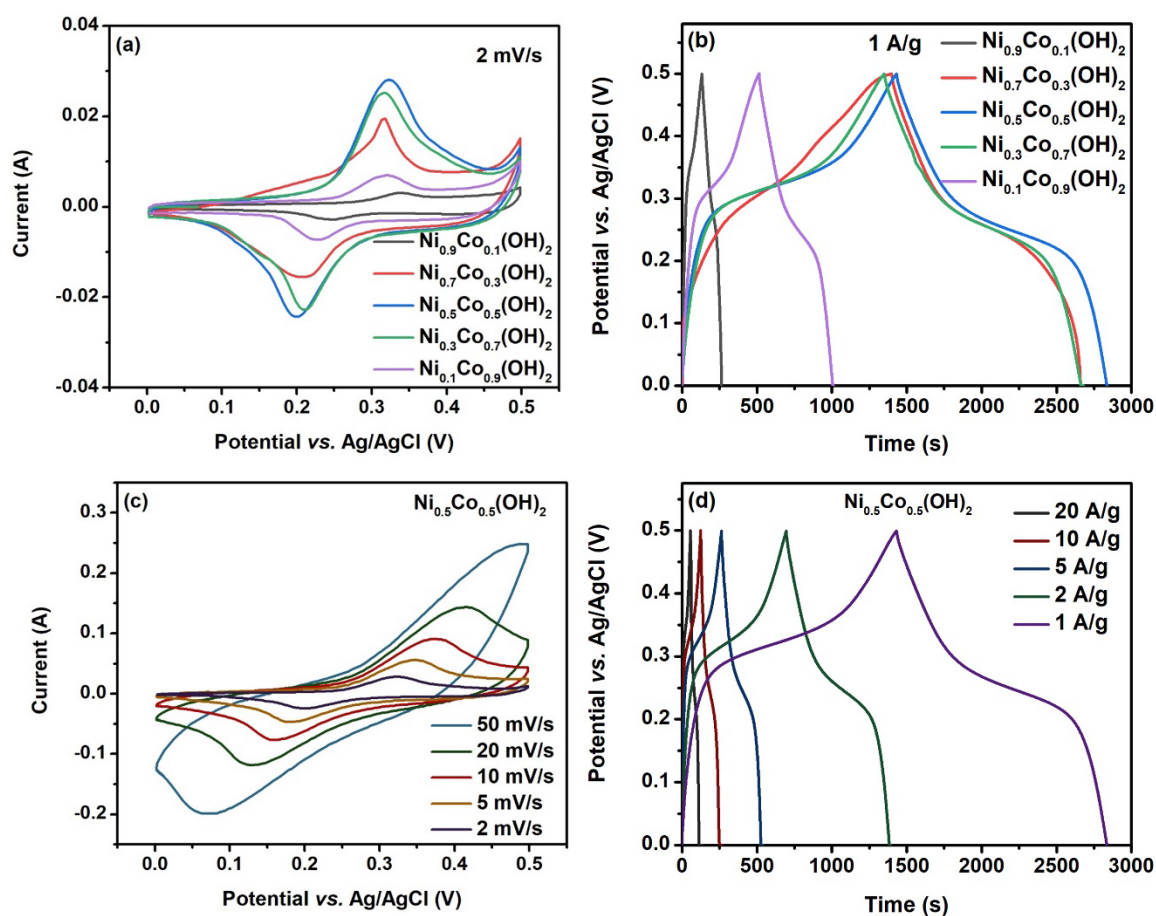


Figure 3-10 (a) CV curves at 2 mV/s and (b) GCD curves at 1 A/g of $\text{Ni}_{1-x}\text{Co}_x(\text{OH})_2$ electrodes, (c) CV curves at different scan rates and (d) GCD curves at different current densities of $\text{Ni}_{0.5}\text{Co}_{0.5}(\text{OH})_2$ electrode.

In systematical electrochemical tests, thanks to binder-free feature, the fabricated electrode ($\text{Ni}_{1-x}\text{Co}_x(\text{OH})_2$ on NF) can be employed as WE directly. The CV curves of five electrodes at scan rate of 2 mV/s were exhibited in Figure 3-10a. The pairs of peaks standing for three reversible faradaic redox reactions ($\text{Ni}^{2+}/\text{Ni}^{3+}$, $\text{Co}^{2+}/\text{Co}^{3+}$ and $\text{Co}^{3+}/\text{Co}^{4+}$) identify the pseudocapacitive characteristics of the $\text{Ni}_{1-x}\text{Co}_x(\text{OH})_2$. Additionally, since SC is proportional to the integrated area at a defined scan rate, it can be concluded that the $\text{Ni}_{0.5}\text{Co}_{0.5}(\text{OH})_2$ electrode reaches the largest SC, which is consistent with the GCD measurements at 1 A/g seen in Figure 3-10b. Particularly, owing to lower transition potential of Co [149,154], the boost in Co content generated a shift of anodic peaks to lower potential. Further, the CV tests at various scan rates and GCD measurements at different current densities were performed on the $\text{Ni}_{0.5}\text{Co}_{0.5}(\text{OH})_2$

electrode, as displayed in Figure 3-10c and Figure 3-10d. The CV curves show a negligible distortion from low to high scan rate, which demonstrates an excellent rate capability.

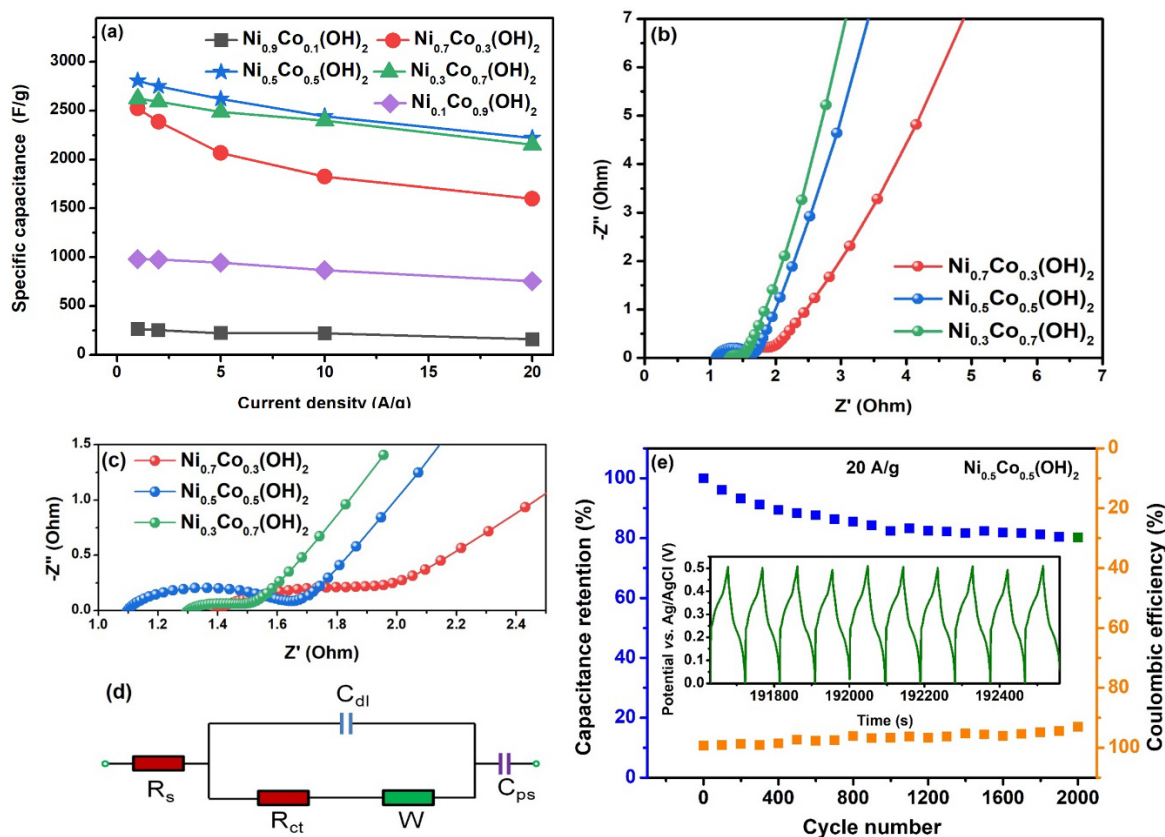


Figure 3-11 (a) SCs based on GCD tests of $\text{Ni}_{1-x}\text{Co}_x(\text{OH})_2$ electrodes, (b) Nyquist plots and (c) enlarged view of high frequency region of $\text{Ni}_{0.7}\text{Co}_{0.3}(\text{OH})_2$, $\text{Ni}_{0.5}\text{Co}_{0.5}(\text{OH})_2$ and $\text{Ni}_{0.3}\text{Co}_{0.7}(\text{OH})_2$ electrodes, (d) equivalent circuit, and (e) cycling performance of $\text{Ni}_{0.5}\text{Co}_{0.5}(\text{OH})_2$ electrode.

The SCs of $\text{Ni}_{1-x}\text{Co}_x(\text{OH})_2$ electrode calculated according to GCD results were plotted in Figure 3-11a. The aggregation of materials observed from SEM images of Figure 3-7b and Figure 3-7f led to the poor SC performances of $\text{Ni}_{0.9}\text{Co}_{0.1}(\text{OH})_2$ and $\text{Ni}_{0.1}\text{Co}_{0.9}(\text{OH})_2$. The highest SCs at corresponding current densities were reached at intermediate ratio of Ni and Co, which coincides with previous reports [155,156]. The $\text{Ni}_{0.5}\text{Co}_{0.5}(\text{OH})_2$ electrode exhibits SC of 2807 F/g at 1 A/g and capacitance loss of 20.8% at 20 A/g. It is worth noting that the $\text{Ni}_{0.3}\text{Co}_{0.7}(\text{OH})_2$ electrode delivers a better rate performance (2624 F/g at 1 A/g and capacitance loss of 18% at 20 A/g) thanks to its one-dimensional (1D) morphology [149,157]. Figure 3-11b shows the typical Nyquist plots over frequency range of 100 mHz to 100 kHz of $\text{Ni}_{0.7}\text{Co}_{0.3}(\text{OH})_2$, $\text{Ni}_{0.5}\text{Co}_{0.5}(\text{OH})_2$ and $\text{Ni}_{0.3}\text{Co}_{0.7}(\text{OH})_2$ electrodes. Figure 3-11c is the enlarge view of high frequency region and Figure 3-11d

is the equivalent circuit. Among three electrodes, the $\text{Ni}_{0.3}\text{Co}_{0.7}(\text{OH})_2$ electrode possesses the smallest R_{ct} and the largest slope, corresponding to its outstanding rate capability, while the $\text{Ni}_{0.5}\text{Co}_{0.5}(\text{OH})_2$ electrode delivers the smallest R_s , together with its feasible synergistic contribution, determining its highest SC. The repetitive GCD tests at 20 A/g were operated on $\text{Ni}_{0.5}\text{Co}_{0.5}(\text{OH})_2$ electrode to assess the stability. As shown in Figure 3-11e, even after 2000 cycles, the capacitance loss is only 19.8% and the coulombic efficiency still exceeds 90%.

3.4.4 Discussion

In summary, the superior SC performance of $\text{Ni}_{0.5}\text{Co}_{0.5}(\text{OH})_2$ electrode can be attributed to the following advantages: (1) in the proposed one-step synthesis, no binder was involved. In other words, the $\text{Ni}_{0.5}\text{Co}_{0.5}(\text{OH})_2$ was grown on NF directly, which contributes to a good electric contact; (2) straightforwardly, the unique morphology (nanosheets encapsulated with nanowires) provides a large surface area as well as increased electroactive sites; (3) owing to introduction of Co, the oxidation peak deviates from the voltage window limit, avoiding possible solvent oxidation; (4) because of the mixed uniformity of Ni and Co in as-prepared $\text{Ni}_{0.5}\text{Co}_{0.5}(\text{OH})_2$, the redox peaks show overlapping characteristic, thereby broadening the redox feature; (5) the most active sites led by valence interchange or charge hopping possibly is obtained at Ni/Co ratio of 5:5 [158]. Impressively, the SC in this study is even beyond some hybrid materials [159-161]. Except for remarkable SC, the excellent rate and cycling performances, comparable loading mass (1.5 mg/cm^2) and facile method (one-step hydrothermal route) further manifest the bright commercial prospect of the fabricated electrode.

3.5 Flower-like ZnWO_4 for supercapacitors

3.5.1 Sample preparation

A hydrothermal route was employed to synthesize ZnWO_4 , as described below:

(1) A solution containing 1 mmol $\text{Zn}(\text{NO}_3)_2 \cdot 6\text{H}_2\text{O}$, 1 mmol $\text{Na}_2\text{WO}_4 \cdot 2\text{H}_2\text{O}$, 8 mmol NH_4F and 50 mL deionized water was prepared;

- (2) The resulting solution was transferred to a Teflon-lined stainless-steel autoclave and kept at 120 °C for 8 h;
- (3) The obtained precipitates were dried and heat treated at 600 °C for 6 h.

3.5.2 Material characterizations and supercapacitors behaviors

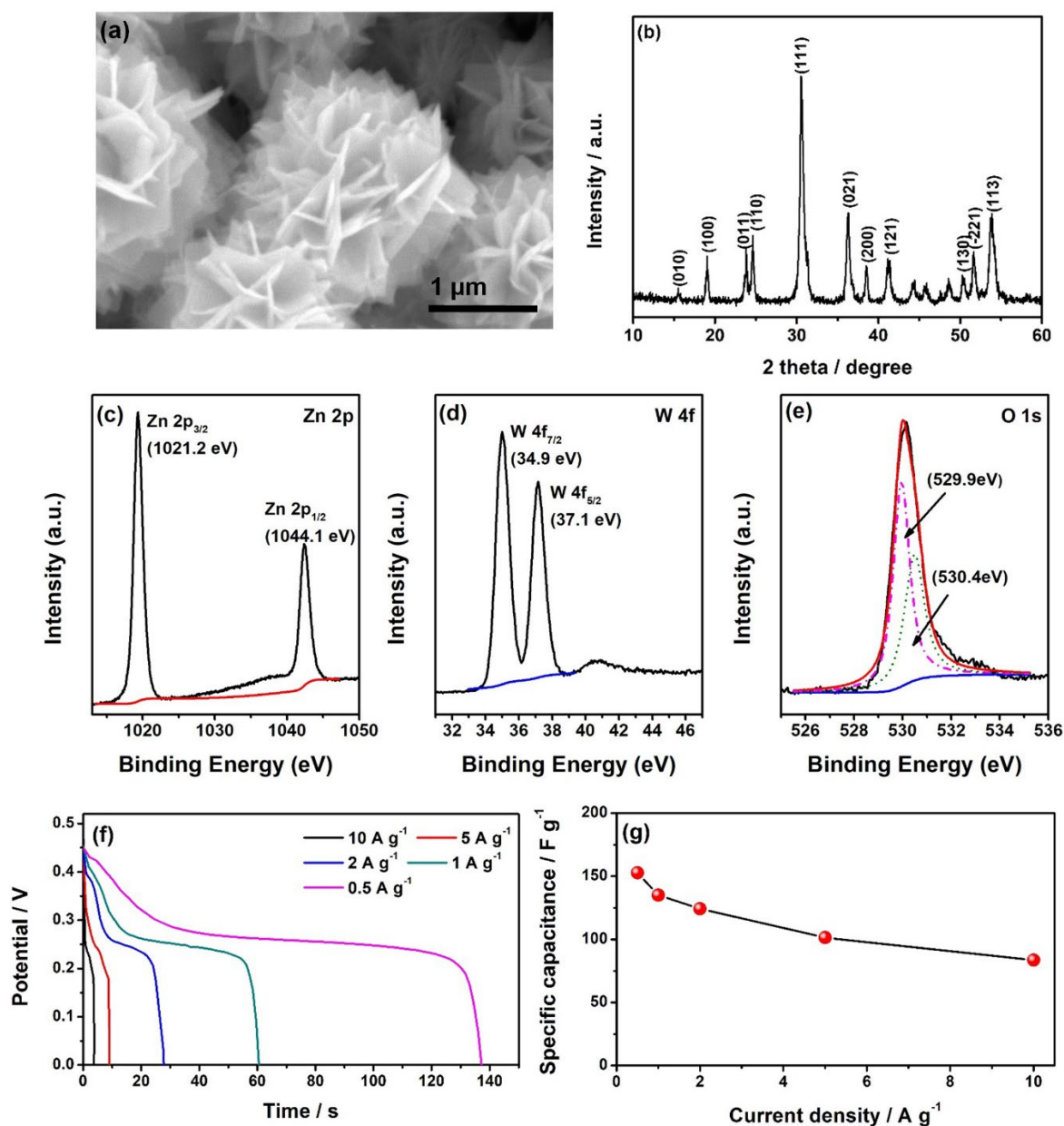


Figure 3-12 (a) SEM image, (b) XRD patterns, XPS spectra: (c) Zn 2p, (d) W 4f and (e) O 1s, (f) discharge curves and (g) corresponding SCs of flower-like ZnWO₄.

As observed from Figure 3-12a, the synthesized material presents a flower-like structure constructed by intersected uniform nanoflakes. Figure 3-12b shows the XRD patterns of the sample. The diffraction peaks are well matched to the ZnWO_4 . Moreover, the highlight sharp peak at (111) plane identifies high crystalline of the sample [162]. The core-level XPS spectra of Zn 2p, W 4f and O 1s were plotted in Figure 3-12c, Figure 3-12d and Figure 3-12e, respectively. For Zn 2p, the peaks locate at 1021.2 and 1044.1 eV; for W 4f, the peaks appear at 34.9 and 37.1 eV; for O 1s, the two peaks at 529.9 and 530.4 eV can be attributed to oxygen and hydroxyl groups [119,163,164]. To sum up, all peaks at corresponding binding energies further indicate the successful synthesis of ZnWO_4 . The discharge curves at various current densities and calculated SCs of the ZnWO_4 electrode were exhibited in Figure 3-12f and Figure 3-12g, respectively. The ZnWO_4 electrode displays a SC of 152.8 F/g at 0.5 A/g.

4 Conclusion and future work

This thesis focus on overcoming the defects of Co_3O_4 , $\text{Ni}(\text{OH})_2$ and $\text{Co}(\text{OH})_2$ utilized in PsCs in previous progress. To address the issue that Co_3O_4 suffers from low rate capability, hollow Co_3O_4 spheres were synthesized. The electrochemical measurements reveal that the Co_3O_4 electrode displays a high SC of 988 F/g and of particular importance is that only 6.4% of the initial value decays at 20 A/g, equivalent to an excellent rate performance, which can be attributed to hollow nature, highly porous morphology, thin-wall feature and so forth. Further, two phases named as nucleation and growth in formation of ZIF-67 were thoroughly investigated. In synthesis of hollow Co_3O_4 nanoboxes, the size adjustment was achieved through tuning concentration of 2-methylimidazole in initial precipitation reaction. The facile route provides a new viewpoint for optimization of hollow Co_3O_4 . The optimized electrode delivers high SCs going up to 1832.7 and 1324.5 F/g at 1 and 20 A/g respectively. Aiming at the drawback that the Ni-Co binary hydroxide fails to exhibit satisfied overall supercapacitors performances, a novel approach was proposed, by which the Ni-Co binary hydroxide could grow on NF directly (binder-free) and the morphology evolving from nanosheet to nanowire was controllable. The electrode at Ni/Co ratio of 5:5 exhibits high SCs of 2807 and 2222 F/g at 1 and 20 A/g and retains 80.2% of its original capacitance after 2000 cycles. Besides, the simple one-step method is also significant for commercial application. Last, the supercapacitors behaviors of flower-like ZnWO_4 , a potential alternative electrode material in the future, were studied.

Straightforwardly compared the spheres, nanoboxes, nanosheets encapsulated with nanowires and nanoflowers , it can be seen that they simultaneously exhibit common merits such as stable architecture, large accessible surface area, increased electroactive sites and so forth. Especially, $\text{Ni}_{0.5}\text{Co}_{0.5}(\text{OH})_2$ electrode stands out among them. It can be attributed to following unparalleled advantages like the overwhelming SC, the largest loading mass and particularly the facile one-step synthesis, which manifests the great potential of the obtained electrode for mass production and commercial application in the future.

In future study, the following aspects are worth noting: (1) prepare full packaged prototype devices to further illuminate the supercapacitors behaviors of the fabricated electrodes; (2) try to adopt the obtained materials to wide applications such as catalysts and sensors; (3) particularly, the pseudocapacitive mechanism still remains controversial up to now. The in-situ study of the mechanism is necessary.

References

- [1] K. N. Hui, K. San Hui, Z. Tang, V. V. Jadhav, and Q. X. Xia, "Hierarchical chestnut-like MnCo_2O_4 nanoneedles grown on nickel foam as binder-free electrode for high energy density asymmetric supercapacitors," *Journal of Power Sources*, vol. 330, pp. 195-203, 2016.
- [2] L. Cui, L. Huang, M. Ji, Y. Wang, H. Shi, Y. Zuo, and S. Kang, "High-performance MgCo_2O_4 nanocone arrays grown on three-dimensional nickel foams: preparation and application as binder-free electrode for pseudo-supercapacitor," *Journal of Power Sources*, vol. 333, pp. 118-124, 2016.
- [3] H. Wang, H. S. Casalongue, Y. Liang, and H. Dai, " $\text{Ni}(\text{OH})_2$ nanoplates grown on graphene as advanced electrochemical pseudocapacitor materials," *Journal of the American Chemical Society*, vol. 132, pp. 7472-7477, 2010.
- [4] A. Roy, H. S. Jadhav, G. M. Thorat, and J. G. Seo, "Electrochemical growth of $\text{Co}(\text{OH})_2$ nanoflakes on Ni foam for methanol electro-oxidation," *New Journal of Chemistry*, vol. 41, pp. 9546-9553, 2017.
- [5] S. M. Pourmortazavi, M. Rahimi-Nasrabadi, M. S. Karimi, and S. Mirsadeghi, "Evaluation of photocatalytic and supercapacitor potential of nickel tungstate nanoparticles synthesized by electrochemical method," *New Journal of Chemistry*, vol. 42, pp. 19934-19944, 2018.
- [6] S. Vazquez, S. M. Lukic, E. Galvan, L. G. Franquelo, and J. M. Carrasco, "Energy storage systems for transport and grid applications," *IEEE Transactions on Industrial Electronics*, vol. 57, pp. 3881-3895, 2010.
- [7] B. Kale and S. Chatterjee, "Electrochemical energy storage systems: India perspective," *Bulletin of Materials Science*, vol. 43, pp. 1-15, 2020.
- [8] H. Lu, J. Chen, and Q. Tian, "Wearable high-performance supercapacitors based on Ni-coated cotton textile with low-crystalline Ni-Al layered double hydroxide nanoparticles," *Journal of colloid and interface science*, vol. 513, pp. 342-348, 2018.
- [9] T. Kousksou, P. Bruel, A. Jamil, T. El Rhafiki, and Y. Zeraouli, "Energy storage: Applications and challenges," *Solar Energy Materials and Solar Cells*, vol. 120, pp. 59-80, 2014.
- [10] J. M. Carrasco, L. G. Franquelo, J. T. Bialasiewicz, E. Galván, R. C. PortilloGuisado, M. M. Prats, J. I. Leon, and N. Moreno-Alfonso, "Power-electronic systems for the grid integration of renewable energy sources: A survey," *IEEE Transactions on industrial electronics*, vol. 53, pp. 1002-1016, 2006.
- [11] M. S. Guney and Y. Tepe, "Classification and assessment of energy storage systems," *Renewable and Sustainable Energy Reviews*, vol. 75, pp. 1187-1197, 2017.
- [12] A. Chauhan and R. P. Saini, "A review on Integrated Renewable Energy System based power generation for stand-alone applications: Configurations, storage options, sizing methodologies and control," *Renewable and Sustainable Energy Reviews*, vol. 38, pp. 99-120, 2014.

- [13] L. Wang, Y. Han, X. Feng, J. Zhou, P. Qi, and B. Wang, "Metal–organic frameworks for energy storage: Batteries and supercapacitors," *Coordination Chemistry Reviews*, vol. 307, pp. 361-381, 2016.
- [14] L. Zhang, X. Hu, Z. Wang, F. Sun, and D. G. Dorrell, "A review of supercapacitor modeling, estimation, and applications: A control/management perspective," *Renewable and Sustainable Energy Reviews*, vol. 81, pp. 1868-1878, 2018.
- [15] C. Wang, E. Zhou, W. He, X. Deng, J. Huang, M. Ding, X. Wei, X. Liu, and X. Xu, "NiCo₂O₄-based supercapacitor nanomaterials," *Nanomaterials*, vol. 7, pp. 41, 2017.
- [16] M. Vangari, T. Pryor, and L. Jiang, "Supercapacitors: review of materials and fabrication methods," *Journal of Energy Engineering*, vol. 139, pp. 72-79, 2013.
- [17] R. Kötz and M. J. E. A. Carlen, "Principles and applications of electrochemical capacitors," *Electrochimica Acta*, vol. 45, pp. 2483-2498, 2000.
- [18] W. Zuo, R. Li, C. Zhou, Y. Li, J. Xia, and J. Liu, "Battery-supercapacitor hybrid devices: recent progress and future prospects," *Advanced Science*, vol. 4, pp. 1600539, 2017.
- [19] H. Gao, F. Xiao, C. B. Ching, and H. Duan, "High-performance asymmetric supercapacitor based on graphene hydrogel and nanostructured MnO₂," *ACS applied materials & interfaces*, vol. 4, pp. 2801-2810, 2012.
- [20] J. Yan, Z. Fan, W. Sun, G. Ning, T. Wei, Q. Zhang, R. Zhang, L. Zhi, and F. Wei, "Advanced asymmetric supercapacitors based on Ni(OH)₂/graphene and porous graphene electrodes with high energy density," *Advanced Functional Materials*, vol. 22, pp. 2632-2641, 2012.
- [21] P. Yang, X. Xiao, Y. Li, Y. Ding, P. Qiang, X. Tan, W. Mai, Z. Lin, W. Wu, T. Li, H. Jin, P. Liu, J. Zhou, C. P. Wong, and Z. L. Wang, "Hydrogenated ZnO core–shell nanocables for flexible supercapacitors and self-powered systems," *ACS nano*, vol. 7, pp. 2617-2626, 2013.
- [22] V. D. Nithya and N. S. Arul, "Review on α -Fe₂O₃ based negative electrode for high performance supercapacitors," *Journal of Power Sources*, vol. 327, pp. 297-318, 2016.
- [23] L. Feng, Y. Zhu, H. Ding, and C. Ni, "Recent progress in nickel based materials for high performance pseudocapacitor electrodes," *Journal of Power Sources*, vol. 267, pp. 430-444, 2014.
- [24] A. González, E. Goikolea, J. A. Barrena, and R. Mysyk, "Review on supercapacitors: technologies and materials," *Renewable and Sustainable Energy Reviews*, vol. 58, pp. 1189-1206, 2016.
- [25] A. G. Pandolfo and A. F. Hollenkamp, "Carbon properties and their role in supercapacitors," *Journal of power sources*, vol. 157, pp. 11-27, 2006.
- [26] X. Zang, R. Zhang, Z. Zhen, W. Lai, C. Yang, F. Kang, and H. Zhu, "Flexible, temperature-tolerant supercapacitor based on hybrid carbon film electrodes," *Nano Energy*, vol. 40, pp. 224-232, 2017.
- [27] R. Kötz, M. Hahn, and R. Gallay, "Temperature behavior and impedance fundamentals of supercapacitors," *Journal of Power Sources*, vol. 154, pp. 550-555, 2006.

- [28] J. Yi, U. S. Kim, C. B. Shin, T. Han, and S. Park, "Modeling the temperature dependence of the discharge behavior of a lithium-ion battery in low environmental temperature," *Journal of Power Sources*, vol. 244, pp. 143-148, 2013.
- [29] D. P. Abraham, J. R. Heaton, S. H. Kang, D. W. Dees, and A. N. Jansen, "Investigating the low-temperature impedance increase of lithium-ion cells," *Journal of The Electrochemical Society*, vol. 155, pp. A41-A47, 2008.
- [30] Z. Tang, C. H. Tang, and H. Gong, "A high energy density asymmetric supercapacitor from nano-architected Ni(OH)₂/Carbon nanotube electrodes," *Advanced Functional Materials*, vol. 22, pp. 1272-1278, 2012.
- [31] K. Sheng, Y. Sun, C. Li, W. Yuan, and G. Shi, "Ultrahigh-rate supercapacitors based on electrochemically reduced graphene oxide for ac line-filtering," *Scientific reports*, vol. 2, pp. 247, 2012.
- [32] D. Sauerteig, S. Ivanov, H. Reinshagen, and A. Bund, "Reversible and irreversible dilation of lithium-ion battery electrodes investigated by in-situ dilatometry," *Journal of Power Sources*, vol. 342, pp. 939-946, 2017.
- [33] J. Lang, "Study on metal oxide and its composite materials for supercapacitor electrode," *Ph.D Dissertation*, Lanzhou University of Technology, China, 2010.
- [34] A. Castaings, W. Lhomme, R. Trigui, and A. Bouscayrol, "Comparison of energy management strategies of a battery/supercapacitors system for electric vehicle under real-time constraints," *Applied Energy*, vol. 163, pp. 190-200, 2016.
- [35] X. Xu, "Preparation and Capacitive Properties of Transition Metal Oxide Based Electrode Materials," *Ph.D Dissertation*, Tianjin University, China, 2017.
- [36] P. Simon and Y. Gogotsi, "Charge storage mechanism in nanoporous carbons and its consequence for electrical double layer capacitors," *Philosophical Transactions of the Royal Society A: Mathematical, Physical and Engineering Sciences*, vol. 368, pp. 3457-3467, 2010.
- [37] J. Kang, J. Wen, S. H. Jayaram, A. Yu, and X. Wang, "Development of an equivalent circuit model for electrochemical double layer capacitors (EDLCs) with distinct electrolytes," *Electrochimica Acta*, vol. 115, pp. 587-598, 2014.
- [38] M. S. Uddin, H. T. Das, T. Maiyalagan, and P. Elumalai, "Influence of designed electrode surfaces on double layer capacitance in aqueous electrolyte: Insights from standard models," *Applied Surface Science*, vol. 449, pp. 445-453, 2018.
- [39] L. L. Zhang and X. S. Zhao, "Carbon-based materials as supercapacitor electrodes," *Chemical Society Reviews*, vol. 38, pp. 2520-2531, 2009.
- [40] M. Endo, T. Takeda, Y. J. Kim, K. Koshiba, and K. Ishii, "High power electric double layer capacitor (EDLC's); from operating principle to pore size control in advanced activated carbons," *Carbon letters*, vol. 1, pp. 117-128, 2001.
- [41] M. A. Brown, G. V. Bossa, and S. May, "Emergence of a stern layer from the incorporation of hydration interactions into the Gouy–Chapman model of the electrical double layer," *Langmuir*, vol. 31, pp. 11477-11483, 2015.
- [42] G. H. Bolt, "Analysis of the validity of the Gouy-Chapman theory of the electric double layer," *Journal of Colloid Science*, vol. 10, pp. 206-218, 1955.

- [43] G. M. Torrie and J. P. Valleau, "Electrical double layers. 4. Limitations of the Gouy-Chapman theory," *The Journal of Physical Chemistry*, vol. 86, pp. 3251-3257, 1982.
- [44] F. C. Schoemaker, N. Grobbe, M. D. Schakel, S. A. L. De Ridder, E. C. Slob, and D. M. J. Smeulders, "Experimental validation of the electrokinetic theory and development of seismoelectric interferometry by cross-correlation," *International Journal of Geophysics*, 2012.
- [45] J. P. Valleau and G. M. Torrie, "The electrical double layer. 3. Modified Gouy-Chapman theory with unequal ion sizes," *The Journal of Chemical Physics*, vol. 76, pp. 4623-4630, 1982.
- [46] K. L. Yang, T. Y. Ying, S. Yiacoumi, C. Tsouris, and E. S. Vittoratos, "Electrosorption of ions from aqueous solutions by carbon aerogel: an electrical double-layer model," *Langmuir*, vol. 17, pp. 1961-1969, 2001.
- [47] J. Liu, J. Wang, C. Xu, H. Jiang, C. Li, L. Zhang, J. Lin, and Z. X. Shen, "Advanced energy storage devices: basic principles, analytical methods, and rational materials design," *Advanced science*, vol. 5, pp. 1700322, 2018.
- [48] A. Muzaffar, M. B. Ahamed, K. Deshmukh, and J. Thirumalai, "A review on recent advances in hybrid supercapacitors: Design, fabrication and applications," *Renewable and Sustainable Energy Reviews*, vol. 101, pp. 123-145, 2019.
- [49] X. Chen, R. Paul, and L. Dai, "Carbon-based supercapacitors for efficient energy storage," *National Science Review*, vol. 4, pp. 453-489, 2017.
- [50] B. E. Conway, *Electrochemical supercapacitors: scientific fundamentals and technological applications*: Springer Science & Business Media, 2013.
- [51] V. Augustyn, P. Simon, and B. Dunn, "Pseudocapacitive oxide materials for high-rate electrochemical energy storage," *Energy & Environmental Science*, vol. 7, pp. 1597-1614, 2014.
- [52] M. Qiu, P. Sun, L. Shen, K. Wang, S. Song, X. Yu, S. Tan, C. Zhao, and W. Mai, "WO₃ nanoflowers with excellent pseudo-capacitive performance and the capacitance contribution analysis," *Journal of Materials Chemistry A*, vol. 4, pp. 7266-7273, 2016.
- [53] J. Liu, J. Jiang, C. Cheng, H. Li, J. Zhang, H. Gong, and H. J. Fan, "Co₃O₄ nanowire@MnO₂ ultrathin nanosheet core/shell arrays: a new class of high-performance pseudocapacitive materials," *Advanced Materials*, vol. 23, pp. 2076-2081, 2011.
- [54] X. Zhang, W. Shi, J. Zhu, D. J. Kharistal, W. Zhao, B. S. Lalia, H.H. Hng, and Q. Yan, "High-power and high-energy-density flexible pseudocapacitor electrodes made from porous CuO nanobelts and single-walled carbon nanotubes," *ACS nano*, vol. 5, pp. 2013-2019, 2011.
- [55] K. Zhou, W. Zhou, L. Yang, J. Lu, S. Cheng, W. Mai, Z. Tang, L. Li, and S. Chen, "Ultrahigh-Performance Pseudocapacitor Electrodes Based on Transition Metal Phosphide Nanosheets Array via Phosphorization: A General and Effective Approach," *Advanced Functional Materials*, vol. 25, pp. 7530-7538, 2015.
- [56] C. Wang, J. Xu, M. F. Yuen, J. Zhang, Y. Li, X. Chen, and W. Zhang, "Hierarchical composite electrodes of nickel oxide nanoflake 3D graphene for high-

- performance pseudocapacitors," *Advanced Functional Materials*, vol. 24, pp. 6372-6380, 2014.
- [57] P. Simon and Y. Gogotsi, "Materials for electrochemical capacitor," *Nature Materials*, vol. 7, pp. 845-854, 2008.
- [58] T. Liu, W. G. Pell, and B. E. Conway, "Self-discharge and potential recovery phenomena at thermally and electrochemically prepared RuO₂ supercapacitor electrodes," *Electrochimica Acta*, vol. 42, pp. 3541-3552, 1997.
- [59] Q. X. Jia, S. G. Song, X. D. Wu, J. H. Cho, S. R. Foltyn, A. T. Findikoglu, and J. L. Smith, "Epitaxial growth of highly conductive RuO₂ thin films on (100) Si," *Applied physics letters*, vol. 68, pp. 1069-1071, 1996.
- [60] S. Faraji and F. N. Ani, "Microwave-assisted synthesis of metal oxide/hydroxide composite electrodes for high power supercapacitors—a review," *Journal of Power Sources*, vol. 263, pp. 338-360, 2014.
- [61] J. Cao, X. Li, Y. Wang, F. C. Walsh, J. H. Ouyang, D. Jia, and Y. Zhou, "Materials and fabrication of electrode scaffolds for deposition of MnO₂ and their true performance in supercapacitors," *Journal of Power Sources*, vol. 293, pp. 657-674, 2015.
- [62] Q. Lu, J. G. Chen, and J. Q. Xiao, "Nanostructured electrodes for high-performance pseudocapacitors," *Angewandte Chemie International Edition*, vol. 52, pp. 1882-1889, 2013.
- [63] B. E. Conway, "Transition from "supercapacitor" to "battery" behavior in electrochemical energy storage," *Journal of the Electrochemical Society*, vol. 138, pp. 1539, 1991.
- [64] Y. Wang, Y. Song, and Y. Xia, "Electrochemical capacitors: mechanism, materials, systems, characterization and applications," *Chemical Society Reviews*, vol. 45, pp. 5925-5950, 2016.
- [65] M. Okubo, E. Hosono, J. Kim, M. Enomoto, N. Kojima, T. Kudo, H. Zhou, and I. Honma, "Nanosize effect on high-rate Li-ion intercalation in LiCoO₂ electrode," *Journal of the American chemical society*, vol. 129, pp. 7444-7452, 2007.
- [66] H. B. Li, M. H. Yu, F. X. Wang, P. Liu, Y. Liang, J. Xiao, C. X. Wang, Y. X. Tong, and G. W. Yang, "Amorphous nickel hydroxide nanospheres with ultrahigh capacitance and energy density as electrochemical pseudocapacitor materials," *Nature communications*, vol. 4, pp. 1-7, 2013.
- [67] M. Salanne, B. Rotenberg, K. Naoi, K. Kaneko, P. L. Taberna, C. P. Grey, B. Dunn, and P. Simon, "Efficient storage mechanisms for building better supercapacitors," *Nature Energy*, vol. 1, pp. 1-10, 2016.
- [68] J. R. Miller and P. Simon, "Electrochemical capacitors for energy management," *Science*, vol. 321, pp. 651-652, 2008.
- [69] A. Borenstein, O. Hanna, R. Attias, S. Luski, T. Brousse, and D. Aurbach, "Carbon-based composite materials for supercapacitor electrodes: a review," *Journal of Materials Chemistry A*, vol. 5, pp. 12653-12672, 2017.
- [70] Y. Huang, L. Peng, Y. Liu, G. Zhao, J. Y. Chen, and G. Yu, "Biobased nano porous active carbon fibers for high-performance supercapacitors," *ACS applied materials & interfaces*, vol. 8, pp. 15205-15215, 2016.

- [71] P. Simon and A. F. Burke, "Nanostructured carbons: double-layer capacitance and more," *The electrochemical society interface*, vol. 17, pp. 38, 2008.
- [72] O. Barbieri, M. Hahn, A. Herzog, and R. Kötz, "Capacitance limits of high surface area activated carbons for double layer capacitors," *Carbon*, vol. 43, pp. 1303-1310, 2005.
- [73] M. C. Liu, L. B. Kong, P. Zhang, Y. C. Luo, and L. Kang, "Porous wood carbon monolith for high-performance supercapacitors," *Electrochimica Acta*, vol. 60, pp. 443-448, 2012.
- [74] P. Lu, L. Müller, M. Hoffmann, and X. Chen, "Taper silicon nano-scaffold regulated compact integration of 1D nanocarbons for improved on-chip supercapacitor," *Nano Energy*, vol. 41, pp. 618-625, 2017.
- [75] D. N. Futaba, K. Hata, T. Yamada, T. Hiraoka, Y. Hayamizu, Y. Kakudate, O. Tanaike, H. Hatori, M. Yumura, and S. Iijima, "Shape-engineerable and highly densely packed single-walled carbon nanotubes and their application as supercapacitor electrodes," *Nature materials*, vol. 5, pp. 987-994, 2006.
- [76] H. Pan, J. Li, and Y. Feng, "Carbon nanotubes for supercapacitor," *Nanoscale research letters*, vol. 5, pp. 654-668, 2010.
- [77] E. Frackowiak, S. Delpeux, K. Jurewicz, K. Szostak, D. Cazorla-Amoros, and F. Beguin, "Enhanced capacitance of carbon nanotubes through chemical activation," *Chemical Physics Letters*, vol. 361, pp. 35-41, 2002.
- [78] Z. S. Wu, G. Zhou, L. C. Yin, W. Ren, F. Li, and H. M. Cheng, "Graphene/metal oxide composite electrode materials for energy storage," *Nano Energy*, vol. 1, pp. 107-131, 2012.
- [79] Y. Wang, Z. Shi, Y. Huang, Y. Ma, C. Wang, M. Chen, and Y. Chen, "Supercapacitor devices based on graphene materials," *The Journal of Physical Chemistry C*, vol. 113, pp. 13103-13107, 2009.
- [80] L. L. Zhang, R. Zhou, and X. S. Zhao, "Graphene-based materials as supercapacitor electrodes," *Journal of Materials Chemistry*, vol. 20, pp. 5983-5992, 2010.
- [81] J. Xia, F. Chen, J. Li, and N. Tao, "Measurement of the quantum capacitance of graphene," *Nature nanotechnology*, vol. 4, pp. 505, 2009.
- [82] S. R. C. Vivekchand, C. S. Rout, K. S. Subrahmanyam, A. Govindaraj, and C. N. R. Rao, "Graphene-based electrochemical supercapacitors," *Journal of Chemical Sciences*, vol. 120, pp. 9-13, 2008.
- [83] Y. Wang, Z. Shi, Y. Huang, Y. Ma, C. Wang, M. Chen, and Y. Chen, "Supercapacitor devices based on graphene materials," *The Journal of Physical Chemistry C*, vol. 113, pp. 13103-13107, 2009.
- [84] Y. Chen, X. Zhang, D. Zhang, P. Yu, and Y. Ma, "High performance supercapacitors based on reduced graphene oxide in aqueous and ionic liquid electrolytes," *Carbon*, vol. 49, pp. 573-580, 2011.
- [85] J. Liu, J. Wang, C. Xu, H. Jiang, C. Li, L. Zhang, J. Lin, and Z. X. Shen, "Advanced energy storage devices: basic principles, analytical methods, and rational materials design," *Advanced science*, vol. 5, pp. 1700322, 2018.
- [86] K. Naoi and P. Simon, "New materials and new configurations for advanced electrochemical capacitors," *Journal of The Electrochemical Society*, vol. 17, pp. 34-37, 2008.

- [87] C. C. Hu, W. C. Chen, and K. H. Chang, "How to achieve maximum utilization of hydrous ruthenium oxide for supercapacitors," *Journal of the Electrochemical Society*, vol. 151, pp. A281-A290, 2004.
- [88] H. Y. Lee and J. B. Goodenough, "Supercapacitor behavior with KCl electrolyte," *Journal of Solid State Chemistry*, vol. 144, pp. 220-223, 1999.
- [89] W. Chen, R. B. Rakhi, L. Hu, X. Xie, Y. Cui, and H. N. Alshareef, "High-performance nanostructured supercapacitors on a sponge," *Nano letters*, vol. 11, pp. 5165-5172, 2011.
- [90] Y. Wang, T. Zhou, K. Jiang, P. Da, Z. Peng, J. Tang, B. Kong, W. Cai, Z. Yang, and G. Zheng, "Reduced mesoporous Co_3O_4 nanowires as efficient water oxidation electrocatalysts and supercapacitor electrodes," *Advanced Energy Materials*, vol. 4, pp. 1400696, 2014.
- [91] G. Cheng, T. Kou, J. Zhang, C. Si, H. Gao, and Z. Zhang, " $\text{O}_2^{2-}/\text{O}^-$ -functionalized oxygen-deficient Co_3O_4 nanorods as high performance supercapacitor electrodes and electrocatalysts towards water splitting," *Nano Energy*, vol. 38, pp. 155-166, 2017.
- [92] X. Fan, Y. Sun, P. Ohlckers, and X. Chen, "Porous Thin-Wall Hollow Co_3O_4 Spheres for Supercapacitors with High Rate Capability," *Applied Sciences*, vol. 9, pp. 4672, 2019.
- [93] M. Yao, Z. Hu, Z. Xu, and Y. Liu, "Template synthesis of 1D hierarchical hollow Co_3O_4 nanotubes as high performance supercapacitor materials," *Journal of Alloys and Compounds*, vol. 644, pp. 721-728, 2015.
- [94] X. Zhou, X. Shen, Z. Xia, Z. Zhang, J. Li, Y. Ma, and Y. Qu, "Hollow fluffy Co_3O_4 cages as efficient electroactive materials for supercapacitors and oxygen evolution reaction," *ACS applied materials & interfaces*, vol. 7, pp. 20322-20331, 2015.
- [95] X. Fan, P. Ohlckers, and X. Chen, "Tunable Synthesis of Hollow Co_3O_4 Nanoboxes and Their Application in Supercapacitors," *Applied Sciences*, vol. 10, pp. 1208, 2020.
- [96] Y. Wang, Y. Lei, J. Li, L. Gu, H. Yuan, and D. Xiao, "Synthesis of 3D-nanonet hollow structured Co_3O_4 for high capacity supercapacitor," *ACS applied materials & interfaces*, vol. 6, pp. 6739-6747, 2014.
- [97] X. H. Xia, J. P. Tu, Y. J. Mai, X. L. Wang, C. D. Gu, and X. B. Zhao, "Self-supported hydrothermal synthesized hollow Co_3O_4 nanowire arrays with high supercapacitor capacitance," *Journal of Materials Chemistry*, vol. 21, pp. 9319-9325, 2011.
- [98] C. C. Hu, J. C. Chen, and K. H. Chang, "Cathodic deposition of $\text{Ni}(\text{OH})_2$ and $\text{Co}(\text{OH})_2$ for asymmetric supercapacitors: importance of the electrochemical reversibility of redox couples," *Journal of Power Sources*, vol. 221, pp. 128-133, 2013.
- [99] X. Xiong, D. Ding, D. Chen, G. Waller, Y. Bu, Z. Wang, and M. Liu, "Three-dimensional ultrathin $\text{Ni}(\text{OH})_2$ nanosheets grown on nickel foam for high-performance supercapacitors," *Nano Energy*, vol. 11, pp. 154-161, 2015.
- [100] W. J. Zhou, M. W. Xu, D. D. Zhao, C. L. Xu, and H. L. Li, "Electrodeposition and characterization of ordered mesoporous cobalt hydroxide films on different

- substrates for supercapacitors," *Microporous and Mesoporous Materials*, vol. 117, pp. 55-60, 2009.
- [101] X. Fan, P. Ohlckers, and X. Chen, "One-Step and Morphology-Controlled Synthesis of Ni-Co Binary Hydroxide on Nickel Foam for High-Performance Supercapacitors," *Applied Sciences*, vol. 10, pp. 3814, 2020.
- [102] J. Zhang, J. P. Cheng, M. Li, L. Liu, F. Liu, and X. B. Zhang, "Flower-like nickel-cobalt binary hydroxides with high specific capacitance: tuning the composition and asymmetric capacitor application," *Journal of Electroanalytical Chemistry*, vol. 743, pp. 38-45, 2015.
- [103] G. Xiong, P. He, D. Wang, Q. Zhang, T. Chen, and T. S. Fisher, "Hierarchical Ni-Co Hydroxide Petals on Mechanically Robust Graphene Petal Foam for High-Energy Asymmetric Supercapacitors," *Advanced Functional Materials*, vol. 26, pp. 5460-5470, 2016.
- [104] X. Liu, R. Ma, Y. Bando, and T. Sasaki, "A general strategy to layered transition-metal hydroxide nanocones: tuning the composition for high electrochemical performance," *Advanced Materials*, vol. 24, pp. 2148-2153, 2012.
- [105] T. Nguyen, M. Boudard, M. J. Carmezim, and M. F. Montemor, "Layered Ni(OH)₂-Co(OH)₂ films prepared by electrodeposition as charge storage electrodes for hybrid supercapacitors," *Scientific reports*, vol. 7, pp. 1-10, 2017.
- [106] C. Wang, X. Zhang, Z. Xu, X. Sun, and Y. Ma, "Ethylene glycol intercalated cobalt/nickel layered double hydroxide nanosheet assemblies with ultrahigh specific capacitance: structural design and green synthesis for advanced electrochemical storage," *ACS applied materials & interfaces*, vol. 7, pp. 19601-19610, 2015.
- [107] T. Nguyen, M. Boudard, M. J. Carmezim, and M. F. Montemor, "Ni_xCo_{1-x}(OH)₂ nanosheets on carbon nanofoam paper as high areal capacity electrodes for hybrid supercapacitors," *Energy*, vol. 126, pp. 208-216, 2017.
- [108] R. R. Salunkhe, K. Jang, S. W. Lee, and H. Ahn, "Aligned nickel-cobalt hydroxide nanorod arrays for electrochemical pseudocapacitor applications," *RSC Advances*, vol. 2, pp. 3190-3193, 2012.
- [109] M. Li, K. Y. Ma, J. P. Cheng, D. Lv, and X. B. Zhang, "Nickel-cobalt hydroxide nanoflakes conformal coating on carbon nanotubes as a supercapacitive material with high-rate capability," *Journal of Power Sources*, vol. 286, pp. 438-444, 2015.
- [110] Y. Tao, L. Ruiyi, L. Zaijun, L. Junkang, W. Guangli, and G. Zhiquo, "A free template strategy for the fabrication of nickel/cobalt double hydroxide microspheres with tunable nanostructure and morphology for high performance supercapacitors," *RSC Advances*, vol. 3, pp. 19416-19422, 2013.
- [111] Y. Tao, L. Ruiyi, Y. Tingting, and L. Zaijun, "Nickel/cobalt layered double hydroxide hollow microspheres with hydrangea-like morphology for high-performance supercapacitors," *Electrochimica Acta*, vol. 152, pp. 530-537, 2015.
- [112] H. Chen, L. Hu, M. Chen, Y. Yan, and L. Wu, "Nickel-cobalt layered double hydroxide nanosheets for high-performance supercapacitor electrode materials," *Advanced Functional Materials*, vol. 24, pp. 934-942, 2014.

- [113] Y. Tao, L. Zaijun, L. Ruiyi, N. Qi, K. Hui, N. Yulian, and L. Junkang, "Nickel–cobalt double hydroxides microspheres with hollow interior and hedgehog-like exterior structures for supercapacitors," *Journal of Materials Chemistry*, vol. 22, pp. 23587-23592, 2012.
- [114] Q. Ren, Z. Feng, S. Mo, C. Huang, S. Li, W. Zhang, L. Chen, M. Fu, J. Wu, and D. Ye, "1D-Co₃O₄, 2D-Co₃O₄, 3D-Co₃O₄ for catalytic oxidation of toluene," *Catalysis Today*, vol. 332, pp. 160-167, 2019.
- [115] G. Liu, "THE PREPARATION AND CAPACITANCE PERFORMANCE STUDY OF THREE-DIMENSIONAL COBALT-BASED NANOMATERIALS," *Ph.D Dissertation*, Harbin Institute of Technology, China, 2018.
- [116] Z. Yu, L. Tetard, L. Zhai, and J. Thomas, "Supercapacitor electrode materials: nanostructures from 0 to 3 dimensions," *Energy & Environmental Science*, vol. 8, pp. 702-730, 2015.
- [117] B. Hsia, "Materials Synthesis and Characterization for Micro-supercapacitor Applications," *Ph.D Dissertation*, University of California, Berkeley, USA, 2013.
- [118] P. Lu, E. Halvorsen, P. Ohlckers, L. Müller, S. Leopold, M. Hoffmann, K. Grigoras, J. Ahopelto, M. Prunnila, and X. Chen, "Ternary composite Si/TiN/MnO₂ taper nanorod array for on-chip supercapacitor," *Electrochimica Acta*, vol. 248, pp. 397–408, 2017
- [119] S. R. Ede, A. Ramadoss, U. Nithiyantham, S. Anantharaj, and S. Kundu, "Bio-molecule assisted aggregation of ZnWO₄ nanoparticles (NPs) into chain-like assemblies: Material for high performance supercapacitor and as catalyst for benzyl alcohol oxidation," *Inorganic chemistry*, vol. 54, pp. 3851-3863, 2015.
- [120] G. Li, M. Chen, Y. Ouyang, D. Yao, L. Lu, L. Wang, X. Xia, W. Lei, S. Chen, D. Mandler, and Q. Hao, "Manganese doped Co₃O₄ mesoporous nanoneedle array for long cycle-stable supercapacitors," *Applied Surface Science*, vol. 469, pp. 941-950, 2019.
- [121] Y. Liu, N. Fu, G. Zhang, M. Xu, W. Lu, L. Zhou, and H. Huang, "Design of Hierarchical Ni-Co@Ni-Co Layered Double Hydroxide Core–Shell Structured Nanotube Array for High-Performance Flexible All-Solid-State Battery-Type Supercapacitors," *Advanced Functional Materials*, vol. 27, pp. 1605307, 2017.
- [122] Y. Tang, Y. Liu, S. Yu, W. Guo, S. Mu, H. Wang, Y. Zhao, L. Hou, Y. Fan, and F. Gao, "Template-free hydrothermal synthesis of nickel cobalt hydroxide nanoflowers with high performance for asymmetric supercapacitor," *Electrochimica Acta*, vol. 161, pp. 279-289, 2015.
- [123] W. Y. Li, L. N. Xu, and J. Chen, "Co₃O₄ nanomaterials in lithium-ion batteries and gas sensors," *Advanced Functional Materials*, vol. 15, pp. 851-857, 2005.
- [124] H. B. Wu, H. Pang, and X. W. D. Lou, "Facile synthesis of mesoporous Ni_{0.3}Co_{2.7}O₄ hierarchical structures for high-performance supercapacitors," *Energy & Environmental Science*, vol. 6, pp. 3619-3626, 2013.
- [125] Z. Zhu, C. Han, T. T. Li, Y. Hu, J. Qian, and S. Huang, "MOF-templated syntheses of porous Co₃O₄ hollow spheres and micro-flowers for enhanced performance in supercapacitors," *CrystEngComm*, vol. 20, pp. 3812-3816, 2018.
- [126] F. Zhang, C. Yuan, J. Zhu, J. Wang, X. Zhang, and X. W. Lou, "Flexible films derived from electrospun carbon nanofibers incorporated with Co₃O₄ hollow

- nanoparticles as self-supported electrodes for electrochemical capacitors," *Advanced Functional Materials*, vol. 23, pp. 3909-3915, 2013.
- [127] H. Du, L. Jiao, Q. Wang, J. Yang, L. Guo, Y. Si, Y. Wang, and H. Yuan, "Facile carbonaceous microsphere templated synthesis of Co_3O_4 hollow spheres and their electrochemical performance in supercapacitors," *Nano Research*, vol. 6, pp. 87-98, 2013.
- [128] Y. Z. Zhang, Y. Wang, Y. L. Xie, T. Cheng, W. Y. Lai, H. Pang, and W. Huang, "Porous hollow Co_3O_4 with rhombic dodecahedral structures for high-performance supercapacitors," *Nanoscale*, vol. 6, pp. 14354-14359, 2014.
- [129] W. Du, R. Liu, Y. Jiang, Q. Lu, Y. Fan, and F. Gao, "Facile synthesis of hollow Co_3O_4 boxes for high capacity supercapacitor," *Journal of power sources*, vol. 227, pp. 101-105, 2013.
- [130] D. Guo, X. Song, F. Li, L. Tan, H. Ma, L. Zhang, and Y. Zhao, "Oriented synthesis of Co_3O_4 core-shell microspheres for high-performance asymmetric supercapacitor," *Colloids and Surfaces A: Physicochemical and Engineering Aspects*, vol. 546, pp. 1-8, 2018.
- [131] A. Xiao, S. Zhou, C. Zuo, Y. Zhuan, and X. Ding, "Controllable synthesis of mesoporous Co_3O_4 nanoflake array and its application for supercapacitor," *Materials Research Bulletin*, vol. 60, pp. 674-678, 2014.
- [132] H. Chen, S. Lu, F. Gong, H. Liu, and F. Li, "Stepwise splitting growth and pseudocapacitive properties of hierarchical three-dimensional Co_3O_4 nanobooks," *Nanomaterials*, vol. 7, pp. 81, 2017.
- [133] Y. Zheng, Z. Li, J. Xu, T. Wang, X. Liu, X. Duan, Y. Ma, Y. Zhou, and C. Pei, "Multi-channeled hierarchical porous carbon incorporated Co_3O_4 nanopillar arrays as 3D binder-free electrode for high performance supercapacitors," *Nano Energy*, vol. 20, pp. 94-107, 2016.
- [134] Y. Tan, Y. Liu, L. Kong, L. Kang, and F. Ran, "Supercapacitor electrode of nano- Co_3O_4 decorated with gold nanoparticles via in-situ reduction method," *Journal of Power Sources*, vol. 363, pp. 1-8, 2017.
- [135] Q. Hu, Z. Gu, X. Zheng, and X. Zhang, "Three-dimensional Co_3O_4 @NiO hierarchical nanowire arrays for solid-state symmetric supercapacitor with enhanced electrochemical performances," *Chemical Engineering Journal*, vol. 304, pp. 223-231, 2016.
- [136] M. Pang, G. Long, S. Jiang, Y. Ji, W. Han, B. Wang, X. Liu, Y. Xi, D. Wang, and F. Xu, "Ethanol-assisted solvothermal synthesis of porous nanostructured cobalt oxides ($\text{CoO}/\text{Co}_3\text{O}_4$) for high-performance supercapacitors," *Chemical Engineering Journal*, vol. 280, pp. 377-384, 2015.
- [137] Y. M. Jo, T. H. Kim, C. S. Lee, K. Lim, C. W. Na, F. Abdel-Hady, A. A. Wazzan, and J. H. Lee, "Metal-organic framework-derived hollow hierarchical Co_3O_4 nanocages with tunable size and morphology: ultrasensitive and highly selective detection of methylbenzenes," *ACS applied materials & interfaces*, vol. 10, pp. 8860-8868, 2018.
- [138] S. Tanaka, K. Kida, M. Okita, Y. Ito, and Y. Miyake, "Size-controlled synthesis of zeolitic imidazolate framework-8 (ZIF-8) crystals in an aqueous system at room temperature," *Chemistry letters*, vol. 41, pp. 1337-1339, 2012.

- [139] X. Wang, N. Zhang, X. Chen, J. Liu, F. Lu, L. Chen, and G. Shao, "Facile precursor conversion synthesis of hollow coral-shaped Co_3O_4 nanostructures for high-performance supercapacitors," *Colloids and Surfaces A: Physicochemical and Engineering Aspects*, vol. 570, pp. 63-72, 2019.
- [140] Z. Liu, W. Zhou, S. Wang, W. Du, H. Zhang, C. Ding, Y. Du, and L. Zhu, "Facile synthesis of homogeneous core-shell Co_3O_4 mesoporous nanospheres as high performance electrode materials for supercapacitor," *Journal of Alloys and Compounds*, vol. 774, pp. 137-144, 2019.
- [141] Z. Xiao, L. Fan, B. Xu, S. Zhang, W. Kang, Z. Kang, H. Lin, X. Liu, S. Zhang, and D. Sun, "Green fabrication of ultrathin Co_3O_4 nanosheets from metal-organic framework for robust high-rate supercapacitors," *ACS applied materials & interfaces*, vol. 9, pp. 41827-41836, 2017.
- [142] W. Gou, X. Zhou, J. Li, and Y. Ma, "Nanoporous Co_3O_4 plates as highly electroactive materials for electrochemical energy storage," *Materials Letters*, vol. 180, pp. 207-211, 2016.
- [143] M. Kumar, A. Subramania, and K. Balakrishnan, "Preparation of electrospun Co_3O_4 nanofibers as electrode material for high performance asymmetric supercapacitors," *Electrochimica Acta*, vol. 149, pp. 152-158, 2014.
- [144] H. Chen, J. Wang, F. Liao, X. Han, Y. Zhang, C. Xu, and L. Gao, "Uniform and porous Mn-doped Co_3O_4 microspheres: Solvothermal synthesis and their superior supercapacitor performances," *Ceramics International*, vol. 45, pp. 11876-11882, 2019.
- [145] J. Wang, X. Zhang, Q. Wei, H. Lv, Y. Tian, Z. Tong, X. Liu, J. Hao, H. Qu, J. Zhao, Y. Li, and L. Mai, "3D self-supported nanopine forest-like $\text{Co}_3\text{O}_4@ \text{CoMoO}_4$ core-shell architectures for high-energy solid state supercapacitors," *Nano Energy*, vol. 19, pp. 222-233, 2016.
- [146] X. Bai, Q. Liu, J. Liu, H. Zhang, Z. Li, X. Jing, P. Liu, J. Wang, and R. Li, "Hierarchical $\text{Co}_3\text{O}_4@ \text{Ni}(\text{OH})_2$ core-shell nanosheet arrays for isolated all-solid state supercapacitor electrodes with superior electrochemical performance," *Chemical Engineering Journal*, vol. 315, pp. 35-45, 2017.
- [147] L. Bao, T. Li, S. Chen, C. Peng, L. Li, Q. Xu, Y. Chen, E. Ou, and W. Xu, "3D Graphene Frameworks/ Co_3O_4 Composites Electrode for High-Performance Supercapacitor and Enzymeless Glucose Detection," *Small*, vol. 13, pp. 1602077, 2017.
- [148] H. Wang, Q. Ren, D. J. Brett, G. He, R. Wang, J. Key, and S. Ji, "Double-shelled tremella-like $\text{NiO}@ \text{Co}_3\text{O}_4@ \text{MnO}_2$ as a high-performance cathode material for alkaline supercapacitors," *Journal of Power Sources*, vol. 343, pp. 76-82, 2017.
- [149] X. Sun, G. Wang, H. Sun, F. Lu, M. Yu, and J. Lian, "Morphology controlled high performance supercapacitor behaviour of the Ni-Co binary hydroxide system," *Journal of power sources*, vol. 238, pp. 150-156, 2013.
- [150] G. Wang, L. Zhang, J. Kim, and J. Zhang, "Nickel and cobalt oxide composite as a possible electrode material for electrochemical supercapacitors," *Journal of Power Sources*, vol. 217, pp. 554-561, 2012.
- [151] F. Liu, X. Chu, H. Zhang, B. Zhang, H. Su, L. Jin, Z. Wang, H. Huang, and W. Yang, "Synthesis of self-assembly 3D porous $\text{Ni}(\text{OH})_2$ with high capacitance for hybrid supercapacitors," *Electrochimica Acta*, vol. 269, pp. 102-110, 2018.

- [152] T. Xue, X. Wang, and J. M. Lee, "Dual-template synthesis of $\text{Co}(\text{OH})_2$ with mesoporous nanowire structure and its application in supercapacitor," *Journal of Power Sources*, vol. 201, pp. 382-386, 2012.
- [153] C. Jiang, B. Zhao, J. Cheng, J. Li, H. Zhang, Z. Tang, and J. Yang, "Hydrothermal synthesis of $\text{Ni}(\text{OH})_2$ nanoflakes on 3D graphene foam for high-performance supercapacitors," *Electrochimica Acta*, vol. 173, pp. 399-407, 2015.
- [154] T. Wang, S. Zhang, X. Yan, M. Lyu, L. Wang, J. Bell, and H. Wang, "2-Methylimidazole-derived Ni-Co layered double hydroxide nanosheets as high rate capability and high energy density storage material in hybrid supercapacitors," *ACS applied materials & interfaces*, vol. 9, pp. 15510-15524, 2017.
- [155] L. Xie, Z. Hu, C. Lv, G. Sun, J. Wang, Y. Li, H. He, J. Wang, and K. Li, " $\text{Co}_x\text{Ni}_{1-x}$ double hydroxide nanoparticles with ultrahigh specific capacitances as supercapacitor electrode materials," *Electrochimica acta*, vol. 78, pp. 205-211, 2012.
- [156] Z. A. Hu, Y. L. Xie, Y. X. Wang, H. Y. Wu, Y. Y. Yang, and Z. Y. Zhang, "Synthesis and electrochemical characterization of mesoporous $\text{Co}_x\text{Ni}_{1-x}$ layered double hydroxides as electrode materials for supercapacitors," *Electrochimica Acta*, vol. 54, pp. 2737-2741, 2009.
- [157] Q. Wang, X. Wang, B. Liu, G. Yu, X. Hou, D. Chen, and G. Shen, " NiCo_2O_4 nanowire arrays supported on Ni foam for high-performance flexible all-solid-state supercapacitors," *Journal of Materials Chemistry A*, vol. 1, pp. 2468-2473, 2013.
- [158] Y. Cheng, H. Zhang, C. V. Varanasi, and J. Liu, "Improving the performance of cobalt-nickel hydroxide-based self-supporting electrodes for supercapacitors using accumulative approaches," *Energy & Environmental Science*, vol. 6, pp. 3314-3321, 2013.
- [159] X. Bai, Q. Liu, H. Zhang, J. Liu, Z. Li, X. Jing, Y. Yuan, L. Liu, and J. Wang, "Nickel-cobalt layered double hydroxide nanowires on three dimensional graphene nickel foam for high performance asymmetric supercapacitors," *Electrochimica Acta*, vol. 215, pp. 492-499, 2016.
- [160] K. Le, Z. Wang, F. Wang, Q. Wang, Q. Shao, V. Murugadoss, S. Wu, W. Liu, J. Liu, Q. Gao, and Z. Guo, "Sandwich-like NiCo layered double hydroxide/reduced graphene oxide nanocomposite cathodes for high energy density asymmetric supercapacitors," *Dalton Transactions*, vol. 48, pp. 5193-5202, 2019.
- [161] X. Cai, X. Shen, L. Ma, Z. Ji, C. Xu, and A. Yuan, "Solvothermal synthesis of NiCo-layered double hydroxide nanosheets decorated on RGO sheets for high performance supercapacitor," *Chemical Engineering Journal*, vol. 268, pp. 251-259, 2015.
- [162] Y. Huang, Y. Gao, Q. Zhang, J. J. Cao, R. J. Huang, W. Ho, and S. C. Lee, "Hierarchical porous ZnWO_4 microspheres synthesized by ultrasonic spray pyrolysis: characterization, mechanistic and photocatalytic NO_x removal studies," *Applied Catalysis A: General*, vol. 515, pp. 170-178, 2016.
- [163] C. Yu and C. Y. Jimmy, "Sonochemical fabrication, characterization and photocatalytic properties of Ag/ZnWO_4 nanorod catalyst," *Materials Science and Engineering: B*, vol. 164, pp. 16-22, 2009.

- [164] O. Y. Khyzhun, V. L. Bekenev, V. V. Atuchin, E. N. Galashov, and V. N. Shlegel, "Electronic properties of ZnWO₄ based on ab initio FP-LAPW band-structure calculations and X-ray spectroscopy data," *Materials Chemistry and Physics*, vol. 140, pp. 588-595, 2013.

Article I

Fan, X., Sun, Y., Ohlckers, P., & Chen, X. (2019). Porous Thin-Wall Hollow Co_3O_4 Spheres for Supercapacitors with High Rate Capability. *Applied Sciences*, 9(21), 4672. DOI: 10.3390/app9214672

Article

Porous Thin-Wall Hollow Co_3O_4 Spheres for Supercapacitors with High Rate Capability

Xiao Fan ¹, Yongjiao Sun ², Per Ohlckers ^{1,*}  and Xuyuan Chen ^{1,*}

¹ Department of Microsystems, University of South-Eastern Norway, Campus Vestfold, Raveien 215, 3184 Borre, Norway; xiao.fan@usn.no

² Micro and Nano System Research Center, College of Information and Computer, Taiyuan University of Technology, Taiyuan 030024, China; yjsun88@126.com

* Correspondence: per.ohlckers@usn.no (P.O.); xuyuan.chen@usn.no (X.C.)

Received: 25 September 2019; Accepted: 30 October 2019; Published: 2 November 2019



Abstract: In this study, a zeolitic imidazolate framework-67 (ZIF-67) was prepared as a precursor using a facile hydrothermal method. After a calcination reaction in the air, the as-prepared precursor was converted to porous thin-wall hollow Co_3O_4 with its original frame structure almost preserved. The physical and chemical characterizations of the nanomaterial were analyzed systemically. The electrochemical tests indicate that the obtained Co_3O_4 possesses large specific capacitances of 988 and 925 F/g at 1 and 20 A/g accompanying an outstanding rate capability (a 93.6% capacitance retention) and retains 96.6% of the specific capacitance, even after 6000 continuous charge/discharge cycles. These excellent properties mark the Co_3O_4 a promising electrode material for high performance supercapacitors.

Keywords: Co_3O_4 ; hollow structure; rate capability; supercapacitors

1. Introduction

Rapid technological development and accelerated natural resource consumption have largely increased the demand for efficient, environmentally-friendly, cost-effective, and safe energy storage devices [1–4]. In the last decade, supercapacitors—the new devices between conventional physical capacitors and lithium-ion batteries—have been extensively recognized as one of the most promising candidates for energy storage devices due to their high power density, long cycling lifespan, and fast charge/discharge process [5–11]. In general, supercapacitors can be divided into two categories according to their energy storage mechanism: One is the electric double-layer capacitor (EDLCs), which is mainly made of carbonaceous materials [12–16]; the other is the faradic redox reaction pseudocapacitor (PSCs), which usually utilizes transition metal oxides/hydroxides as electrode materials [17–21]. In particular, pseudocapacitors deliver much higher specific capacitance in comparison with electric double-layer capacitors, and receive considerable interest today [22,23].

Among various transition metal compounds, Co_3O_4 occupies a crucial position due to its superior theoretical specific capacitance (3560 F/g), nontoxicity, and low cost [24–26]. Meanwhile, the hollow structure stands out because of its novel interior geometry and surface functionality; this can possibly provide a large surface area and extra active sites, thus dramatically boosting the electrochemical properties [27,28]. To date, a great deal of efforts have been devoted to synthesizing Co_3O_4 with hollow morphologies such as hollow spheres [28], hollow nanocubes [29], and hollow cages [30]. Despite the great progress that has been made, the specific capacitance is still significantly below the theoretical value, especially at high current densities. Therefore, it is still a challenge to fully take advantage of this powerful hollow nanoscaled Co_3O_4 to achieve a large specific capacitance and a good rate capability.

In this work, we successfully prepared porous thin-wall hollow Co_3O_4 spheres from a zeolitic imidazolate framework-67 (ZIF-67) precursor through a simple and fast reaction. This nanostructure offers a large accessible surface area with numerous pathways. As a consequence, it exhibits a large specific capacitance of 988 F/g at 1 A/g with satisfactory cycling stability (96.6% retention after 6000 cycles). In particular, the specific capacitance of 925 F/g at even 20 A/g (slight decay of less than 7%) is extremely competitive among Co_3O_4 -based electrode materials reported in literature. The pseudocapacitive performance manifests the great potential of the porous thin-wall hollow Co_3O_4 spheres as electrode materials for applications in supercapacitors.

2. Materials and Methods

2.1. Sample Preparation

All reagents were of analytical grade and were used as received without any further purification. First, 0.437 g of $\text{Co}(\text{NO}_3)_2 \cdot 6\text{H}_2\text{O}$ and 0.616 g of 2-methyl imidazole were briefly dissolved in respective 20 mL methanol solutions. Then, the latter solution was added dropwise into the prior one under vigorous stirring. After an ultrasonic bath for 20 min, the precipitates were collected by centrifugation and washed with methanol. Partial precipitates (0.02 g) were dispersed in a 15 mL methanol solution again. Subsequently, 0.175 g of $\text{Co}(\text{NO}_3)_2 \cdot 6\text{H}_2\text{O}$ was added into the separated solution. The resulting mixture was transferred to a Teflon-lined stainless-steel autoclave and heated at 120 °C for 1 h. The separated products were washed with methanol and dried at 60 °C. Finally, the porous thin-wall hollow Co_3O_4 spheres were obtained via heat treatment at 400 °C for 2 h.

2.2. Material Characterizations

The crystal structure of as-obtained Co_3O_4 was recorded by X-ray powder diffraction (XRD, EQUINOX 1000) with $\text{Cu-K}\alpha_1$ radiation ($\lambda = 1.5406 \text{ \AA}$). Scanning electron microscopy (SEM, Hitachi SU8230) with energy-dispersive X-ray (EDX) spectrum was performed for characterizations of morphology and element composition. X-ray photoelectron spectroscopy (XPS) was collected on an ESCALAB 250Xi.

2.3. Electrochemical Measurements

The Co_3O_4 , acetylene black, and polyvinylidene fluoride (PVDF) with a weight ratio of 80:15:5 were dispersed in *n*-methyl-2-pyrrolidone (NMP) solution and ground continuously for 10 min in a mortar to form a slurry. The working electrode was prepared by pressing the slurry on nickel foam (NF). The electrochemical measurements were carried out at room temperature in a typical three-electrode system (2M KOH as the electrolyte), in which a Pt net and Ag/AgCl were used as a counter electrode and a reference electrode, respectively. A cyclic voltammogram (CV) was conducted at various scan rates and galvanostatic charge/discharge (GCD) was tested at different current densities. The specific capacitance (C , F/g) based on CV is defined as:

$$C = \frac{\int i(V)dV}{2mv\Delta V}, \quad (1)$$

and the specific capacitance based on GCD is given by:

$$C = \frac{It}{m\Delta V}, \quad (2)$$

where $\int i(V)dV$ (V·A) is the integrated area of the CV curve, and m (g), v (V/s), ΔV (V), I (A/g), and t (s) are the mass of active material, scan rate, potential window, discharge current, and discharge time [31,32]. The electrochemical impedance spectrum (EIS) was determined over a frequency range

from 100 mHz to 100 kHz with an AC perturbation of 5 mV at open circuit potential. The cycling performance was evaluated through repetitive GCD tests.

3. Results and Discussion

The morphology of as-prepared Co_3O_4 was investigated by SEM. Figure 1 presents SEM images of the precursor (Figure 1a,b) and the calcined Co_3O_4 (Figure 1c,d). Surprisingly, the Co_3O_4 effectively inherited the morphology of the precursor (negligible size contraction and few broken pieces) and exhibits uniform spherical structures. Furthermore, the magnified image (Figure 1d) shows that the spheres tend to interconnect with one another and clearly confirms the hollow nature, as well as the thin shell thickness of the Co_3O_4 from the view of a broken piece. The diameter of the spheres lies between 500 and 600 nm. In addition, the shell is assembled from numerous nanoparticles, constructing a highly porous architecture. This structure results in more active sites on the surface and easier transportation of ions, leading to better electrochemical performance.

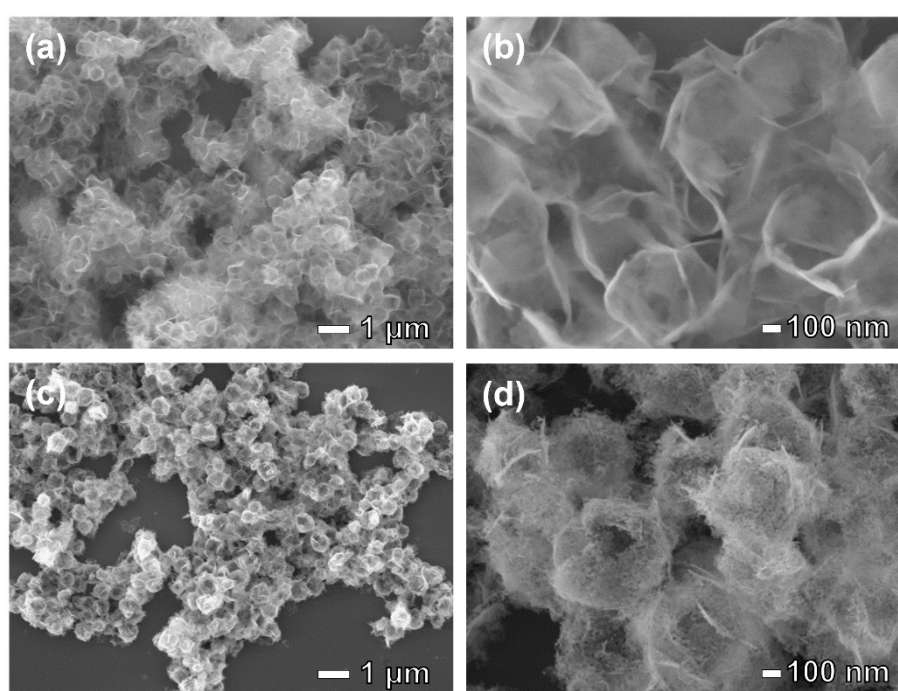


Figure 1. SEM images of (a) low- and (b) high-magnification of the precursor; (c) low- and (d) high-magnification of the calcined Co_3O_4 .

The XRD patterns seen in Figure 2a, where the eight identified diffraction peaks located at 19° , 31.3° , 36.9° , 38.6° , 44.9° , 55.8° , 59.5° , and 65.4° are indexed to the (111), (220), (311), (222), (400), (422), (511), and (440) planes respectively, are perfectly consistent with the cubic phase of Co_3O_4 (JCPDS card No. 65-3103) [33]. The element compositions were confirmed by EDX, as depicted in Figure 2b. The peaks correspond to the elements Co and O, respectively. No other impurity element was observed. Both XRD and EDX characterizations reveal the high purity of the product.

The XPS was used to analyze the surface component and valence state of the as-obtained Co_3O_4 . In the Co 2p core-level XPS spectrum seen in Figure 3a, the Co 2p was deconvoluted into two doublets. The peaks at 779.4 and 794.4 eV are related to Co^{3+} , and the peaks at 780.4 and 795.7 eV are assigned to Co^{2+} [34]. In the high-resolution XPS spectrum of O 1s seen in Figure 3b, the O 1s can be fit into three different peaks at binding energies of 529.9, 530.9, and 532 eV, which are referenced to the lattice oxygen, the OH^- species absorbed onto surface, and the multiplicity of physical and chemical absorbed water near surface, respectively [35]. This analysis of XPS further verifies the successful synthesis of the Co_3O_4 .

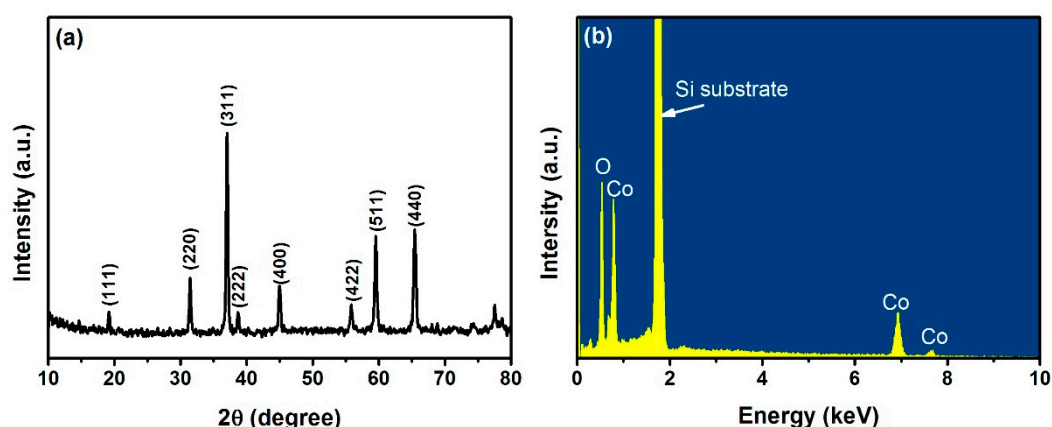


Figure 2. (a) XRD patterns and (b) energy-dispersive X-ray (EDX) spectrum of the obtained Co_3O_4 .

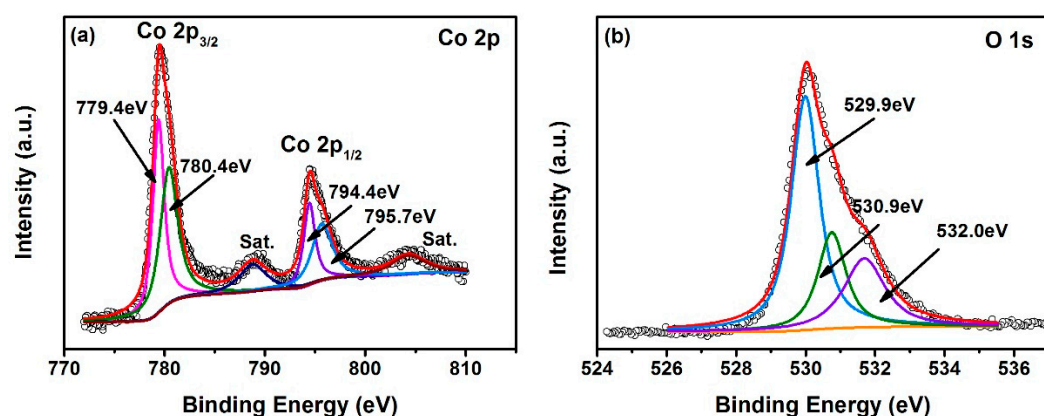
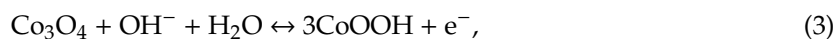
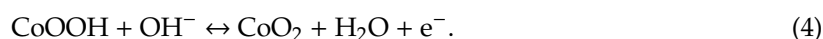


Figure 3. High-resolution X-ray photoelectron spectroscopy (XPS) scan of as-obtained Co_3O_4 : (a) Co 2p region; (b) O 1s region.

The electrochemical performance of as-formed Co_3O_4 as an electrode material for supercapacitors was evaluated systematically. Figure 4a shows CV curves of the Co_3O_4 at various scan rates within a potential window of 0–0.55 V. As expected, the CV curve shape is totally different from those of electric double-layer capacitors (which have an almost rectangular shape), which reveals that the capacitance characteristics of the Co_3O_4 are those of typical pseudocapacitive capacitance. Additionally, two distinct pairs of redox peaks are visible in the CV curves. The first redox couple is ascribed to the faradic redox reaction of $\text{Co}^{2+}/\text{Co}^{3+}$, expressed as Equation (3) [29,30,36]:



and the second redox couple corresponds to the conversion of $\text{Co}^{3+}/\text{Co}^{4+}$, expressed as Equation (4) [29,30,36]:



When the scan rate increases from 5 to 100 mV/s, the peak current increases enormously. Furthermore, the anodic and cathodic peaks shift to higher and to lower potentials, suggesting classical pseudocapacitive behavior. The CV curve of the Co_3O_4 at 100 mV/s retains a redox shape similar to the original shape at 5 mV/s. It implies that the Co_3O_4 possesses an excellent rate capability, which is further confirmed by the calculated specific capacitances.

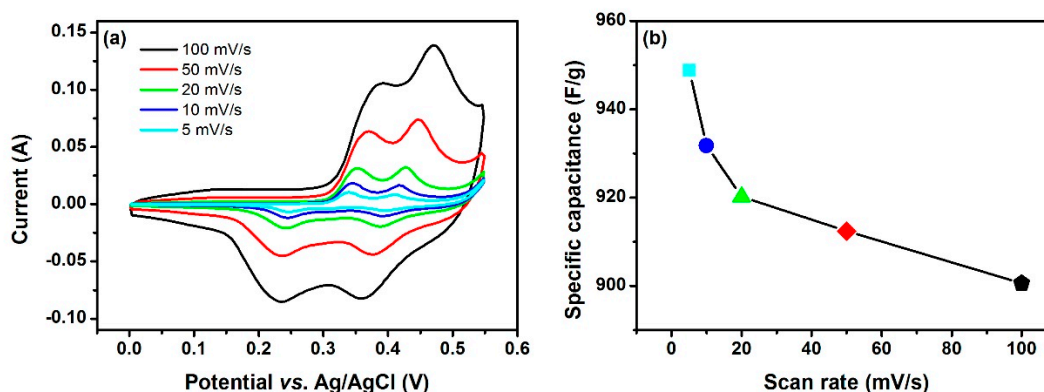


Figure 4. (a) Cyclic voltammogram (CV) curves and (b) specific capacitances of the Co_3O_4 electrode at various scan rates.

On the basis of Equation (1), the specific capacitances were determined to be 948.9, 931.8, 920.2, 912.4, and 900.6 F/g at scan rates of 5, 10, 20, 50, and 100 mV/s respectively, as shown in Figure 4b. The prominent specific capacitances most probably benefit from the porous hollow sphere nanostructure. The decrease in specific capacitances with an increasing scan rate can be understood in terms of the circuitous diffusion of OH^- ions into the Co_3O_4 . At a low scan rate, both the inner and outer surface of the material can be utilized for charge storage. At a high scan rate, the diffusion of OH^- ions is more likely happen on the outer surface and only a small fraction of OH^- ions can penetrate into the inner surface [37]. Nevertheless, the inevitable decrease of specific capacitances is not drastic, which demonstrates an excellent rate capability (maintaining almost 95% capacitance from 5 to 100 mV/s). This phenomenon illustrates that the Co_3O_4 is able to act as a “reservoir” of ions [38,39] to accommodate OH^- . The reservoir can guarantee the efficient proceeding of the faradic reactions at high scan rates (or high current densities) and in turn relieves the fading of the specific capacitances. Further evidence is provided by GCD measurement.

The discharge curves of the Co_3O_4 measured at different current densities in a voltage window of 0–0.55 V are presented in Figure 5a. In comparison with the discharge curves of electric double-layer capacitors (which are almost a straight line), two evident plateaus are well displayed. These coincide with the sequential redox reactions described by Equations (3) and (4), indicating the pseudocapacitive property of the Co_3O_4 . According to Equation (2), specific capacitances of 988, 960, 947.9, 939.4, and 925 F/g can be delivered at current densities of 1, 2, 5, 10, and 20 A/g respectively, as depicted by Figure 5b. Due to the relatively insufficient active material involved in redox reactions under higher current densities, the boosting of the current densities results in the fading of specific capacitances. At a low current density, the OH^- ions have adequate time to transfer at the interface between electrode and electrolyte than they do at a high current density [40]. It is worth noting that the rate performance of the Co_3O_4 is impressive (maintaining 925 F/g at 20 A/g, representing a 93.6% capacitance retention), which is significant for practical use of the material.

An EIS study is depicted in Figure 6. The first intersection point of the Nyquist plot with the real axis reflects the resistances (R_s), including the ionic resistance of the electrolyte, contact resistance at the interface of electrolyte and electrode, and intrinsic resistance of the material [39]. The Co_3O_4 modified electrode exhibits a very low R_s of 0.52 Ohms. In the high frequency region, the charge-transfer resistance (R_{ct}) and double-layer capacitance (C_{dl}) correspond to the semicircle arc. The inset of Figure 6 shows that the semicircle has a small diameter, expressing a low charge-transfer resistance and a low interfacial resistance between the current collector and electroactive material [22,41]. In the low frequency range, the slope of the plot corresponds to the diffusive resistance of OH^- ions (Warburg impedance, W) within the Co_3O_4 . The plot presents an evident straight line with a slope greater than 45° , which indicates a valid electrolyte ion diffusion [30,34]. The equivalent circuit fitting the

impedance spectrum, which involves R_s , R_{ct} , C_{dl} , W , and pseudocapacitance (C_{ps}), is shown in the inset of Figure 6.

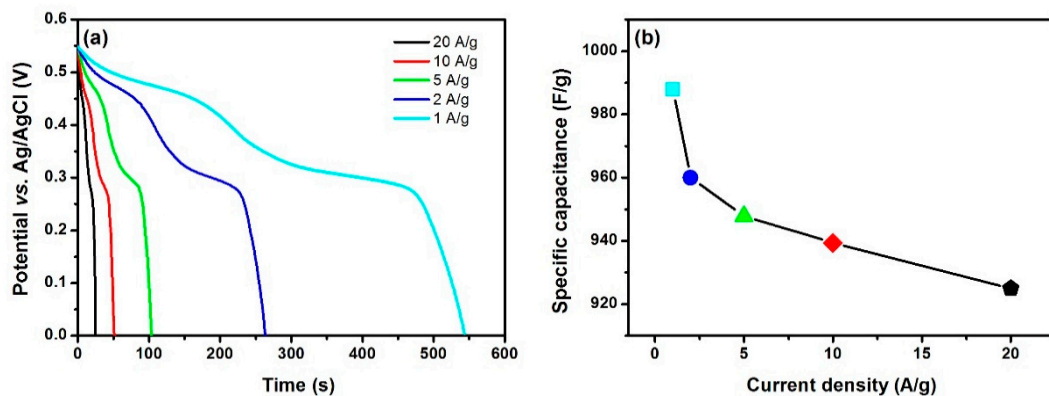


Figure 5. (a) Discharge curves and (b) specific capacitances of the Co_3O_4 electrode at different current densities.

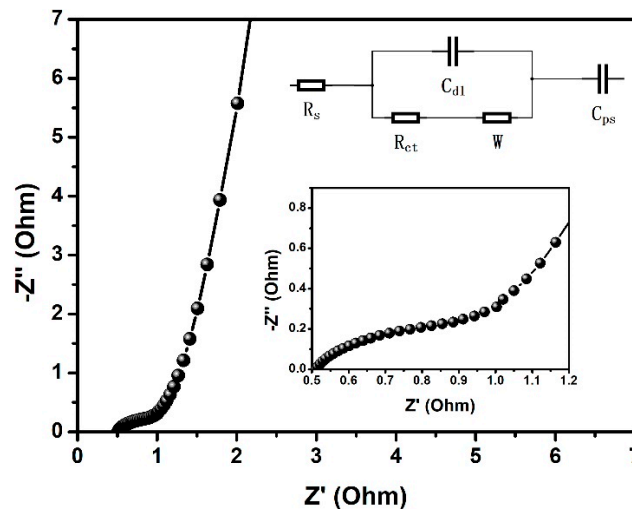


Figure 6. Electrochemical impedance spectrum (EIS) plot of the Co_3O_4 electrode over a frequency range from 100 mHz to 100 kHz. The insets show the equivalent circuit and an enlarged view of the high frequency region.

Long-term cycling stability is an important parameter required for practical application. Hence, the GCD tests were repeated for 6000 cycles at a current density of 20 A/g. As shown in Figure 7, 96.6% of the specific capacitance value is still retained. In addition, the coulombic efficiency is deduced from Equation (5) [37,39]:

$$\eta = \frac{t_d}{t_c}, \quad (5)$$

where t_d (s) and t_c (s) are, respectively, the discharge and charge times; a high efficiency exceeding 95% is achieved. This reveals that long-lasting cycling assessment does no obvious damage to the nanostructure and a feasible redox process is generated from the obtained material and verifies the remarkable electrochemical stability.

A comparison between our work and Co_3O_4 -based electrode materials in current reports was made, as summarized in Table 1. Unfortunately, the high capacitive performances obtained through tremendous efforts usually accompany poor rate capability, which severely limits their wide application in high-power energy storage devices. The Co_3O_4 in this paper can meet the need of not only high specific capacitance but also excellent rate capability. In addition, the performance of the Co_3O_4 is

even better than some composites of cobalt oxides [34,42,43]. The superior electrochemical behaviors can first be explained by the stable morphology. Secondly, the large surface and inner space favors an efficient contact between active material and electrolyte, ensuring a high utilization rate of active material. Thirdly, the interconnected nanoparticles with an increased surface-to-bulk ratio offer more sites for ions to enter and, more importantly, allow facile ion diffusion at a high current density [44]. Finally, the hollow spheres are interconnected with one another, contributing to an even longer ionic diffusion channel [37].

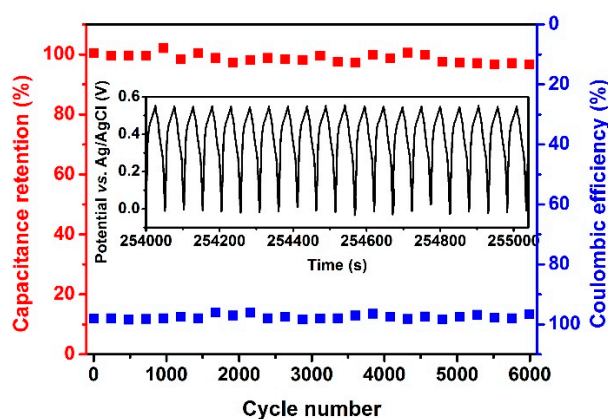


Figure 7. Cycling performance and coulombic efficiency of the Co_3O_4 electrode.

Table 1. Brief capacitance, rate, and cycling performance list of Co_3O_4 -based electrode materials.

Material	Specific Capacitance	Rate Capability	Stability-Cycles	Ref.
hollow Co_3O_4 spheres	474.8 F/g at 1 A/g	79% at 10 A/g	99%-1000	[37]
hollow Co_3O_4 spheres	394.4 F/g at 2 A/g	81% at 20 A/g	92%-500	[45]
hollow Co_3O_4 spheres	342.1 F/g at 0.5 A/g	69% at 10 A/g	90%-2000	[46]
hollow Co_3O_4 nanotubes	1006 F/g at 1 A/g	51% at 10 A/g	91%-1000	[29]
hollow Co_3O_4 cages	948.9 F/g at 1 A/g	56.6% at 40 A/g	–	[30]
hollow Co_3O_4 nanotubes	404.9 F/g at 0.5 A/g	87.8% at 20 A/g	95%-2000	[38]
hollow Co_3O_4 3D-nanonet	739 F/g at 1 A/g	72% at 15 A/g	90.2%-1000	[39]
hollow Co_3O_4 flowers	210 F/g at 0.5 A/g	86% at 10 A/g	–	[46]
hollow Co_3O_4 corals	527 F/g at 1 A/g	78% at 10 A/g	99%-5000	[47]
hollow Co_3O_4 nanowires	599 F/g at 2 A/g	73% at 40 A/g	91%-7500	[48]
hollow Co_3O_4 boxes	278 F/g at 0.5 A/g	63% at 5 A/g	–	[49]
hollow Co_3O_4 dodecahedron	1100 F/g at 1.25 A/g	40% at 12.5 A/g	95.1%-6000	[50]
Co_3O_4 spheres	837.7 F/g at 1 A/g	93.6% at 10 A/g	87%-2000	[51]
Co_3O_4 spheres	261.1 F/g at 0.5 A/g	42% at 5 A/g	90.2%-2000	[52]
Co_3O_4 nanorods	739 F/g at 5 mV/s	52.5% at 100 mV/s	103%-50000	[53]
Co_3O_4 nanowires	977 F/g at 2 A/g	49.5% at 10 A/g	90%-2000	[54]
Co_3O_4 nanoflakes	450 F/g at 1 A/g	81% at 20 A/g	92%-5000	[55]
Mn doped Co_3O_4	668.4 F/g at 1 A/g	62% at 10 A/g	104%-10000	[34]
Au decorated Co_3O_4	681 F/g at 0.5 A/g	58% at 10 A/g	83.1%-13000	[42]
$\text{CoO}/\text{Co}_3\text{O}_4$	451 F/g at 1 A/g	68.3% at 20 A/g	108%-5000	[43]
hollow Co_3O_4 spheres	988 F/g at 1 A/g	93.6% at 20 A/g	96.6%-6000	Ours

4. Conclusions

In summary, porous thin-wall hollow Co_3O_4 spheres were successfully prepared through a simple approach and were characterized in detail. The electrochemical studies above unambiguously illuminate that the Co_3O_4 in this work shows prominent specific capacitance and cycling stability, which are attributed to its favorable structural features. Particularly, in comparison with other Co_3O_4 -based electrode materials, it demonstrates an overwhelming rate capability (limited decay of 6.4% from

1 to 20 A/g), which is very critical for commercial applications. These results indicate the exciting supercapacitor application potential of our synthesized material. Moreover, the relationship between the structure and properties is worth investigating in depth in the future.

Author Contributions: X.F. investigated the research, performed the characterizations and analyzed the data; X.F. and Y.S. contributed equally to conduct the experiments and to write the manuscript; P.O. provided the critical feedback and designed the structure of the manuscript; P.O. and X.C. both equally supervised the experiments and refined the manuscript.

Funding: This research was funded by the Norwegian PhD Network on Nanotechnology for Microsystems, which is sponsored by the Research Council of Norway, Division for Science, under contract no. 221860/F60. X.F. was funded by China Scholarship Council.

Acknowledgments: Fruitful discussions with Einar Halvorsen and Pai Lu are acknowledged.

Conflicts of Interest: The authors declare no conflict of interest.

References

1. Hui, K.N.; San Hui, K.; Tang, Z.; Jadhav, V.V.; Xia, Q.X. Hierarchical chestnut-like MnCo_2O_4 nanoneedles grown on nickel foam as binder-free electrode for high energy density asymmetric supercapacitors. *J. Power Sources* **2016**, *330*, 195–203. [[CrossRef](#)]
2. Cui, L.; Huang, L.; Ji, M.; Wang, Y.; Shi, H.; Zuo, Y.; Kang, S. High-performance MgCo_2O_4 nanocone arrays grown on three-dimensional nickel foams: Preparation and application as binder-free electrode for pseudo-supercapacitor. *J. Power Sources* **2016**, *333*, 118–124. [[CrossRef](#)]
3. Tang, Z.; Tang, C.H.; Gong, H. A high energy density asymmetric supercapacitor from nano-architected $\text{Ni}(\text{OH})_2$ /Carbon nanotube electrodes. *Adv. Funct. Mater.* **2012**, *22*, 1272–1278. [[CrossRef](#)]
4. Roy, A.; Jadhav, H.S.; Thorat, G.M.; Seo, J.G. Electrochemical growth of $\text{Co}(\text{OH})_2$ nanoflakes on Ni foam for methanol electro-oxidation. *New J. Chem.* **2017**, *41*, 9546–9553. [[CrossRef](#)]
5. Wang, C.; Zhou, E.; He, W.; Deng, X.; Huang, J.; Ding, M.; Wei, X.; Liu, X.; Xu, X. NiCo_2O_4 -based supercapacitor nanomaterials. *Nanomaterials* **2017**, *7*, 41. [[CrossRef](#)] [[PubMed](#)]
6. Simon, P.; Gogotsi, Y.; Dunn, B. Where do batteries end and supercapacitors begin? *Science* **2014**, *343*, 1210–1211. [[CrossRef](#)]
7. Conway, B.E. Transition from “supercapacitor” to “battery” behavior in electrochemical energy storage. *J. Electrochem. Soc.* **1991**, *138*, 1539–1548. [[CrossRef](#)]
8. González, A.; Goikolea, E.; Barrena, J.A.; Mysyk, R. Review on supercapacitors: Technologies and materials. *Renew. Sustain. Energy Rev.* **2016**, *58*, 1189–1206. [[CrossRef](#)]
9. Vangari, M.; Pryor, T.; Jiang, L. Supercapacitors: Review of materials and fabrication methods. *J. Energy Eng.* **2012**, *139*, 72–79. [[CrossRef](#)]
10. Miller, J.R.; Simon, P. Electrochemical capacitors for energy management. *Science* **2008**, *321*, 651–652. [[CrossRef](#)]
11. Kötz, R.; Carlen, M. Principles and applications of electrochemical capacitors. *Electrochim. Acta* **2000**, *45*, 2483–2498. [[CrossRef](#)]
12. Lu, P.; Müller, L.; Hoffmann, M.; Chen, X. Taper silicon nano-scaffold regulated compact integration of 1D nanocarbons for improved on-chip supercapacitor. *Nano Energy* **2017**, *41*, 618–625. [[CrossRef](#)]
13. Zhang, L.L.; Zhao, X.S. Carbon-based materials as supercapacitor electrodes. *Chem. Soc. Rev.* **2009**, *38*, 2520–2531. [[CrossRef](#)] [[PubMed](#)]
14. Wang, Y.; Shi, Z.; Huang, Y.; Ma, Y.; Wang, C.; Chen, M.; Chen, Y. Supercapacitor devices based on graphene materials. *J. Phys. Chem. C* **2009**, *113*, 13103–13107. [[CrossRef](#)]
15. Zhang, L.L.; Zhou, R.; Zhao, X.S. Graphene-based materials as supercapacitor electrodes. *J. Mater. Chem.* **2010**, *20*, 5983–5992. [[CrossRef](#)]
16. Pan, H.; Li, J.; Feng, Y. Carbon nanotubes for supercapacitor. *Nanoscale Res. Lett.* **2010**, *5*, 654. [[CrossRef](#)]
17. Yu, Z.; Tetard, L.; Zhai, L.; Thomas, J. Supercapacitor electrode materials: Nanostructures from 0 to 3 dimensions. *Energy Environ. Sci.* **2015**, *8*, 702–730. [[CrossRef](#)]
18. Sk, M.M.; Yue, C.Y.; Ghosh, K.; Jena, R.K. Review on advances in porous nanostructured nickel oxides and their composite electrodes for high-performance supercapacitors. *J. Power Sources* **2016**, *308*, 121–140. [[CrossRef](#)]

19. Chen, H.; Hu, L.; Chen, M.; Yan, Y.; Wu, L. Nickel–cobalt layered double hydroxide nanosheets for high-performance supercapacitor electrode materials. *Adv. Funct. Mater.* **2014**, *24*, 934–942. [[CrossRef](#)]
20. Zhi, M.; Xiang, C.; Li, J.; Li, M.; Wu, N. Nanostructured carbon–metal oxide composite electrodes for supercapacitors: A review. *Nanoscale* **2013**, *5*, 72–88. [[CrossRef](#)]
21. Lin, L.; Tang, S.; Zhao, S.; Peng, X.; Hu, N. Hierarchical three-dimensional FeCo₂O₄@MnO₂ core-shell nanosheet arrays on nickel foam for high-performance supercapacitor. *Electrochim. Acta* **2017**, *228*, 175–182. [[CrossRef](#)]
22. Qiu, M.; Sun, P.; Shen, L.; Wang, K.; Song, S.; Yu, X.; Tan, S.; Zhao, C.; Mai, W. WO₃ nanoflowers with excellent pseudo-capacitive performance and the capacitance contribution analysis. *J. Mater. Chem. A* **2016**, *4*, 7266–7273. [[CrossRef](#)]
23. Liu, J.; Jiang, J.; Cheng, C.; Li, H.; Zhang, J.; Gong, H.; Fan, H.J. Co₃O₄ nanowire@MnO₂ ultrathin nanosheet core/shell arrays: A new class of high-performance pseudocapacitive materials. *Adv. Mater.* **2011**, *23*, 2076–2081. [[CrossRef](#)] [[PubMed](#)]
24. Yuan, C.; Yang, L.; Hou, L.; Li, J.; Sun, Y.; Zhang, X.; Shen, L.; Lu, X.; Xiong, S.; Lou, X.W. Flexible hybrid paper made of monolayer Co₃O₄ microsphere arrays on rGO/CNTs and their application in electrochemical capacitors. *Adv. Funct. Mater.* **2012**, *22*, 2560–2566. [[CrossRef](#)]
25. Li, Z.Y.; Bui, P.T.; Kwak, D.H.; Akhtar, M.S.; Yang, O.B. Enhanced electrochemical activity of low temperature solution process synthesized Co₃O₄ nanoparticles for pseudo-supercapacitors applications. *Ceram. Int.* **2016**, *42*, 1879–1885. [[CrossRef](#)]
26. Rakhi, R.B.; Chen, W.; Cha, D.; Alshareef, H.N. Substrate dependent self-organization of mesoporous cobalt oxide nanowires with remarkable pseudocapacitance. *Nano Lett.* **2012**, *12*, 2559–2567. [[CrossRef](#)]
27. He, T.; Chen, D.; Jiao, X.; Xu, Y.; Gu, Y. Surfactant-assisted solvothermal synthesis of Co₃O₄ hollow spheres with oriented-aggregation nanostructures and tunable particle size. *Langmuir* **2004**, *20*, 8404–8408. [[CrossRef](#)]
28. Xia, X.H.; Tu, J.P.; Wang, X.L.; Gu, C.D.; Zhao, X.B. Mesoporous Co₃O₄ monolayer hollow-sphere array as electrochemical pseudocapacitor material. *Chem. Commun.* **2011**, *47*, 5786–5788. [[CrossRef](#)]
29. Yao, M.; Hu, Z.; Xu, Z.; Liu, Y. Template synthesis of 1D hierarchical hollow Co₃O₄ nanotubes as high performance supercapacitor materials. *J. Alloys Compd.* **2015**, *644*, 721–728. [[CrossRef](#)]
30. Zhou, X.; Shen, X.; Xia, Z.; Zhang, Z.; Li, J.; Ma, Y.; Qu, Y. Hollow fluffy Co₃O₄ cages as efficient electroactive materials for supercapacitors and oxygen evolution reaction. *ACS Appl. Mater. Interfaces* **2015**, *7*, 20322–20331. [[CrossRef](#)]
31. Lu, P.; Ohlckers, P.; Müller, L.; Leopold, S.; Hoffmann, M.; Grigoras, K.; Ahopelto, J.; Prunnila, M.; Chen, X. Nano fabricated silicon nanorod array with titanium nitride coating for on-chip supercapacitors. *Electrochem. Commun.* **2016**, *70*, 51–55. [[CrossRef](#)]
32. Lu, P.; Halvorsen, E.; Ohlckers, P.; Müller, L.; Leopold, S.; Hoffmann, M.; Grigoras, K.; Ahopelto, J.; Prunnila, M.; Chen, X. Ternary composite Si/TiN/MnO₂ taper nanorod array for on-chip supercapacitor. *Electrochim. Acta* **2017**, *248*, 397–408. [[CrossRef](#)]
33. Li, W.Y.; Xu, L.N.; Chen, J. Co₃O₄ nanomaterials in lithium-ion batteries and gas sensors. *Adv. Funct. Mater.* **2005**, *15*, 851–857. [[CrossRef](#)]
34. Li, G.; Chen, M.; Ouyang, Y.; Yao, D.; Lu, L.; Wang, L.; Xia, X.; Lei, W.; Chen, S.M.; Hao, Q. Manganese doped Co₃O₄ mesoporous nanoneedle array for long cycle-stable supercapacitors. *Appl. Surf. Sci.* **2019**, *469*, 941–950. [[CrossRef](#)]
35. Wu, H.B.; Pang, H.; Lou, X.W.D. Facile synthesis of mesoporous Ni_{0.3}Co_{2.7}O₄ hierarchical structures for high-performance supercapacitors. *Energy Environ. Sci.* **2013**, *6*, 3619–3626. [[CrossRef](#)]
36. Wang, D.; Wang, Q.; Wang, T. Morphology-controllable synthesis of cobalt oxalates and their conversion to mesoporous Co₃O₄ nanostructures for application in supercapacitors. *Inorg. Chem.* **2011**, *50*, 6482–6492. [[CrossRef](#)]
37. Du, H.; Jiao, L.; Wang, Q.; Yang, J.; Guo, L.; Si, Y.; Wang, Y.; Yuan, H. Facile carbonaceous microsphere templated synthesis of Co₃O₄ hollow spheres and their electrochemical performance in supercapacitors. *Nano Res.* **2013**, *6*, 87–98. [[CrossRef](#)]
38. Zhao, C.; Huang, B.; Fu, W.; Chen, J.; Zhou, J.; Xie, E. Fabrication of porous nanosheet-based Co₃O₄ hollow nanocubes for electrochemical capacitors with high rate capability. *Electrochim. Acta* **2015**, *178*, 555–563. [[CrossRef](#)]

39. Wang, Y.; Lei, Y.; Li, J.; Gu, L.; Yuan, H.; Xiao, D. Synthesis of 3D-nanonet hollow structured Co_3O_4 for high capacity supercapacitor. *ACS Appl. Mater. Interfaces* **2014**, *6*, 6739–6747. [CrossRef]
40. Kumar, R.D.; Andou, Y.; Karuppuhachamy, S. Microwave-assisted synthesis of Zn-WO_3 and ZnWO_4 for pseudocapacitor applications. *J. Phys. Chem. Solids* **2016**, *92*, 94–99. [CrossRef]
41. Ede, S.R.; Ramadoss, A.; Nithyanantham, U.; Anantharaj, S.; Kundu, S. Bio-molecule assisted aggregation of ZnWO_4 nanoparticles (NPs) into chain-like assemblies: Material for high performance supercapacitor and as catalyst for benzyl alcohol oxidation. *Inorg. Chem.* **2015**, *54*, 3851–3863. [CrossRef] [PubMed]
42. Tan, Y.; Liu, Y.; Kong, L.; Kang, L.; Ran, F. Supercapacitor electrode of nano- Co_3O_4 decorated with gold nanoparticles via in-situ reduction method. *J. Power Sources* **2017**, *363*, 1–8. [CrossRef]
43. Pang, M.; Long, G.; Jiang, S.; Ji, Y.; Han, W.; Wang, B.; Liu, X.; Xi, Y.; Wang, D.; Xu, F. Ethanol-assisted solvothermal synthesis of porous nanostructured cobalt oxides ($\text{CoO/Co}_3\text{O}_4$) for high-performance supercapacitors. *Chem. Eng. J.* **2015**, *280*, 377–384. [CrossRef]
44. Yang, G.W.; Xu, C.L.; Li, H.L. Electrodeposited nickel hydroxide on nickel foam with ultrahigh capacitance. *Chem. Commun.* **2008**, 6537–6539. [CrossRef] [PubMed]
45. Wang, Y.; Pan, A.; Zhu, Q.; Nie, Z.; Zhang, Y.; Tang, Y.; Liang, S.; Cao, G. Facile synthesis of nanorod-assembled multi-shelled Co_3O_4 hollow microspheres for high-performance supercapacitors. *J. Power Sources* **2014**, *272*, 107–112. [CrossRef]
46. Zhu, Z.; Han, C.; Li, T.T.; Hu, Y.; Qian, J.; Huang, S. MOF-templated syntheses of porous Co_3O_4 hollow spheres and micro-flowers for enhanced performance in supercapacitors. *CrystEngComm* **2018**, *20*, 3812–3816. [CrossRef]
47. Wang, X.; Zhang, N.; Chen, X.; Liu, J.; Lu, F.; Chen, L.; Shao, G. Facile precursor conversion synthesis of hollow coral-shaped Co_3O_4 nanostructures for high-performance supercapacitors. *Colloids Surf. A* **2019**, *570*, 63–72. [CrossRef]
48. Xia, X.H.; Tu, J.P.; Mai, Y.J.; Wang, X.L.; Gu, C.D.; Zhao, X.B. Self-supported hydrothermal synthesized hollow Co_3O_4 nanowire arrays with high supercapacitor capacitance. *J. Mater. Chem.* **2011**, *21*, 9319–9325. [CrossRef]
49. Du, W.; Liu, R.; Jiang, Y.; Lu, Q.; Fan, Y.; Gao, F. Facile synthesis of hollow Co_3O_4 boxes for high capacity supercapacitor. *J. Power Sources* **2013**, *227*, 101–105. [CrossRef]
50. Zhang, Y.Z.; Wang, Y.; Xie, Y.L.; Cheng, T.; Lai, W.Y.; Pang, H.; Huang, W. Porous hollow Co_3O_4 with rhombic dodecahedral structures for high-performance supercapacitors. *Nanoscale* **2014**, *6*, 14354–14359. [CrossRef]
51. Liu, Z.; Zhou, W.; Wang, S.; Du, W.; Zhang, H.; Ding, C.; Du, Y.; Zhu, L. Facile synthesis of homogeneous core-shell Co_3O_4 mesoporous nanospheres as high performance electrode materials for supercapacitor. *J. Alloys Compd.* **2019**, *774*, 137–144. [CrossRef]
52. Guo, D.; Song, X.; Li, F.; Tan, L.; Ma, H.; Zhang, L.; Zhao, Y. Oriented synthesis of Co_3O_4 core-shell microspheres for high-performance asymmetric supercapacitor. *Colloids Surf. A* **2018**, *546*, 1–8. [CrossRef]
53. Cheng, G.; Kou, T.; Zhang, J.; Si, C.; Gao, H.; Zhang, Z. $\text{O}_2^{2-}/\text{O}^-$ functionalized oxygen-deficient Co_3O_4 nanorods as high performance supercapacitor electrodes and electrocatalysts towards water splitting. *Nano Energy* **2017**, *38*, 155–166. [CrossRef]
54. Wang, Y.; Zhou, T.; Jiang, K.; Da, P.; Peng, Z.; Tang, J.; Kong, B.; Cai, W.B.; Yang, Z.; Zheng, G. Reduced mesoporous Co_3O_4 nanowires as efficient water oxidation electrocatalysts and supercapacitor electrodes. *Adv. Energy Mater.* **2014**, *4*, 1400696. [CrossRef]
55. Xiao, A.; Zhou, S.; Zuo, C.; Zhuan, Y.; Ding, X. Controllable synthesis of mesoporous Co_3O_4 nanoflake array and its application for supercapacitor. *Mater. Res. Bull.* **2014**, *60*, 674–678. [CrossRef]



Article II

Fan, X., Ohlckers, P., & Chen, X. (2020). Tunable Synthesis of Hollow Co_3O_4 Nanoboxes and Their Application in Supercapacitors. *Applied Sciences*, 10(4), 1208. DOI: 10.3390/app10041208

Article

Tunable Synthesis of Hollow Co_3O_4 Nanoboxes and Their Application in Supercapacitors

Xiao Fan, Per Ohlckers *  and Xuyuan Chen *

Department of Microsystems, Faculty of Technology, Natural Sciences and Maritime Sciences, University of South-Eastern Norway, Campus Vestfold, Raveien 215, 3184 Borre, Norway; xiao.fan@usn.no

* Correspondence: per.ohlckers@usn.no (P.O.); xuyuan.chen@usn.no (X.C.); Tel.: +47-310-09-315 (P.O.); +47-310-09-028 (X.C.)

Received: 17 January 2020; Accepted: 7 February 2020; Published: 11 February 2020



Abstract: Hollow Co_3O_4 nanoboxes constructed by numerous nanoparticles were prepared by using a facile method consisting of precipitation, solvothermal and annealing reactions. The desirable hollow structure as well as a highly porous morphology led to synergistically determined and enhanced supercapacitor performances. In particular, the hollow Co_3O_4 nanoboxes were comprehensively investigated to achieve further optimization by tuning the sizes of the nanoboxes, which were well controlled by initial precipitation reaction. The systematical electrochemical measurements show that the optimized Co_3O_4 electrode delivers large specific capacitances of 1832.7 and 1324.5 F/g at current densities of 1 and 20 A/g, and only 14.1% capacitance decay after 5000 cycles. The tunable synthesis paves a new pathway to get the utmost out of Co_3O_4 with a hollow architecture for supercapacitors application.

Keywords: Co_3O_4 ; hollow nanoboxes; supercapacitors; tunable synthesis

1. Introduction

Nowadays, the growing energy crisis has enormously accelerated the demand for efficient, safe and cost-effective energy storage devices [1,2]. Because of unparalleled advantages such as superior power density, strong temperature adaptation, a fast charge/discharge rate and an ultralong service life, supercapacitors have significantly covered the shortage of conventional physical capacitors and batteries, and sparked considerable interest in the last decade [3–5]. Supercapacitors are generally classified into electric double layer capacitors storing energy depending on reversible ions absorption at the interface [6–9] and pseudocapacitors through reversible faradaic redox reactions [10–13]. The different energy storage mechanisms directly determine whether electric double layer capacitors utilize carbonaceous materials as electrode materials [6,7,14], while pseudocapacitors employ transition metal oxides/hydroxides [10,11,15]. Drawing a benefit from faradaic redox reactions, pseudocapacitors usually generate several times higher specific capacitance than that of electric double layer capacitors, and have attracted major attention in recent years [15,16].

Among various transition compounds, Co_3O_4 is extensively recognized as one of the most representative pseudocapacitive materials owing to its abundant resources, environmental friendliness, low cost, strong redox activity and more importantly its superior theoretical specific capacitance (3560 F/g) [17–20]. The series of excellent features have triggered tremendous efforts on Co_3O_4 research for high performance supercapacitors application. To date, various solid or hollow structures of Co_3O_4 have been achieved. The previous progress illustrated the hollow architecture that a highly porous morphology could provide for a large electroactive surface area with extra active sites and facile ions transportation, consequently enhancing the electrochemical properties dramatically [21,22]. For instance, Zhou et al. reported hollow Co_3O_4 cages and presented the specific capacitance of 948.9 F/g at

1 A/g (536.8 F/g at 40 A/g) [23]. The hollow Co_3O_4 nanotubes prepared by Yao et al. demonstrated the specific capacitance of 1006 F/g at 1 A/g (512 F/g at 10 A/g) [24]. Zhu et al. synthesized hollow Co_3O_4 spheres and hollow Co_3O_4 microflowers. The spheres deliver the specific capacitance of 342.1 F/g at 0.5 A/g (235 F/g at 10 A/g), while the microflowers show the specific capacitance of 210 F/g at 0.5 A/g (180 F/g at 10 A/g) [25]. However, the obtained specific capacitances up to now are far lower than their maximum theoretical value. Moreover, the Co_3O_4 also suffers from a poor rate performance. Obviously, both low specific capacitance and poor rate performance severely hinder the practical application of Co_3O_4 . Therefore, even though major contributions are achieved, there is still much room to deeply investigate the ability of the hollow Co_3O_4 to reach a large specific capacitance closer to its maximum theoretical value, as well as an excellent rate capability. Recently, metal-organic frameworks (MOFs), in which zeolitic imidazolate framework (ZIF) is most representative, have received much attention for constructing a hollow nanostructure for supercapacitor applications. By using the ZIF as a self-sacrificial template, a well-defined hollow structure as well as a highly electrolyte ions accessible surface area can be achieved [26–28]. Unfortunately, it is difficult to control the sizes of nanoarchitectures via a facile approach at present, which fails to further enhance the electrochemical performance.

In this paper, hollow Co_3O_4 nanoboxes were successfully prepared from ZIF-67 precursors. The hollow nanostructure and highly porous morphology of the Co_3O_4 synergistically enhance the electrochemical performances. Meanwhile, in this design, the sizes of the nanostructures were well controlled by the precipitation reaction. There are scarce reports about systematically tunable sizes of architectures in hollow Co_3O_4 preparation for high performance supercapacitors. What is more, this distinctive advantage makes the hollow Co_3O_4 nanoboxes comprehensively utilized. In this work, the optimized Co_3O_4 electrode exhibits an unprecedented specific capacitance (1832.7 F/g at 1 A/g), while the specific capacitance is still as high as 1324.5 F/g at 20 A/g. In addition, the capacitance only decays 14.1% after 5000 cycles. The pseudocapacitive performances mark the obtained Co_3O_4 as a promising electrode material candidate for supercapacitors.

2. Materials and Methods

2.1. Synthesis of Dodecahedral Diamond ZIF-67

Dodecahedral diamond ZIF-67 with different diameters were prepared by a precipitation method. To achieve this, 0.273, 0.102 or 0.068 M of 2-methylimidazole methanol solution was added to 0.04 M of cobalt nitrate methanol solution. The mixed solution was stirred for 30 min. Then the cloudy solution was kept static for 24 h at room temperature. The purple precipitates (denoted as ZIF-67-1, ZIF-67-2 and ZIF-67-3) were obtained and washed with methanol via centrifugation.

2.2. Conversion to Hollow Co-LDH (Co-Layered Double Hydroxide)

The hollow structures were transformed from ZIF-67 (-1, -2, -3) by using a solvothermal reaction. Afterwards, 0.05 g of ZIF-67 (-1, -2, -3) was dispersed in 0.01 M cobalt nitrate methanol solution and stirred for 10 min. After that, the pink slurry was transferred to a Teflon-lined stainless-steel autoclave and kept at 120 °C for 1 h. The brown precipitates (named as Co-LDH-1, Co-LDH-2 and Co-LDH-3) were obtained and washed with methanol via centrifugation.

2.3. Preparation of Hollow Co_3O_4 Nanoboxes

The Co-LDH (-1, -2, -3) were dried in an oven at 60 °C overnight and calcinated at 500 °C for 2 h. The final products were called Co_3O_4 -1, Co_3O_4 -2 and Co_3O_4 -3.

2.4. Material Characterizations

The morphological and structural features of as-prepared samples were examined by scanning electron microscope (SEM, Hitachi SU8230) at 10 kV. The crystallinity and crystal phase were investigated

through X-ray powder diffraction (XRD, EQUINOX 1000) with Cu-K α_1 radiation ($\lambda = 1.5406 \text{ \AA}$) at a scanning speed of $6^\circ/\text{min}$.

2.5. Electrode Fabrication

Nickel foam (NF, $1.0 \text{ cm} \times 1.0 \text{ cm}$) was selected as the current collector. The as-prepared Co_3O_4 (80 wt%), acetylene black (15 wt%) and Polyvinylidene fluoride (PVDF, 5 wt%) were added to N-Methyl-2-pyrrolidone (NMP) and grinded in a mortar thoroughly. The resulting mixture was pressed on NF and dried in an oven at 100°C overnight. The loading mass was approximately 1 mg.

2.6. Electrochemical Measurements

Cyclic voltammetry (CV) at typical scan rates (5, 10, 20, 50 and 100 mV/s), galvanostatic charge/discharge (GCD) at representative current densities (1, 2, 5, 10 and 20 A/g) and electrochemical impedance spectroscopy (EIS) in wide frequency range (100 mHz–100 kHz) were conducted on an electrochemical workstation (Zahner IM6). The configuration, potential window, electrolyte, counter electrode and reference electrode were set as three-electrode system, 0–0.65 V, 2 M KOH, Pt net and Ag/AgCl (3.5 M KCl), respectively.

The specific capacitance of the active material is calculated based on a GCD test according to Equation (1) [29]:

$$C = \frac{I\Delta t}{m\Delta V}, \quad (1)$$

where: C (F/g) is the specific capacitance; I (A) is the discharge current; Δt (s) is the discharge time; ΔV (V) is the voltage window; and m (g) is the mass of active material.

3. Results

Figure 1 presents the XRD patterns of the calcination products. The identified diffraction peaks of all samples can be assigned to the face centered Co_3O_4 (JCPDS No. 42-1467, space group: $Fd\bar{3}m$ (227)), suggesting a high purity of the samples [30]. According to the Scherrer equation [31], the crystallite sizes of Co_3O_4 -1, Co_3O_4 -2 and Co_3O_4 -3 are around 23.6, 20.0 and 24.3 nm, respectively.

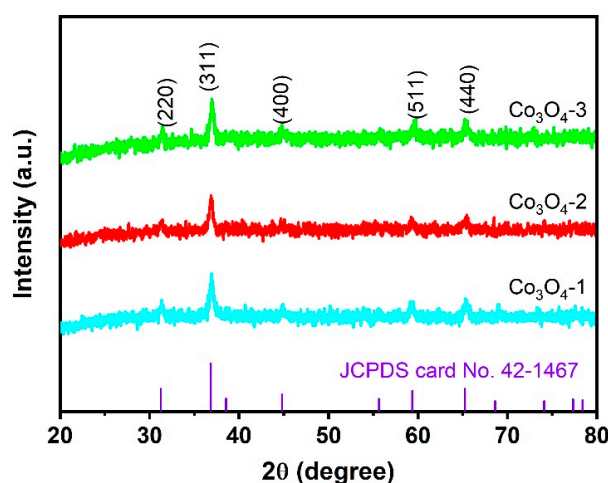


Figure 1. X-ray powder diffraction (XRD) patterns of Co_3O_4 -1, Co_3O_4 -2 and Co_3O_4 -3.

Typical SEM images of ZIF-67 are shown in Figure 2a–c. The ZIF-67 present monodispersity and the average sizes of ZIF-67-1, ZIF-67-2 and ZIF-67-3 are 0.39 ± 0.05 , 1.98 ± 0.18 and $3.28 \pm 0.37 \mu\text{m}$, respectively. Namely, the average sizes increase with the decrease of 2-methylimidazole concentration. This phenomenon is attributed to the stepwise formation of ZIF-67. The process can be briefly divided into a nucleation phase and growth stage. In the initial nucleation phase, the

increased concentration of 2-methylimidazole enhanced the nucleation rate, determining a small size of each unit cell. Subsequently, diffusive particles slowly grew around the cell to form ZIF-67 [32,33]. After the conversion, the ZIF-67 transferred to hollow Co-LDH with a significant morphology change. Figure 2d–f shows that there were nanosheets vertically growing on the surface of as-formed ZIF-67 and the average sizes shrunk a little bit. Meanwhile, with the continuous dissolution of the inner cobalt, the hollow Co-LDH nanoboxes with different sizes were formed. Hollow Co_3O_4 were obtained through calcination, as displayed in Figure 2g–i. Beyond expectations, the overall size and hollow feature were well maintained even after heat treatment, except for Co_3O_4 -1 due to the very thin configuration of the shell. It could be dimly seen that the shell of hollow Co_3O_4 consisted of small nanoparticles.

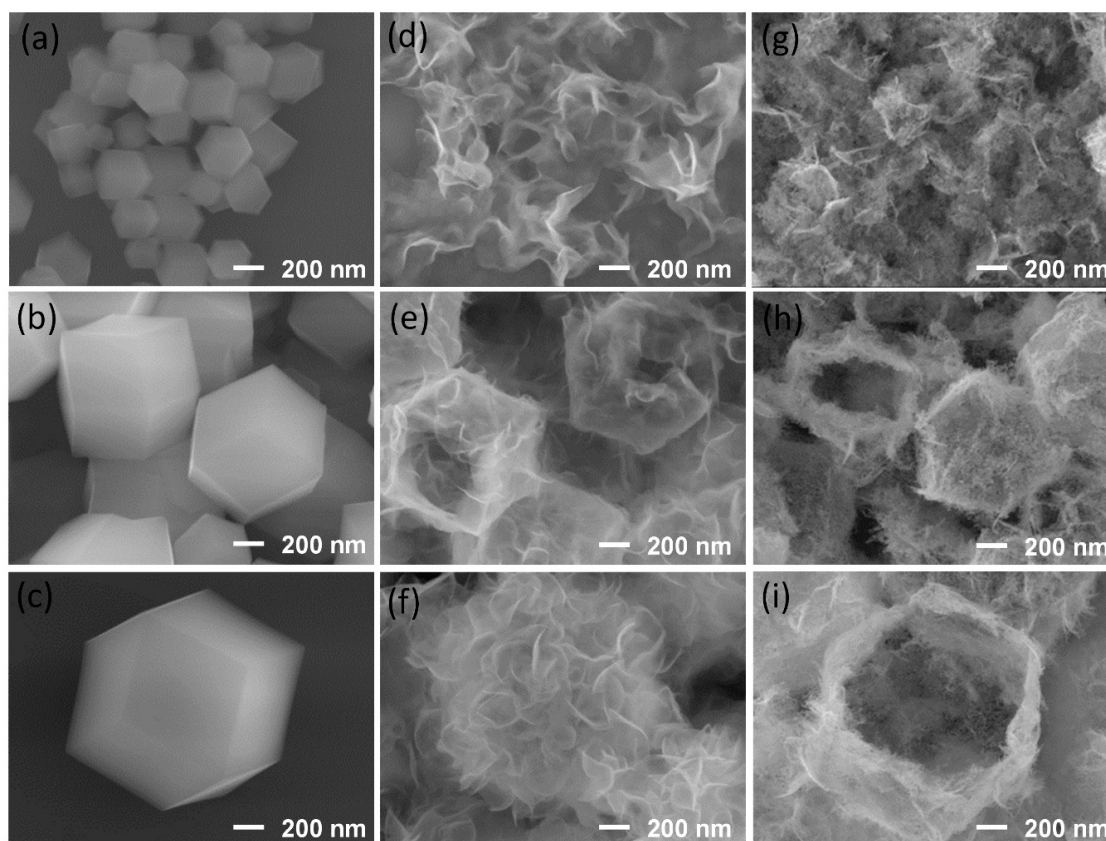


Figure 2. Scanning electron microscope (SEM) images of dodecahedral diamond zeolitic imidazolate framework-67 (ZIF-67): (a) ZIF-67-1, (b) ZIF-67-2, (c) ZIF-67-3; hollow Co-layered double hydroxide (Co-LDH): (d) Co-LDH-1, (e) Co-LDH-2, (f) Co-LDH-3; hollow Co_3O_4 : (g) Co_3O_4 -1, (h) Co_3O_4 -2, (i) Co_3O_4 -3.

The CV measurements in a potential range of 0–0.65 V (vs. Ag/AgCl) were first characterized to reveal the supercapacitors behavior of the Co_3O_4 electrodes. Figure 3a presents CV curves of the Co_3O_4 with different sizes at a scan rate of 5 mV/s. As expected, all samples deliver a distinct pair of peaks induced by a faradaic redox reaction, which clearly reveals the typical pseudocapacitive characteristics [23,24]. In particular, the integrated area under CV curve of Co_3O_4 -2 electrode is the largest among three Co_3O_4 electrodes, demonstrating that the Co_3O_4 -2 possesses the largest specific capacitance [34]. The CV curves of the Co_3O_4 -2 electrode measured at typical scan rates from 5 to 100 mV/s are displayed in Figure 3b. The following classical and desirable pseudocapacitive phenomena were observed: (1) the CV curves are highly symmetrical; (2) the peak currents remarkably increase along with the increase of scan rates; (3) the peak position also changes accompanied by the increase of scan rates. The peaks generated in the anodic sweep shifted to a higher potential value, while the peaks which originated from the cathodic sweep moved towards a lower potential value; (4) no

significant distortion existed in a comparison of CV curves obtained at 5 and 100 mV/s. Notably, the obvious increase of peak currents and excellent symmetries in CV curves as well as negligible distortion indicate the rapid and well reversible redox process [30], further possibly resulting in an outstanding rate capability.

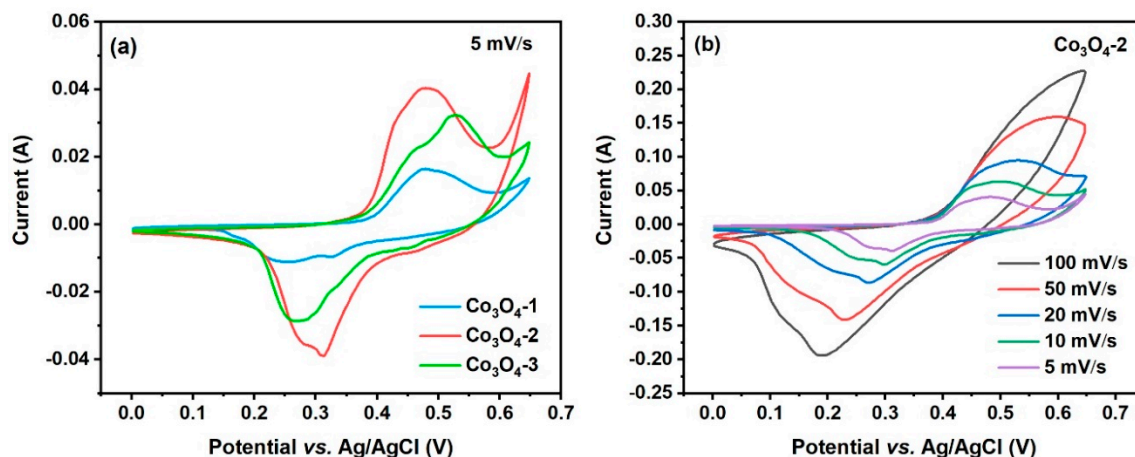


Figure 3. (a) Cyclic voltammetry (CV) curves of Co_3O_4 -1, Co_3O_4 -2 and Co_3O_4 -3 electrodes at scan rate of 5 mV/s; (b) CV curves of Co_3O_4 -2 electrode at typical scan rates ranging from 5 to 100 mV/s.

GCD tests between potential window of 0–0.65 V (vs. Ag/AgCl) were conducted to further investigate the capacitive properties. The discharge curves of Co_3O_4 -1, Co_3O_4 -2 and Co_3O_4 -3 electrodes at representative current densities of 1, 2, 5, 10 and 20 A/g are presented in Figure 4a–c, respectively. It is intuitive that all discharge curves deliver evident plateaus coinciding with the redox reaction, which also confirms the pseudocapacitive behavior of each Co_3O_4 [25,30]. In addition, the GCD performances comparison at current densities of 1 A/g shown in Figure 4d also confirms the Co_3O_4 -2 sample offers the largest specific capacitance [29], which is consistent with the aforementioned CV result (Figure 3a).

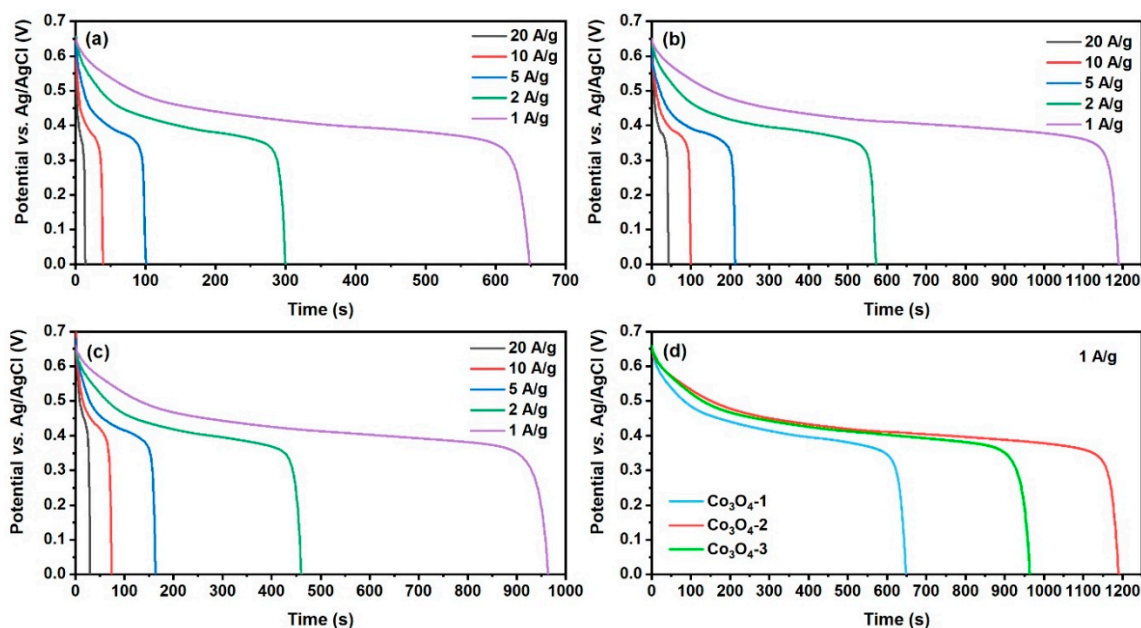


Figure 4. Discharge curves at representative current densities ranging from 1 to 20 A/g: (a) Co_3O_4 -1, (b) Co_3O_4 -2, (c) Co_3O_4 -3; (d) discharge curves of Co_3O_4 -1, Co_3O_4 -2 and Co_3O_4 -3 electrodes at current density of 1 A/g.

The specific capacitances based on GCD measurements are calculated according to Equation (1) for all Co_3O_4 electrodes, and the results are plotted in Figure 5. The Co_3O_4 -2 electrode exhibits the specific capacitances of 1832.7, 1760.9, 1640.4, 1526.6 and 1324.5 F/g at 1, 2, 5, 10 and 20 A/g, respectively. Moreover, Figure 5 demonstrates that the boost in current densities leads to a decrease in specific capacitances. Unfortunately, the similar fading tendencies of Co_3O_4 -1, Co_3O_4 -2 and Co_3O_4 -3 are inevitable owing to the correlation between current density and electrolytic ions diffusion (OH^- in this study) in electrode material (Co_3O_4 in this study). Namely, compared with the diffusion at high current density, the OH^- ions have relatively sufficient time to transfer at a low current density. The phenomenon gives rise to inner active sites failing to be comprehensively devoted to the redox reaction at high current density. In contrast, both the inner and outer surface can be involved at low current density, thoroughly making a redox reaction proceed and thus contributing to a large specific capacitance [35]. Nevertheless, the Co_3O_4 -2 electrode can maintain capacitance of 72.3% from 1 to 20 A/g (43.5% of Co_3O_4 -1, 62.6% of Co_3O_4 -3). The slight decay provides the Co_3O_4 -2 bright application with the high power required for energy storage devices. The relieved fading in specific capacitances can be explained by the unique morphology of synthesized Co_3O_4 . During the redox process, the hollow structure can serve as an “ OH^- ions buffer reservoir” [35] to effectively minimize the influence of limited ions diffusion at a high current density on rate performance. In short, the impressive performances in specific capacitance and rate capability make the as-synthesized Co_3O_4 -2 a promising electrode material in supercapacitors application.

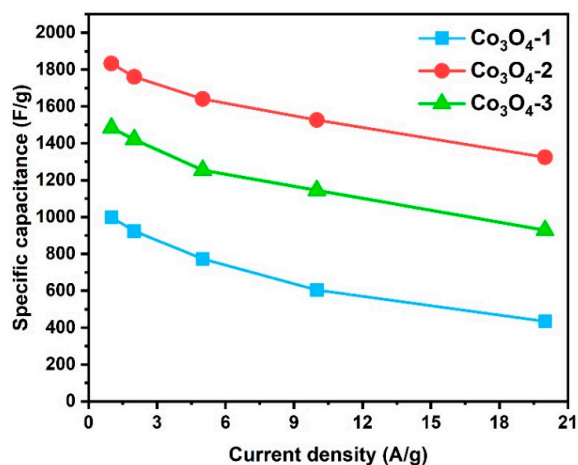


Figure 5. Specific capacitances of Co_3O_4 -1, Co_3O_4 -2 and Co_3O_4 -3 electrodes as a function of current densities.

Figure 6a illustrates the Nyquist plots of different Co_3O_4 electrodes from frequency range of 100 mHz to 100 kHz. The plots of Co_3O_4 -1, Co_3O_4 -2 and Co_3O_4 -3 are similar, which consists of a semicircle and a straight line. The intersection value of plot and real axis reflects the intrinsic resistance and interface resistance of electrolyte and active material (denoted as R_s) [35]. The R_s of Co_3O_4 -1, Co_3O_4 -2 and Co_3O_4 -3 are 0.55, 0.52 and 0.53 Ω , respectively (tiny difference). The semicircle acquired in high frequency range represents the double-layer capacitance (C_{dl}) and the charge-transfer resistance (R_{ct} , corresponds to the semicircle diameter). The semicircle also expresses that the C_{dl} and R_{ct} are connected in parallel [36]. Apparently, the R_{ct} value of Co_3O_4 -2 is much smaller than Co_3O_4 -1 and Co_3O_4 -3 (Figure 6b). In low frequency region, the approximate line in Nyquist plot is related to the interfacial diffusive process and determined by pseudocapacitance (C_{ps}) and Warburg element (W). The equivalent circuit is shown in Figure 6c. Benefited from the hollow structure constructed by numerous nanoparticles, the slopes for all electrodes are larger than 45° , which presents an efficient electrolyte diffusion. Furthermore, a quasi-vertical line displayed by the plot of Co_3O_4 -2 electrode implies a scarcely limited ions diffusion and the behavior tends to an ideal capacitor [23,36]. The

merits of Co₃O₄-2 electrode proposed in EIS results well coincide with the superior electrochemical performance of Co₃O₄-2 electrode in CV and GCD assessments.

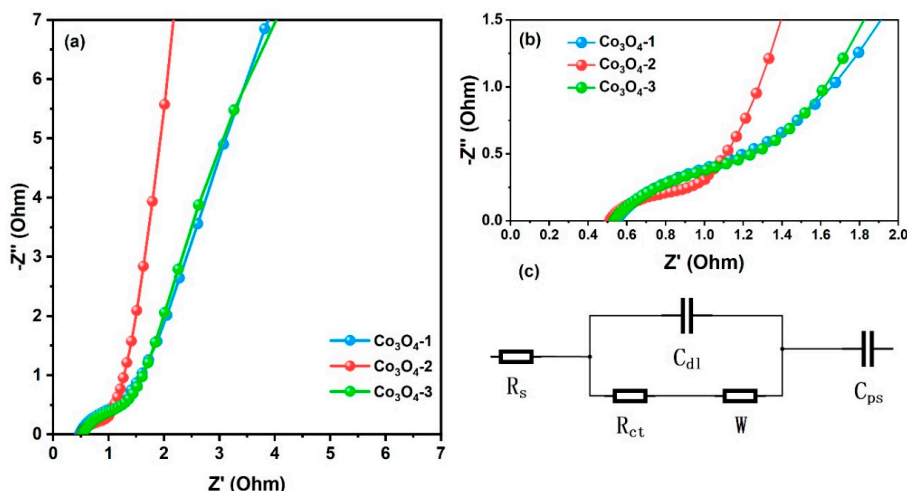


Figure 6. (a) Electrochemical impedance spectroscopy (EIS) plots of Co₃O₄-1, Co₃O₄-2 and Co₃O₄-3 electrodes; (b) enlarged view of high frequency region; (c) equivalent circuit involves intrinsic resistance and interface resistance (R_s), double-layer capacitance (C_{dl}), charge-transfer resistance (R_{ct}), Warburg element (W) and pseudocapacitance (C_{ps}).

The Co₃O₄-2 was employed as the optimized electrode through CV, GCD and EIS results for long term cycling investigation, as recorded in Figure 7. The evaluation was carried out by using a repetitive GCD process at 20 A/g. The Co₃O₄-2 electrode retains 85.9% of its initial specific capacitance even after undergoing 5000 cycles. The insets display the GCD curves of the Co₃O₄-2 electrode at first and last for 10 cycles. The coulombic efficiency (η) is also an important criterion for evaluating the durability and can be calculated based on Equation (2) [37]:

$$\eta = \frac{t_d}{t_c}, \tag{2}$$

where t_d (s) is the discharge time and t_c (s) is the charge time. All deduced coulombic efficiency values reach over 95%. The excellent electrochemical stability of Co₃O₄-2 electrode is significant for possible commercial application.

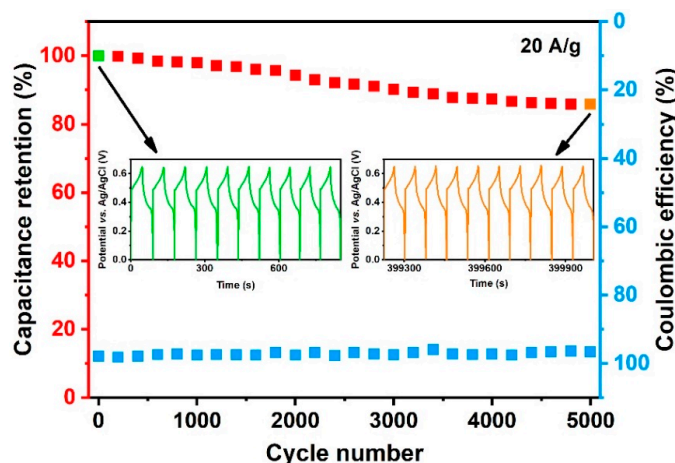


Figure 7. Cycling performance and coulombic efficiency of Co₃O₄-2 electrode. The insets are GCD curves at the first and last 10 cycles.

4. Discussion

In this study, the different electrochemical performances of Co₃O₄-1, Co₃O₄-2 and Co₃O₄-3 are determined by their own structural features. For Co₃O₄-1, mass collapsed structures accompanied the loss of opening pores, which were caused by ultrathin shells, while severely reducing the available surface area, as observed from a SEM image (Figure 2g). In contrast, during the fabricated process of Co₃O₄-2 and Co₃O₄-3, morphologies were well inherited not only in synthesis of Co-LDH from a ZIF-67 precursor but also in conversion of Co-LDH to Co₃O₄ (negligible aggregation). The hollow nature as well as the highly porous architecture (the shell is assembled by numerous nanoparticles) provide a large electrochemical active area with increased active sites for redox reactions. In addition, the unique morphology also significantly facilitates electron transportation and ion diffusion and permeation in electroactive material. The relatively lower electrochemical performance of Co₃O₄-3 electrode is possibly due to the decreased accessibility of electrolyte ions into material produced by the large size and thick shell [38–40]. Table 1 compares this work with other Co₃O₄ based electrodes reported in previous literature. It clearly demonstrates that the specific capacitance of hollow Co₃O₄ nanoboxes electrode in this research is competitive, and even higher than some Co₃O₄ hybrid materials. More importantly, the Co₃O₄ electrode reaches a specific capacitance of 1324.5 F/g at a high current density of 20 A/g. The value at 20 A/g is superior to some Co₃O₄ electrodes at 1 A/g. Except for the two criterions, a slight capacitance decay of 14.1% after 5000 cycles is also worth noting.

Table 1. Specific capacitances at low current density and high current density (rate performance) of Co₃O₄ based electrode materials.

Material	Specific Capacitance (F/g)/ Low Current Density (A/g)	Specific Capacitance (F/g)/ High Current Density (A/g)	Ref.
hollow Co ₃ O ₄ 3D-nanonet	739/1	533/15	[35]
hollow Co ₃ O ₄ spheres	474.8/1	377.4/10	[37]
hollow Co ₃ O ₄ spheres	460/4	401/20	[41]
hollow Co ₃ O ₄ corals	527/1	412/10	[42]
hollow Co ₃ O ₄ dodecahedron	1100/1.25	437/12.5	[43]
hollow Co ₃ O ₄ nanowires	599/2	439 /40	[44]
Co ₃ O ₄ nanowires	977/2	484/10	[45]
Co ₃ O ₄ nanosheets	1121/1	873/25	[46]
Co ₃ O ₄ nanoflakes	448/0.5	421/10	[47]
Co ₃ O ₄ nanobooks	590/0.5	421/8	[48]
Co ₃ O ₄ nanoplates	355.6/0.4	230/4	[49]
Co ₃ O ₄ nanofibers	340/1	296/10	[50]
carbon incorporated Co ₃ O ₄	978.9/0.5	303.3/15	[51]
Mn doped Co ₃ O ₄	773/1	485/16	[52]
Co ₃ O ₄ /CoMoO ₄	1902 /1	1200/10	[53]
Co ₃ O ₄ /NiO	1236.7/1	836.7/20	[54]
Co ₃ O ₄ /Ni(OH) ₂	1306.3/1.2	600 /12.1	[55]
graphene/Co ₃ O ₄	1765 /1	1266 /20	[56]
rGO/Co ₃ O ₄	546/0.5	496/5	[57]
NiO/Co ₃ O ₄ /MnO ₂	1055.3/0.2	727.4/4	[58]
hollow Co ₃ O ₄ nanoboxes	1832.7/1	1324.5/20	Ours

5. Conclusions

In summary, hollow Co₃O₄ nanoboxes were synthesized successfully by using a facile method, in which the overall sizes of the Co₃O₄ were effectively controlled and as a consequence resulted in different supercapacitor performances. An overwhelming specific capacitance of 1832.7 F/g at 1 A/g and a comparable cycling stability of 85.9% after 5000 cycles are achieved in optimal Co₃O₄ electrode. In particular, the Co₃O₄ electrode still retains 72.3% of the specific capacitance, even at 20 A/g. The outstanding performances qualify the hollow Co₃O₄ nanoboxes an attractive electrode material in research field and commercial application of supercapacitors. Furthermore, the morphologic features

and tunable sizes make the applications of as-prepared Co_3O_4 promisingly extend to other aspects, especially in highly accessible surface area required fields, such as catalysts and gas sensors.

Author Contributions: Conceptualization, X.C.; Methodology, P.O. and X.C.; Investigation, X.F., P.O. and X.C.; Data Curation, X.F.; Formal Analysis, X.F.; Validation, X.F., P.O. and X.C.; Writing—Original Draft Preparation, X.F.; Writing—Review & Editing, P.O. and X.C.; Supervision, P.O. and X.C.; Project Administration, P.O. and X.C. All authors have read and agreed to the published version of the manuscript.

Funding: This research was mainly funded by Research Council of Norway (RCN), grant number 221860/F60.

Acknowledgments: X.F. is funded by China Scholarship Council (CSC), grant number 201506930018. The authors also thank the Norwegian Micro- and Nano-Fabrication Facility, NorFab, project number 245963 and Pai Lu for SEM characterization. Critical comments by Einar Halvorsen and Yongjiao Sun are acknowledged.

Conflicts of Interest: The authors declare no conflict of interest.

References

1. Wang, H.; Casalongue, H.S.; Liang, Y.; Dai, H. $\text{Ni}(\text{OH})_2$ nanoplates grown on graphene as advanced electrochemical pseudocapacitor materials. *J. Am. Chem. Soc.* **2010**, *132*, 7472–7477. [[CrossRef](#)] [[PubMed](#)]
2. Zuo, W.; Li, R.; Zhou, C.; Li, Y.; Xia, J.; Liu, J. Battery-Supercapacitor hybrid devices: Recent progress and future prospects. *Adv. Sci.* **2017**, *4*, 1600539. [[CrossRef](#)] [[PubMed](#)]
3. Gao, H.; Xiao, F.; Ching, C.B.; Duan, H. High-Performance asymmetric supercapacitor based on graphene hydrogel and nanostructured MnO_2 . *ACS Appl. Mater. Interfaces* **2012**, *4*, 2801–2810. [[CrossRef](#)]
4. Yan, J.; Fan, Z.; Sun, W.; Ning, G.; Wei, T.; Zhang, Q.; Zhang, R.; Zhi, L.; Wei, F. Advanced asymmetric supercapacitors based on $\text{Ni}(\text{OH})_2$ /graphene and porous graphene electrodes with high energy density. *Adv. Funct. Mater.* **2012**, *22*, 2632–2641. [[CrossRef](#)]
5. Yang, P.; Xiao, X.; Li, Y.; Ding, Y.; Qiang, P.; Tan, X.; Mai, W.; Lin, Z.; Wu, W.; Li, T.; et al. Hydrogenated ZnO core-shell nanocables for flexible supercapacitors and self-powered systems. *ACS Nano* **2013**, *7*, 2617–2626. [[CrossRef](#)] [[PubMed](#)]
6. Pandolfo, A.G.; Hollenkamp, A.F. Carbon properties and their role in supercapacitors. *J. Power Sources* **2006**, *157*, 11–27. [[CrossRef](#)]
7. Zhu, Y.; Murali, S.; Stoller, M.D.; Ganesh, K.J.; Cai, W.; Ferreira, P.J.; Pirkle, A.; Wallace, R.M.; Cychosz, K.A.; Thommes, M.; et al. Carbon-Based supercapacitors produced by activation of graphene. *Science* **2011**, *332*, 1537–1541. [[CrossRef](#)]
8. An, K.H.; Kim, W.S.; Park, Y.S.; Moon, J.M.; Bae, D.J.; Lim, S.C.; Lee, Y.S.; Lee, Y.H. Electrochemical properties of high-power supercapacitors using single-walled carbon nanotube electrodes. *Adv. Funct. Mater.* **2001**, *11*, 387–392. [[CrossRef](#)]
9. Yun, Y.S.; Park, H.H.; Jin, H.J. Pseudocapacitive effects of N-doped carbon nanotube electrodes in supercapacitors. *Materials* **2012**, *5*, 1258–1266. [[CrossRef](#)]
10. Lu, Q.; Chen, J.G.; Xiao, J.Q. Nanostructured electrodes for high-performance pseudocapacitors. *Angew. Chem. Int. Ed.* **2013**, *52*, 1882–1889. [[CrossRef](#)]
11. Chen, Y.C.; Wen, C.Y.; Wang, C.M.; Ho, C.W.; Lin, S.Y.; Chen, Y.L. Characterization of transition-metal oxide deposition on carbon electrodes of a supercapacitor. *Appl. Sci.* **2016**, *6*, 413. [[CrossRef](#)]
12. Hu, L.; Chen, W.; Xie, X.; Liu, N.; Yang, Y.; Wu, H.; Yao, Y.; Pasta, M.; Alshareef, H.N.; Cui, Y. Symmetrical MnO_2 -carbon nanotube-textile nanostructures for wearable pseudocapacitors with high mass loading. *ACS Nano* **2011**, *5*, 8904–8913. [[CrossRef](#)] [[PubMed](#)]
13. Li, H.B.; Yu, M.H.; Wang, F.X.; Liu, P.; Liang, Y.; Xiao, J.; Wang, C.X.; Tong, Y.X.; Yang, G.W. Amorphous nickel hydroxide nanospheres with ultrahigh capacitance and energy density as electrochemical pseudocapacitor materials. *Nat. Commun.* **2013**, *4*, 1894. [[CrossRef](#)] [[PubMed](#)]
14. Cao, X.; Shi, Y.; Shi, W.; Lu, G.; Huang, X.; Yan, Q.; Zhang, Q.; Zhang, H. Preparation of novel 3D graphene networks for supercapacitor applications. *Small* **2011**, *7*, 3163–3168. [[CrossRef](#)] [[PubMed](#)]
15. Zhang, X.; Shi, W.; Zhu, J.; Kharistal, D.J.; Zhao, W.; Lalia, B.S.; Hng, H.H.; Yan, Q. High-Power and high-energy-density flexible pseudocapacitor electrodes made from porous CuO nanobelts and single-walled carbon nanotubes. *ACS Nano* **2011**, *5*, 2013–2019. [[CrossRef](#)] [[PubMed](#)]

16. Zhou, K.; Zhou, W.; Yang, L.; Lu, J.; Cheng, S.; Mai, W.; Tang, Z.; Li, L.; Chen, S. Ultrahigh-Performance pseudocapacitor electrodes based on transition metal phosphide nanosheets array via phosphorization: A general and effective approach. *Adv. Funct. Mater.* **2015**, *25*, 7530–7538. [[CrossRef](#)]
17. Abouali, S.; Akbari Garakani, M.; Zhang, B.; Xu, Z.L.; Kamali Heidari, E.; Huang, J.Q.; Huang, J.; Kim, J.K. Electrospun carbon nanofibers with in situ encapsulated Co_3O_4 nanoparticles as electrodes for high-performance supercapacitors. *ACS Appl. Mater. Interfaces* **2015**, *7*, 13503–13511. [[CrossRef](#)]
18. Meng, T.; Xu, Q.Q.; Wang, Z.H.; Li, Y.T.; Gao, Z.M.; Xing, X.Y.; Ren, T.Z. Co_3O_4 nanorods with self-assembled nanoparticles in queue for supercapacitor. *Electrochim. Acta* **2015**, *180*, 104–111. [[CrossRef](#)]
19. Fan, H.; Quan, L.; Yuan, M.; Zhu, S.; Wang, K.; Zhong, Y.; Chang, L.; Shao, H.; Wang, J.; Zhang, J.; et al. Thin Co_3O_4 nanosheet array on 3D porous graphene/nickel foam as a binder-free electrode for high-performance supercapacitors. *Electrochim. Acta* **2016**, *188*, 222–229. [[CrossRef](#)]
20. Wang, J.; Dou, W.; Zhang, X.; Han, W.; Mu, X.; Zhang, Y.; Zhao, X.; Chen, Y.; Yang, Z.; Su, Q.; et al. Embedded Ag quantum dots into interconnected Co_3O_4 nanosheets grown on 3D graphene networks for high stable and flexible supercapacitors. *Electrochim. Acta* **2017**, *224*, 260–268. [[CrossRef](#)]
21. Guan, C.; Liu, X.; Ren, W.; Li, X.; Cheng, C.; Wang, J. Rational design of metal-organic framework derived hollow NiCo_2O_4 arrays for flexible supercapacitor and electrocatalysis. *Adv. Energy Mater.* **2017**, *7*, 1602391. [[CrossRef](#)]
22. Hu, H.; Guan, B.Y.; Lou, X.W.D. Construction of complex CoS hollow structures with enhanced electrochemical properties for hybrid supercapacitors. *Chem* **2016**, *1*, 102–113. [[CrossRef](#)]
23. Zhou, X.; Shen, X.; Xia, Z.; Zhang, Z.; Li, J.; Ma, Y.; Qu, Y. Hollow fluffy Co_3O_4 cages as efficient electroactive materials for supercapacitors and oxygen evolution reaction. *ACS Appl. Mater. Interfaces* **2015**, *7*, 20322–20331. [[CrossRef](#)] [[PubMed](#)]
24. Yao, M.; Hu, Z.; Xu, Z.; Liu, Y. Template synthesis of 1D hierarchical hollow Co_3O_4 nanotubes as high performance supercapacitor materials. *J. Alloys Compd.* **2015**, *644*, 721–728. [[CrossRef](#)]
25. Zhu, Z.; Han, C.; Li, T.T.; Hu, Y.; Qian, J.; Huang, S. MOF-Templated syntheses of porous Co_3O_4 hollow spheres and micro-flowers for enhanced performance in supercapacitors. *CrystEngComm* **2018**, *20*, 3812–3816. [[CrossRef](#)]
26. Wu, J.; Zhang, X.; Wei, F.; Sui, Y.; Qi, J. Controllable synthesis of ZIF-derived nano-hexahedron porous carbon for supercapacitor electrodes. *Mater. Lett.* **2020**, *258*, 126761. [[CrossRef](#)]
27. Qu, C.; Jiao, Y.; Zhao, B.; Chen, D.; Zou, R.; Walton, K.S.; Liu, M. Nickel-Based pillared MOFs for high-performance supercapacitors: Design, synthesis and stability study. *Nano Energy* **2016**, *26*, 66–73. [[CrossRef](#)]
28. Xu, J.; Liu, S.; Liu, Y. $\text{Co}_3\text{O}_4/\text{ZnO}$ nanoheterostructure derived from core-shell ZIF-8@ZIF-67 for supercapacitors. *RSC Adv.* **2016**, *6*, 52137–52142. [[CrossRef](#)]
29. Liu, W.; Li, X.; Zhu, M.; He, X. High-Performance all-solid state asymmetric supercapacitor based on Co_3O_4 nanowires and carbon aerogel. *J. Power Sources* **2015**, *282*, 179–186. [[CrossRef](#)]
30. Zhang, F.; Yuan, C.; Zhu, J.; Wang, J.; Zhang, X.; Lou, X.W. Flexible films derived from electrospun carbon nanofibers incorporated with Co_3O_4 hollow nanoparticles as self-supported electrodes for electrochemical capacitors. *Adv. Funct. Mater.* **2013**, *23*, 3909–3915. [[CrossRef](#)]
31. Ren, Q.; Feng, Z.; Mo, S.; Huang, C.; Li, S.; Zhang, W.; Chen, L.; Fu, M.; Wu, J.; Ye, D. 1D- Co_3O_4 , 2D- Co_3O_4 , 3D- Co_3O_4 for catalytic oxidation of toluene. *Catal. Today* **2019**, *332*, 160–167. [[CrossRef](#)]
32. Jo, Y.M.; Kim, T.H.; Lee, C.S.; Lim, K.; Na, C.W.; Abdel-Hady, F.; Wazzan, A.A.; Lee, J.H. Metal-Organic framework-derived hollow hierarchical Co_3O_4 nanocages with tunable size and morphology: Ultrasensitive and highly selective detection of methylbenzenes. *ACS Appl. Mater. Interfaces* **2018**, *10*, 8860–8868. [[CrossRef](#)] [[PubMed](#)]
33. Tanaka, S.; Kida, K.; Okita, M.; Ito, Y.; Miyake, Y. Size-Controlled synthesis of zeolitic imidazolate framework-8 (ZIF-8) crystals in an aqueous system at room temperature. *Chem. Lett.* **2012**, *41*, 1337–1339. [[CrossRef](#)]
34. Lu, P.; Halvorsen, E.; Ohlckers, P.; Müller, L.; Leopold, S.; Hoffmann, M.; Grigoras, K.; Ahopelto, J.; Prunnila, M.; Chen, X. Ternary composite Si/TiN/MnO₂ taper nanorod array for on-chip supercapacitor. *Electrochim. Acta* **2017**, *248*, 397–408. [[CrossRef](#)]
35. Wang, Y.; Lei, Y.; Li, J.; Gu, L.; Yuan, H.; Xiao, D. Synthesis of 3D-nanonet hollow structured Co_3O_4 for high capacity supercapacitor. *ACS Appl. Mater. Interfaces* **2014**, *6*, 6739–6747. [[CrossRef](#)]

36. Qiu, M.; Sun, P.; Shen, L.; Wang, K.; Song, S.; Yu, X.; Tan, S.; Zhao, C.; Mai, W. WO₃ nanoflowers with excellent pseudo-capacitive performance and the capacitance contribution analysis. *J. Mater. Chem. A* **2016**, *4*, 7266–7273. [[CrossRef](#)]
37. Du, H.; Jiao, L.; Wang, Q.; Yang, J.; Guo, L.; Si, Y.; Wang, Y.; Yuan, H. Facile carbonaceous microsphere templated synthesis of Co₃O₄ hollow spheres and their electrochemical performance in supercapacitors. *Nano Res.* **2013**, *6*, 87–98. [[CrossRef](#)]
38. Yang, W.; Yang, W.; Ding, F.; Sang, L.; Ma, Z.; Shao, G. Template-Free synthesis of ultrathin porous carbon shell with excellent conductivity for high-rate supercapacitors. *Carbon* **2017**, *111*, 419–427. [[CrossRef](#)]
39. Peng, S.; Li, L.; Tan, H.; Cai, R.; Shi, W.; Li, C.; Mhaisalkar, S.G.; Srinivasan, M.; Ramakrishna, S.; Yan, Q. MS₂ (M = Co and Ni) hollow spheres with tunable interiors for high-performance supercapacitors and photovoltaics. *Adv. Funct. Mater.* **2014**, *24*, 2155–2162. [[CrossRef](#)]
40. Li, G.C.; Liu, P.F.; Liu, R.; Liu, M.; Tao, K.; Zhu, S.R.; Wu, M.K.; Yi, F.Y.; Han, L. MOF-Derived hierarchical double-shelled NiO/ZnO hollow spheres for high-performance supercapacitors. *Dalton Trans.* **2016**, *45*, 13311–13316. [[CrossRef](#)]
41. Chen, F.; Liu, X.; Zhang, Z.; Zhang, N.; Pan, A.; Liang, S.; Ma, R. Controllable fabrication of urchin-like Co₃O₄ hollow spheres for high-performance supercapacitors and lithium-ion batteries. *Dalton Trans.* **2016**, *45*, 15155–15161. [[CrossRef](#)] [[PubMed](#)]
42. Wang, X.; Zhang, N.; Chen, X.; Liu, J.; Lu, F.; Chen, L.; Shao, G. Facile precursor conversion synthesis of hollow coral-shaped Co₃O₄ nanostructures for high-performance supercapacitors. *Colloids Surf. A* **2019**, *570*, 63–72. [[CrossRef](#)]
43. Zhang, Y.Z.; Wang, Y.; Xie, Y.L.; Cheng, T.; Lai, W.Y.; Pang, H.; Huang, W. Porous hollow Co₃O₄ with rhombic dodecahedral structures for high-performance supercapacitors. *Nanoscale* **2014**, *6*, 14354–14359. [[CrossRef](#)]
44. Xia, X.H.; Tu, J.P.; Mai, Y.J.; Wang, X.L.; Gu, C.D.; Zhao, X.B. Self-Supported hydrothermal synthesized hollow Co₃O₄ nanowire arrays with high supercapacitor capacitance. *J. Mater. Chem.* **2011**, *21*, 9319–9325. [[CrossRef](#)]
45. Wang, Y.; Zhou, T.; Jiang, K.; Da, P.; Peng, Z.; Tang, J.; Kong, B.; Cai, W.B.; Yang, Z.; Zheng, G. Reduced mesoporous Co₃O₄ nanowires as efficient water oxidation electrocatalysts and supercapacitor electrodes. *Adv. Energy Mater.* **2014**, *4*. [[CrossRef](#)]
46. Xiao, Z.; Fan, L.; Xu, B.; Zhang, S.; Kang, W.; Kang, Z.; Lin, H.; Liu, X.; Zhang, S.; Sun, D. Green fabrication of ultrathin Co₃O₄ nanosheets from metal–organic framework for robust high-rate supercapacitors. *ACS Appl. Mater. Interfaces* **2017**, *9*, 41827–41836. [[CrossRef](#)]
47. Li, J.; Hu, X.; Chen, D.; Gu, J.; Wu, Q. Facile synthesis of superthin Co₃O₄ porous nanoflake for stable electrochemical supercapacitor. *ChemistrySelect* **2018**, *3*, 9622–9626. [[CrossRef](#)]
48. Chen, H.; Lu, S.; Gong, F.; Liu, H.; Li, F. Stepwise splitting growth and pseudocapacitive properties of hierarchical three-dimensional Co₃O₄ nanobooks. *Nanomaterials* **2017**, *7*, 81. [[CrossRef](#)]
49. Gou, W.; Zhou, X.; Li, J.; Ma, Y. Nanoporous Co₃O₄ plates as highly electroactive materials for electrochemical energy storage. *Mater. Lett.* **2016**, *180*, 207–211. [[CrossRef](#)]
50. Kumar, M.; Subramania, A.; Balakrishnan, K. Preparation of electrospun Co₃O₄ nanofibers as electrode material for high performance asymmetric supercapacitors. *Electrochim. Acta* **2014**, *149*, 152–158. [[CrossRef](#)]
51. Zheng, Y.; Li, Z.; Xu, J.; Wang, T.; Liu, X.; Duan, X.; Ma, Y.; Zhou, Y.; Pei, C. Multi-Channeled hierarchical porous carbon incorporated Co₃O₄ nanopillar arrays as 3D binder-free electrode for high performance supercapacitors. *Nano Energy* **2016**, *20*, 94–107. [[CrossRef](#)]
52. Chen, H.; Wang, J.; Liao, F.; Han, X.; Zhang, Y.; Xu, C.; Gao, L. Uniform and porous Mn-doped Co₃O₄ microspheres: Solvothermal synthesis and their superior supercapacitor performances. *Ceram. Int.* **2019**, *45*, 11876–11882. [[CrossRef](#)]
53. Wang, J.; Zhang, X.; Wei, Q.; Lv, H.; Tian, Y.; Tong, Z.; Liu, X.; Hao, J.; Qu, H.; Zhao, J.; et al. 3D self-supported nanopine forest-like Co₃O₄@CoMoO₄ core–shell architectures for high-energy solid state supercapacitors. *Nano Energy* **2016**, *19*, 222–233.
54. Hu, Q.; Gu, Z.; Zheng, X.; Zhang, X. Three-Dimensional Co₃O₄@ NiO hierarchical nanowire arrays for solid-state symmetric supercapacitor with enhanced electrochemical performances. *Chem. Eng. J.* **2016**, *304*, 223–231. [[CrossRef](#)]

55. Bai, X.; Liu, Q.; Liu, J.; Zhang, H.; Li, Z.; Jing, X.; Liu, P.; Wang, J.; Li, R. Hierarchical $\text{Co}_3\text{O}_4@\text{Ni}(\text{OH})_2$ core-shell nanosheet arrays for isolated all-solid state supercapacitor electrodes with superior electrochemical performance. *Chem. Eng. J.* **2017**, *315*, 35–45. [[CrossRef](#)]
56. Bao, L.; Li, T.; Chen, S.; Peng, C.; Li, L.; Xu, Q.; Chen, Y.; Ou, E.; Xu, W. 3D graphene frameworks/ Co_3O_4 composites electrode for high-performance supercapacitor and enzymeless glucose detection. *Small* **2017**, *13*. [[CrossRef](#)]
57. Yin, D.; Huang, G.; Sun, Q.; Li, Q.; Wang, X.; Yuan, D.; Wang, C.; Wang, L. RGO/ Co_3O_4 composites prepared using GO-MOFs as precursor for advanced lithium-ion batteries and supercapacitors electrodes. *Electrochim. Acta* **2016**, *215*, 410–419. [[CrossRef](#)]
58. Wang, H.; Ren, Q.; Brett, D.J.; He, G.; Wang, R.; Key, J.; Ji, S. Double-Shelled tremella-like $\text{NiO}@\text{Co}_3\text{O}_4@\text{MnO}_2$ as a high-performance cathode material for alkaline supercapacitors. *J. Power Sources* **2017**, *343*, 76–82. [[CrossRef](#)]




© 2020 by the authors. Licensee MDPI, Basel, Switzerland. This article is an open access article distributed under the terms and conditions of the Creative Commons Attribution (CC BY) license (<http://creativecommons.org/licenses/by/4.0/>).

Article III

Fan, X., Ohlckers, P., & Chen, X. (2020). One-Step and Morphology-Controlled Synthesis of Ni-Co Binary Hydroxide on Nickel Foam for High-Performance Supercapacitors. *Applied Sciences*, 10(11), 3814. DOI: 10.3390/app10113814

Article

One-Step and Morphology-Controlled Synthesis of Ni-Co Binary Hydroxide on Nickel Foam for High-Performance Supercapacitors

Xiao Fan, Per Ohlckers *  and Xuyuan Chen *

Department of Microsystems, Faculty of Technology, Natural Sciences and Maritime Sciences, University of South-Eastern Norway, Campus Vestfold, Raveien 215, 3184 Borre, Norway; xiao.fan@usn.no

* Correspondence: per.ohlckers@usn.no (P.O.); xuyuan.chen@usn.no (X.C.); Tel.: +47-310-09-315 (P.O.); +47-310-09-028 (X.C.)

Received: 11 April 2020; Accepted: 29 May 2020; Published: 30 May 2020



Abstract: Ni-Co binary hydroxide grown on nickel foam was synthesized through a facile one-step process for pseudocapacitive electrode application. The morphology of the fabricated binary hydroxide, evolving from nanosheet to nanowire, was highly controllable by tuning the Ni:Co ratio. In systematical electrochemical measurements, the prepared binary material on nickel foam could be employed as a binder-free working electrode directly. The optimal composition obtained at the Ni:Co ratio of 5:5 in integrated nanosheet/nanowire geometry exhibited high specific capacitances of 2807 and 2222 F/g at current densities of 1 and 20 A/g, equivalent to excellent rate capability. The capacitance loss was 19.8% after 2000 cycles, demonstrating good long-term cyclic stability. The outstanding supercapacitors behaviors benefited from unique structure and synergistic contributions, indicating the great potential of the obtained binary hydroxide electrode for high-performance energy storage devices.

Keywords: Ni-Co binary hydroxide; one-step; controllable morphology; binder-free; supercapacitors; synergistic contributions

1. Introduction

The enormously increasing energy requirements and the limited availability of energy sources motivate the development of efficient and safe energy storage devices [1,2]. Supercapacitors, as next-generation high-performance energy storage devices, significantly make up the shortfall of conventional physical capacitors and batteries, and are extremely suitable for superior power density and high charge/discharge rate required applications [3–5], such as electrical vehicles and stop-go driving models [6,7]. In addition, supercapacitors also possess an ultralong service life of up to 10,000 cycles and excellent operating temperature adaptability from $-40\text{ }^{\circ}\text{C}$ to $+70\text{ }^{\circ}\text{C}$ [8,9]. Accordingly, supercapacitors have sparked extensive interest in recent years. Two types of supercapacitors, divided by energy storage mechanisms, are termed as electric double-layer capacitors and pseudocapacitors, respectively [10,11]. Currently, the electric double-layer capacitors, by operating reversible ions' adsorption/desorption to store energy, suffer from lower specific capacitance [12,13], which fails to meet the ever-growing demand. In contrast, pseudocapacitors contribute to higher specific capacitance by reversible faradaic redox reactions [14,15] and have become the research hotspot in supercapacitors fields in past decade.

Among various transition metal oxides/hydroxides for the electrode materials of pseudocapacitors, $\text{Ni}(\text{OH})_2$ and $\text{Co}(\text{OH})_2$, in virtues of definite redox transitions, superior theoretical specific capacitances (ca. 3750 F/g for $\text{Ni}(\text{OH})_2$ and ca. 3460 F/g for $\text{Co}(\text{OH})_2$), earth-abundant resources, and environmental friendliness [16,17], have attracted much attentions. For instance, the $\text{Ni}(\text{OH})_2$ microspheres,

synthesized by Du et al., presented the specific capacitance of 1280.9 F/g at current density of 0.5 A/g [18]. Yin et al. reported the Co(OH)₂ nanoflakes delivering 1636 F/g at 0.5 A/g [19]. However, the achieved specific capacitances by single Ni(OH)₂ or Co(OH)₂ so far are far lower than the theoretical values, consequently hampering their practical use. To address the issue, novel binary Ni-Co hydroxide was studied and has been shown to outperform the corresponding single hydroxide, owing to unparalleled advantages, such as stronger layered orientation, reduced resistance, increased active sites generated by valence interchange or charge hopping between cations, synergistic redox reaction, moderate redox potential, and decreased redox peak potential difference [20–28]. Unfortunately, even though numerous efforts were devoted, the specific capacitances up to now are still unsatisfied, which are mainly caused by undesirable morphology [29–33] and involved binders [34–38]. Moreover, with respect to high rate capability, cycling stability, good mass loading, and facile method, previous progress to date rarely shows all of these characteristics. For example, the Ni-Co double hydroxide nanosheets prepared by Chen et al. reached ultrahigh 2682 F/g at 3 A/g, but the capacitance loss was more than 35% at 20 A/g [39]. Similarly, the Ni-Co double hydroxides microspheres by Tao and co-workers displayed 2275.5 F/g at 1 A/g, nevertheless the capacitance sharply faded to 1007.8 F/g at 25 A/g [40]. Besides, Zhang et al. developed flower-like Ni-Co binary hydroxides, in which only 73.8% capacitance could be maintained after 3000 cycles [41]. Yang and co-workers fabricated Ni-Co hydroxide nanostructures, which demonstrated 1760 and 1468 F/g at 1 and 20 A/g, as well as 87.3% capacitance retention after 2000 cycles, whereas remarkable criteria were obtained at an exaggerated low mass loading of 0.23 mg/cm² [42]. In addition, the multi-step and complex routes employed in certain cases further hindered their commercial application. Hence, it is still a challenge to get the utmost out of the binary system for the application of high-performance supercapacitors with promising commercial prospect.

In this paper, we report a novel approach to directly grow Ni-Co binary hydroxides at different Ni:Co ratios on nickel foam (NF), a substrate with a series of fulfilling features, such as polyporous structure, high surface area, and low resistivity. The optimal electrode has numerous advantages, such as being binder-free, having integrated geometry, moderate redox potential, overlapping redox peaks, and feasible synergistic effect, therefore displaying outstanding overall supercapacitor performances. The simple one-step method further manifests the bright outlook of this study in both research and commercial fields.

2. Materials and Methods

2.1. Preparation of Ni-Co Binary Hydroxide on Nickel Foam

Ni-Co binary hydroxide on nickel foam was fabricated by a facile one-step solvothermal reaction. Nickel foam (1 cm × 1 cm) was pretreated with 6 M HCl, deionized water, and ethanol, sequentially. Then, a precursor solution containing the desired molar mixture of Ni(NO₃)₂·6H₂O, Co(NO₃)₂·6H₂O (the feeding concentration ratios of Ni²⁺:Co²⁺ were 9:1, 7:3, 5:5, 3:7, and 1:9, respectively, and total molar of cations was 5 mmol), 2 mmol NH₄F, 6 mmol CO(NH₂)₂, and 50 mL deionized water was prepared. After vigorous stirring for 10 min, the solution and nickel foam were transferred to a Teflon-lined stainless-steel autoclave and maintained at 120 °C for 8 h. The final products were rinsed with deionized water after cooling down to room temperature naturally. For convenient clarification, the samples were labeled as Ni_{1-x}Co_x(OH)₂ (x = 0.1, 0.3, 0.5, 0.7, and 0.9). The loading mass on the nickel foam was approximately 1.5 mg/cm².

2.2. Material Characterizations

The surface morphological feature was characterized by a scanning electron microscope (SEM, SU8230, Hitachi, Tokyo, Japan) operated at 10 kV. The crystalline structure was investigated via X-ray powder diffraction (XRD, EQUINOX 1000, ThermoFisher, Waltham, America) with Cu K α radiation (λ = 0.15406 nm). X-ray photoelectron spectroscopy (XPS, ESCALAB 250Xi, ThermoFisher, Waltham, America) under monochromatized Al K α excitation was adopted to reveal the chemical status.

2.3. Electrochemical Measurements

The electrochemical performances were evaluated throughout cyclic voltammetry (CV), galvanostatic charge/discharge (GCD), electrochemical impedance spectroscopy (EIS), and long-term cycling on an electrochemical workstation (IM6, Zahner, Kronach, Germany) at room temperature. The configuration, potential window, and electrolyte were set as a three-electrode system, 0–0.5 V and 2 M KOH, respectively. The Ni_{1-x}Co_x(OH)₂/NF served as a working electrode directly while Pt net and Ag/AgCl (3.5 M KCl) were employed as a counter electrode and reference electrode. The measured ranges of scan rate for CV, current density for GCD, and frequency for EIS were 2–50 mV/s, 1–20 A/g and 100 mHz–100 kHz, respectively. The long-term cycling was executed at a constant current density of 20 A/g for 2000 cycles.

The specific capacitance, energy density, and power density based on GCD measurement are defined as Equations (1)–(3), respectively [43]:

$$C = \frac{It}{m\Delta V}, \quad (1)$$

$$E = \frac{C\Delta V^2}{7.2}, \quad (2)$$

$$P = \frac{3.6E}{t}. \quad (3)$$

where, C (F/g) is the specific capacitance, I (A) is the discharge current, Δt (s) is the discharge time, m (g) is the mass of active material, ΔV (V) is the voltage window, E (Wh/kg) is the energy density, and P (kW/kg) is the power density.

3. Results

By controlling the initial ratio of Ni and Co in the reactants, the binary material experienced an evident morphological evolution from nanosheet to nanowire, investigated in detail by the SEM, as shown in Figure 1b–f. Figure 1a presents the bare nickel foam with a continuous porous three-dimension (3D) network. At a Ni:Co ratio of 9:1, the nanosheets were observed, as shown in Figure 1b. Partial nanosheets intersected among each other, displaying an ambiguous nanoflower-like feature. By further increasing content of Co, the morphology of the composite evolved into nanosheet completely, as shown in Figure 1c. Particularly, as more cobalt ions were devoted (intermediate Ni:Co ratio), nanowires appeared and were encapsulated around the nanosheets, as shown in Figure 1d. The constructed integrated geometry provided a large accessible surface area compared with sole nanosheet morphology. At a greater Co to Ni ratio, the nanosheet structures were replaced by uniform nanowires, as shown in Figure 1e. Finally, when Co became dominant (Ni:Co ratio of 1:9), it could be seen that sectional nanowires trended to aggregate, as depicted in Figure 1f. The distinct morphological evolution is ascribed to the competition of Ni and Co cations for hydroxide radicals [44].

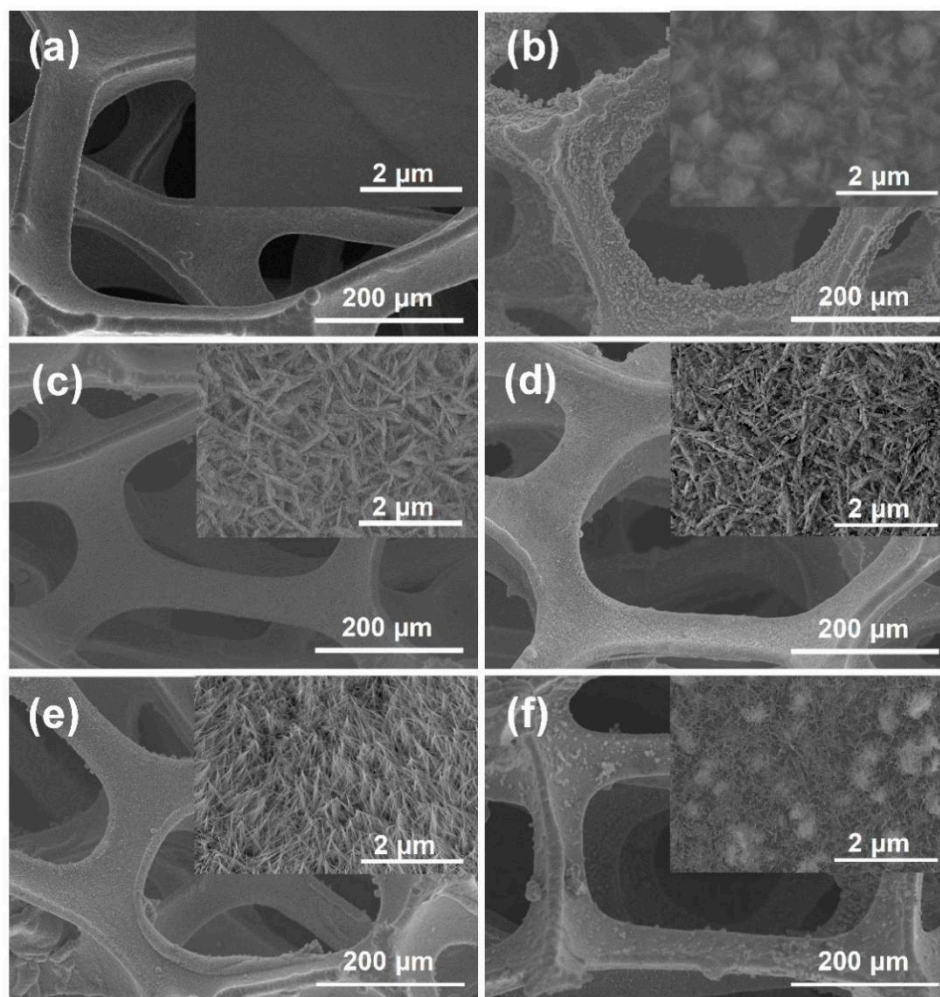


Figure 1. Scanning electron microscope (SEM) images of the samples at different Ni:Co ratios: (a) bare nickel foam; (b) 9:1; (c) 7:3; (d) 5:5; (e) 3:7; (f) 1:9.

The XRD patterns of as-prepared samples under different Ni:Co ratios are shown in Figure 2. The indexed planes of the diffraction peaks at corresponding 2θ values can be assigned to $\text{Ni}(\text{OH})_2$ (JCPDS No. 14-0117) and $\text{Co}(\text{OH})_2$ (JCPDS No. 30-0443). The analogous peak positions are believed to be caused by the similar physical and chemical characteristics of Ni and Co [45]. When a larger Co source was applied, the peak signals became weaker and a lacking of partial peaks appeared, which is ascribed to the low crystallinity of the sample [46]. The XPS was carried out to verify the element valence state of the as-synthesized material. The typical XPS survey spectrum of the sample at a Ni:Co ratio of 5:5 is depicted in Figure 3a, where C, Ni, Co, and O were visible. The C element is due to the air exposure of the sample and can be referenced to calibrate the binding energy [47,48]. In the high resolution XPS spectrum of Ni 2p, shown in Figure 3b, the peaks of Ni $2p_{3/2}$ and Ni $2p_{1/2}$ at binding energies of 855.6 and 873.5 eV (energy separation of 17.9 eV), as well as two obvious shakeup satellites (denoted as Sat.), indicate the characteristics of Ni^{2+} [49]. Figure 3c illustrates the core-level XPS spectrum of Co 2p, the peaks at binding energies of 781.4 and 796.9 eV standing for Co $2p_{3/2}$ and Co $2p_{1/2}$ (energy gap of 15.5 eV), identify Co as Co^{2+} [50,51]. The single peak located at 531.1 eV in the O 1s spectrum, shown in Figure 3d, is assigned to OH- [48,52]. Hence, it can be concluded that Ni-Co double hydroxides were successfully formed under the present experimental conditions.

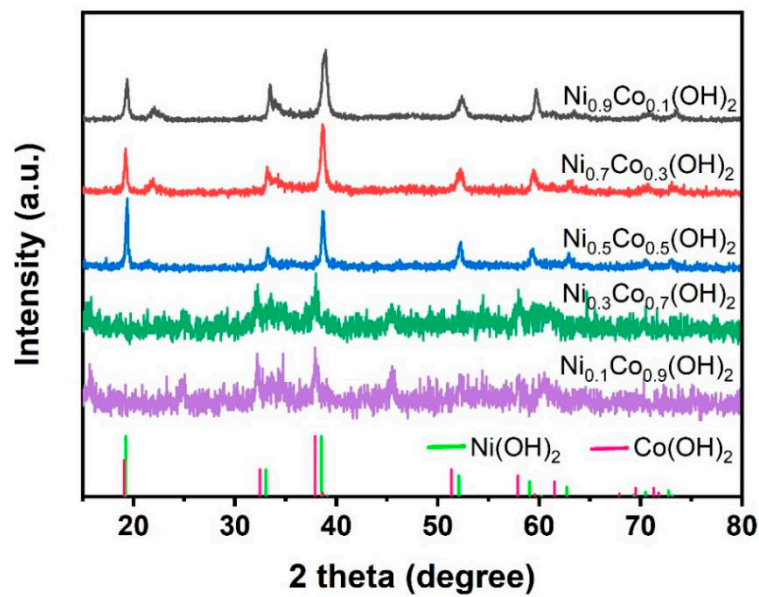


Figure 2. X-ray powder diffraction (XRD) patterns of the $\text{Ni}_{1-x}\text{Co}_x(\text{OH})_2$.

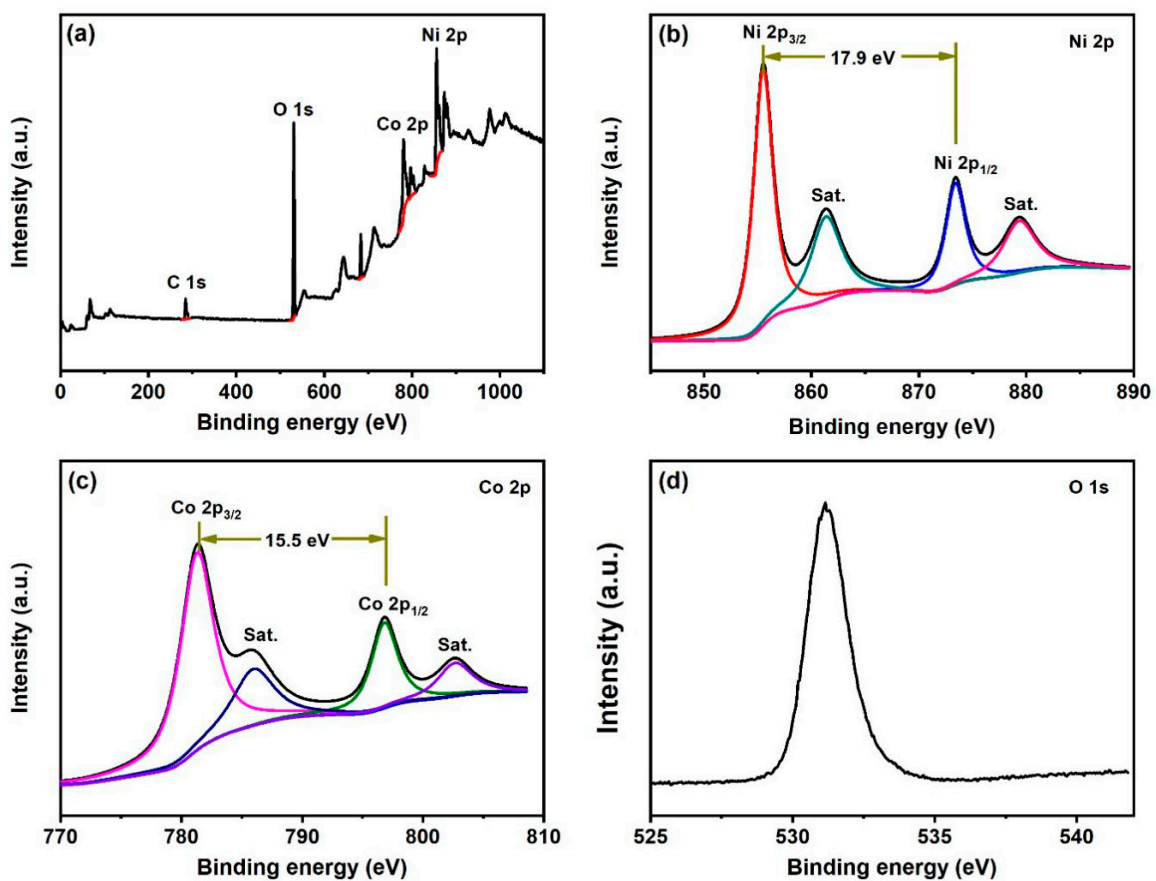
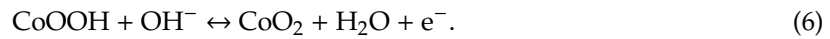
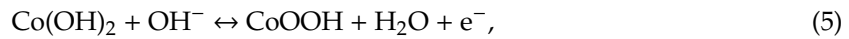
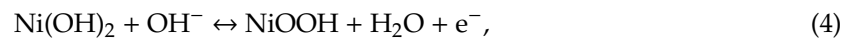


Figure 3. X-ray photoelectron spectroscopy (XPS) spectra of the $\text{Ni}_{0.5}\text{Co}_{0.5}(\text{OH})_2$: (a) survey spectrum; (b) Ni 2p; (c) Co 2p; (d) O 1s.

The CV curves were initially characterized in a potential window of 0–0.5 V (vs. Ag/AgCl) to evaluate the supercapacitor behavior of the binary materials. The $\text{Ni}_{1-x}\text{Co}_x(\text{OH})_2/\text{NF}$ was directly employed as the binder-free working electrode in a typical three-electrode configuration. The CV curves of the active materials under different Ni:Co ratios, measured at a scan rate of 2 mV/s, are shown

in Figure 4a. All CV curves present a distinct pair of peaks, which involves three reversible faradaic redox processes, expressed as Equations (4)–(6) [41]:



The merged and indistinguishable redox peaks reveal the mixed uniformity of Ni and Co in the binary hydroxides [53]. Further, the peaks in anodic sweep move to lower potential when Co content increases, because the potential of Co transition is lower than that of Ni. In other words, the oxidation peak corresponding to Ni is closer to the voltage window limit [44,54]. The potential window is mainly determined according to the range where effective faradaic reactions occur. At a defined scan rate, the specific capacitance is correlated with the curvilinear integrated area positively based on CV evaluation [43]. Clearly, the maximum area of the CV curve is achieved at a Ni:Co ratio of 5:5. Figure 4b displays the CV curves of the $\text{Ni}_{0.5}\text{Co}_{0.5}(\text{OH})_2$ electrode, tested at scan rates of 2, 5, 10, 20, and 50 mV/s. The coupled redox peaks in the CV curves shift positively or negatively with increased scan rates. The classical phenomenon also confirms the pseudocapacitive property of the obtained material [55]. Besides, the relationship of peak currents and the square root of the scan rates delivers a linear response with a steep slope, as described in the inset of Figure 4b. The distortion of the CV curves, obtained from 2 to 50 mV/s, is almost negligible. The characteristics above illustrate the excellent reversibility and rapid response of the $\text{Ni}_{0.5}\text{Co}_{0.5}(\text{OH})_2$ electrode, promisingly leading to a desirable rate capability [56].

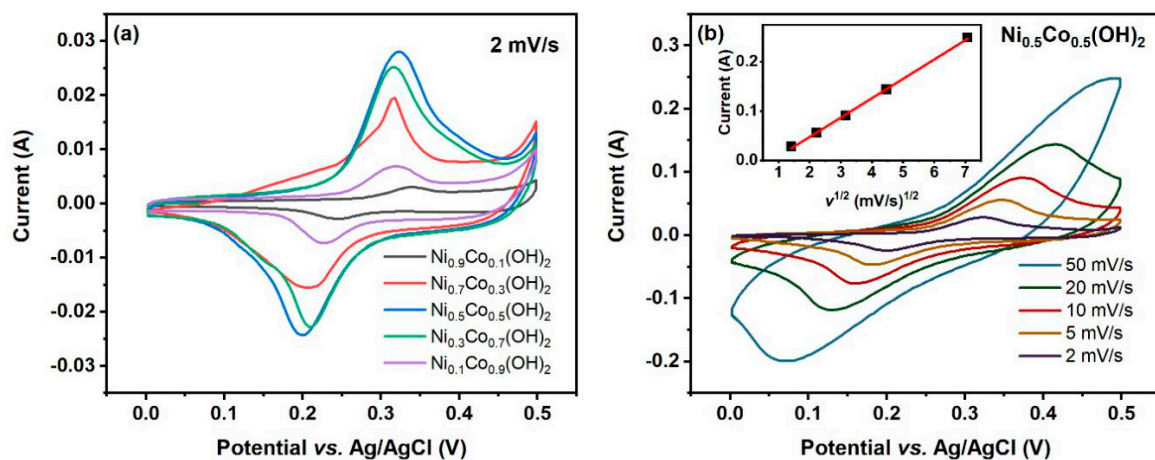


Figure 4. (a) Cyclic voltammetry (CV) curves of the $\text{Ni}_{1-x}\text{Co}_x(\text{OH})_2$ electrodes at scan rate of 2 mV/s. (b) CV curves of the $\text{Ni}_{0.5}\text{Co}_{0.5}(\text{OH})_2$ electrode at scan rates from 2 to 50 mV/s.

The GCD tests through the same three-electrode system were conducted on the binary hydroxide electrodes to demonstrate the electrochemical properties further. The GCD curves of the $\text{Ni}_{1-x}\text{Co}_x(\text{OH})_2$ electrodes, measured at current densities of 1, 2, 5, 10, and 20 A/g in a potential range of 0–0.5 V (vs. Ag/AgCl), are shown in Figure 5a–e, respectively. As expected, all non-linear curves deliver well-defined plateaus, arising from redox reactions, also suggesting the pseudocapacitive features of the synthesized materials [54]. What is more, the plateaus are still dimly visible, even at a current density of 20 A/g, which implies a slight decay of the specific capacitance at high current density could possibly be reached. In GCD measurements, the specific capacitance is proportional to the discharge time [43]. Figure 5f intuitively depicts that the proposed $\text{Ni}_{0.5}\text{Co}_{0.5}(\text{OH})_2$ electrode takes the longest time to complete one discharge process, which is in good agreement with the CV results exhibited in Figure 4a.

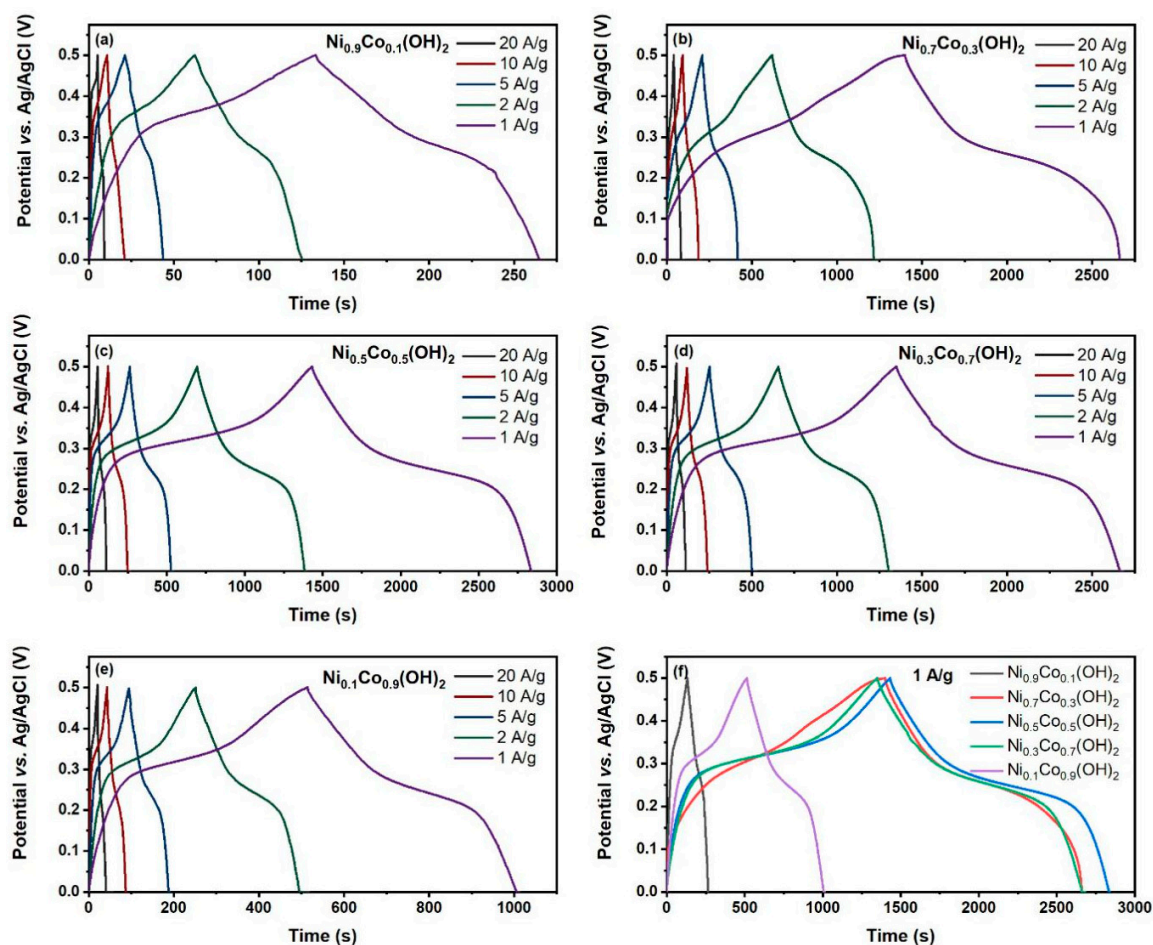


Figure 5. Galvanostatic charge/discharge (GCD) curves at current densities from 1 to 20 A/g: (a) $\text{Ni}_{0.9}\text{Co}_{0.1}(\text{OH})_2$; (b) $\text{Ni}_{0.7}\text{Co}_{0.3}(\text{OH})_2$; (c) $\text{Ni}_{0.5}\text{Co}_{0.5}(\text{OH})_2$; (d) $\text{Ni}_{0.3}\text{Co}_{0.7}(\text{OH})_2$; (e) $\text{Ni}_{0.1}\text{Co}_{0.9}(\text{OH})_2$; (f) GCD curves of the $\text{Ni}_{1-x}\text{Co}_x(\text{OH})_2$ electrodes at current density of 1 A/g.

The specific capacitances based on the GCD tests were determined according to Equation (1). The calculated values as a function of current densities for all as-prepared electrodes are plotted in Figure 6a. All of the function graphs show a similar attenuation tendency, namely, the produced specific capacitances decrease accompanied by the boost of current densities. Admittedly, the unsatisfying fade is inevitable, owing to the limited diffusion of electrolyte ions (OH^- in this work). Briefly, in comparison with low current density, the time for OH^- transfer is inadequate at high current density, leading to the fact that involved active material in redox reactions is also insufficient [57]. The specific capacitance becomes greater with the content of Co in the binary hydroxide until the intermediate ratio. Beyond this ratio, a decrease in capacitive performance appears. This phenomenon is consistent with previous literature [54,58–61]. The $\text{Ni}_{0.5}\text{Co}_{0.5}(\text{OH})_2$ electrode delivers high specific capacitances of 2807, 2751, 2622, 2444, and 2222 F/g at current densities of 1, 2, 5, 10 and 20 A/g, which is attributed to the integrated nanosheet/nanowire geometry and broadened redox behavior at a Ni:Co ratio of 5:5. The specific capacitance, reached as an important parameter for supercapacitors, manifests in the great application prospect of the obtained $\text{Ni}_{0.5}\text{Co}_{0.5}(\text{OH})_2$ electrode. Among five composites, the $\text{Ni}_{0.9}\text{Co}_{0.1}(\text{OH})_2$ and $\text{Ni}_{0.1}\text{Co}_{0.9}(\text{OH})_2$ electrodes express large differences in specific capacitances compared with the other three samples. The poor ability under the same measured conditions is mainly due to the aggregation of material, which deteriorates the accessibility of electrolyte ions in electroactive material. Furthermore, the $\text{Ni}_{0.5}\text{Co}_{0.5}(\text{OH})_2$ electrode still maintains a specific capacitance of 79.2%, even when the current density increases 20-times more than the initial value, representing an excellent rate capability. What is noteworthy is that the $\text{Ni}_{0.3}\text{Co}_{0.7}(\text{OH})_2$ electrode offers a slightly higher rate capability of 82% (2624 and

2151 F/g at 1 and 20 A/g) than that of the $\text{Ni}_{0.5}\text{Co}_{0.5}(\text{OH})_2$ sample, which highlights the advantage of nanowire morphology as a one-dimension (1D) geometry, which can better guarantee effective ion diffusion and electron transportation at high current density [44,62]. Based on Equations (2) and (3), the Ragone plots of the samples were obtained to further illustrate the electrochemical properties, as exhibited in Figure 6b. The $\text{Ni}_{0.5}\text{Co}_{0.5}(\text{OH})_2$ sample shows energy densities of 97.5, 95.5, 91, 84.9 and 77.2 Wh/kg at power densities of 0.25, 0.5, 1.25, 2.5 and 5 kW/kg, respectively.

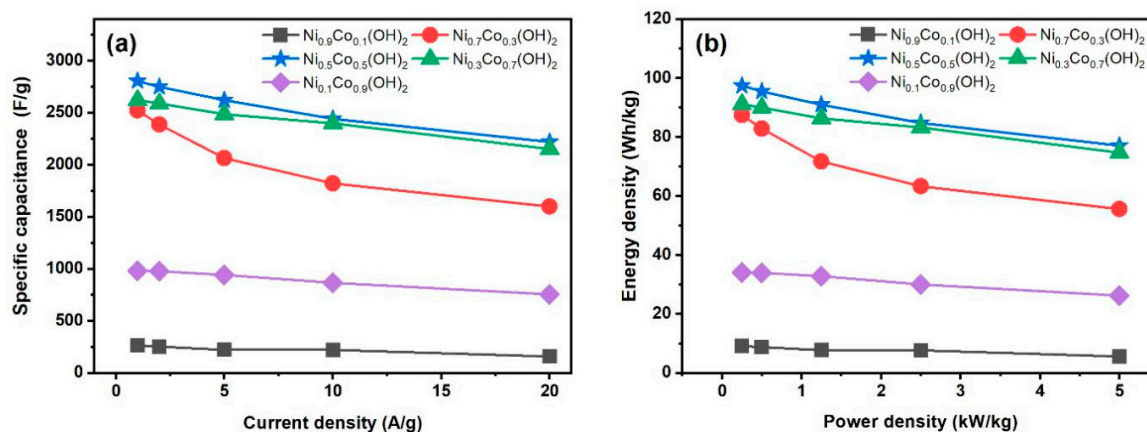


Figure 6. (a) Specific capacitances as a function of current densities and (b) Ragone plots of the $\text{Ni}_{1-x}\text{Co}_x(\text{OH})_2$ samples.

The EIS studies over the frequency range of 100 mHz to 100 kHz in 2 M KOH were carried out on $\text{Ni}_{0.7}\text{Co}_{0.3}(\text{OH})_2$, $\text{Ni}_{0.5}\text{Co}_{0.5}(\text{OH})_2$, and $\text{Ni}_{0.3}\text{Co}_{0.7}(\text{OH})_2$ as optimized electrodes. Figure 7a records the typical Nyquist plots. Generally, the intrinsic resistances (electrolyte and material) and contact resistances (electrolyte/material and material/current collector) are summarized as R_s , which is valued from the intersection of the EIS plot and real axis. Figure 7b illustrates the high frequency in an enlarged view, in which the semicircle corresponds to the charge transfer resistance (R_{ct}). The straight line at the low frequency portion represents the ion diffusion in the electrolyte, arising in a Warburg element (W) [61,63,64]. The $\text{Ni}_{0.3}\text{Co}_{0.7}(\text{OH})_2$ electrode delivers the smallest diameter (expressing lowest R_{ct}) and largest slope (suggesting fastest ion diffusion), which is consistent with its outstanding rate performance. The highest specific capacitance produced by the $\text{Ni}_{0.5}\text{Co}_{0.5}(\text{OH})_2$ electrode is due to: (1) the union of Ni and Co at ratio of 5:5 generating most electroactive sites from the feasible interaction of the valence state electron [54]; (2) the R_s value of the $\text{Ni}_{0.5}\text{Co}_{0.5}(\text{OH})_2$ electrode being lower than the others. Overall, the EIS spectra well coincide with the aforementioned CV and GCD results. Figure 7c presents the fitting equivalent circuit, where C_{dl} and C_{ps} account for double-layer capacitance and pseudocapacitance, respectively.

The long-term electrochemical stability was assessed via repetitive GCD tests at a constant current density of 20 A/g. Figure 8 displays the capacitance retentions and coulombic efficiencies of the $\text{Ni}_{0.5}\text{Co}_{0.5}(\text{OH})_2$ electrode as a function of the cycle numbers (the inset depicts the GCD curves of the last 10 cycles). The coulombic efficiency is calculated based on Equation (7) [63]:

$$\eta = \frac{t_d}{t_c}, \quad (7)$$

where, η (%) is the coulombic efficiency, t_d (s) is the discharge time, and t_c (s) is the charge time. As recorded in Figure 8, the deduced capacitance retentions gradually decreased at first, and after approximately 1000 cycles remained nearly constant. Impressively, even after 2000 cycles, the $\text{Ni}_{0.5}\text{Co}_{0.5}(\text{OH})_2$ electrode still reached 80.2% of its initial specific capacitance and its high coulombic efficiency exceeded 90%. The capacitance loss after long-term cycling is inevitable, which is likely attributed to several reasons, (e.g., the presence of irreversible redox reactions, damage to the electrode,

or impurities in the electrolyte) [65]. The remarkable durability performance of the $\text{Ni}_{0.5}\text{Co}_{0.5}(\text{OH})_2$ electrode is pivotal for potential commercial application. In contrast, the cycling stability of the $\text{Ni}_{0.3}\text{Co}_{0.7}(\text{OH})_2$ electrode is poor (capacitance retention of 62.1% after 2000 cycles), possibly since partial nanowires were not attached to the nickel foam tightly enough, giving rise to low material utilization for capacitance.

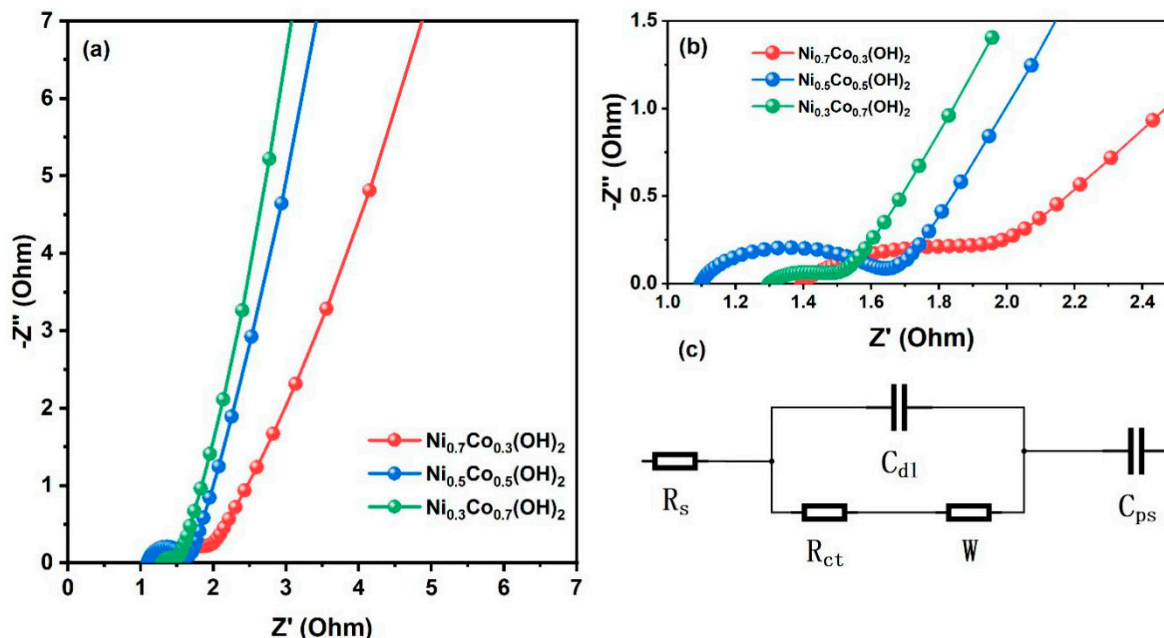


Figure 7. (a) Electrochemical impedance spectroscopy (EIS) plots of the $\text{Ni}_{0.7}\text{Co}_{0.3}(\text{OH})_2$, $\text{Ni}_{0.5}\text{Co}_{0.5}(\text{OH})_2$, and $\text{Ni}_{0.3}\text{Co}_{0.7}(\text{OH})_2$ electrodes. (b) Enlarged view of the high frequency region. (c) Fitting equivalent circuit.

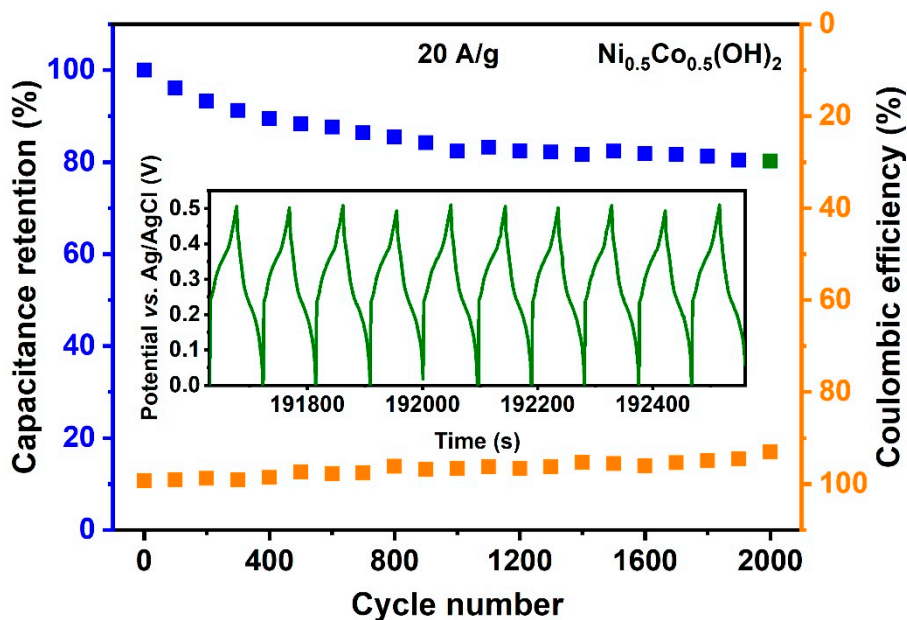


Figure 8. Cycling performance and coulombic efficiency of the $\text{Ni}_{0.5}\text{Co}_{0.5}(\text{OH})_2$ electrode.

4. Discussion

To summarize, the $\text{Ni}_{1-x}\text{Co}_x(\text{OH})_2$ electrode possessed the best overall supercapacitor performance when x equals 0.5 was investigated in terms of specific capacitance, rate capability, and cycling stability. These superior behaviors are attributed to the common advantages of the binary system and the unique

merits of $\text{Ni}_{0.5}\text{Co}_{0.5}(\text{OH})_2$. Firstly, the synthesized material is grown directly onto the surface of nickel foam rather than by virtue of a binder, affording an intimate electric contact. Secondly, the oxidation peak of Ni moves towards comparatively lower potential by introducing Co, which avoids possible solvent oxidation [44]. Thirdly, the overlapping redox peaks broaden the redox features and improve redox response. In addition, the integrated nanosheet/nanowire architecture of $\text{Ni}_{0.5}\text{Co}_{0.5}(\text{OH})_2$ increases the active sites for redox reaction and pathways for electron transportation. On the other hand, the $\text{Ni}_{0.5}\text{Co}_{0.5}(\text{OH})_2$ electrode delivers the lowest intrinsic and contact resistances (i.e., R_s). Moreover, the $\text{Ni}_{0.5}\text{Co}_{0.5}(\text{OH})_2$ possibly possesses the most electroactive sites generated by valence interchange or charge hopping between cations [58]. The specific capacitance of the $\text{Ni}_{0.5}\text{Co}_{0.5}(\text{OH})_2$ electrode is even higher than those of some hybrid materials [66–68]. Apart from remarkable specific capacitance, the high rate capability of 79.2% at current density of 20 A/g and the slight capacitance decay of 19.8% after 2000 cycles are also satisfied.

5. Conclusions

In summary, the Ni-Co binary hydroxide system was fabricated by a facile one-step hydrothermal reaction. By tailoring the cation ratio in preparation, the morphology of the binary system evolved from nanosheet to nanowire straightforwardly, as a consequence, giving rise to different supercapacitor behaviors. The optimal electrode achieved at a Ni:Co ratio of 5:5 exhibited a prominent specific capacitance of 2807 F/g at a current density of 1 A/g (based on active material) as well as outstanding rate (79.2% capacitance retention at 20 A/g) and cycling (80.2% capacitance retention after 2000 cycles) performances. The remarkable criteria and the environmentally friendly method manifest great prospects of the obtained $\text{Ni}_{0.5}\text{Co}_{0.5}(\text{OH})_2$ electrode for commercial application in high-performance supercapacitors. Furthermore, this novel approach is also promisingly adopted to develop other binary systems using different electrochemically active metal hydroxides for wide applications not only in supercapacitors, but also in catalysts, sensors, and so forth.

Author Contributions: Conceptualization, X.C. and P.O.; methodology, X.F., P.O., and X.C.; software, X.F.; validation, X.F., P.O., and X.C.; formal analysis, X.F.; investigation, X.C. and P.O.; resources, X.C. and P.O.; data curation, X.F., P.O., and X.C.; writing—original draft preparation, X.F.; writing—review and editing, X.C. and P.O.; visualization, X.F., P.O., and X.C.; supervision, X.C. and P.O.; project administration, X.C. and P.O.; funding acquisition, X.C. All authors have read and agreed to the published version of the manuscript.

Funding: This research was funded by the Research Council of Norway (RCN, grant number 221860/F60) and the Norwegian Micro- and Nano-Fabrication Facility (NorFab, project number 245963). Xiao Fan was financially supported by the China Scholarship Council (CSC, grant number 201506930018).

Acknowledgments: The authors gratefully acknowledge lab engineers Zekija Ramic, Thomas Martinsen, Tayyib Muhammad, Anh Tuan Thai Nguyen, and Birgitte Kasin Hønsvall for their kind help associated with this work. The authors also specially thank Einar Halvorsen, Pai Lu, and Yongjiao Sun for their critical suggestions.

Conflicts of Interest: The authors declare no conflict of interest.

References

1. Wang, L.; Han, Y.; Feng, X.; Zhou, J.; Qi, P.; Wang, B. Metal–organic frameworks for energy storage: Batteries and supercapacitors. *Coord. Chem. Rev.* **2016**, *307*, 361–381. [[CrossRef](#)]
2. González, A.; Goikolea, E.; Barrena, J.A.; Mysyk, R. Review on supercapacitors: Technologies and materials. *Renew. Sustain. Energy Rev.* **2016**, *58*, 1189–1206. [[CrossRef](#)]
3. Dubal, D.P.; Ayyad, O.; Ruiz, V.; Gomez-Romero, P. Hybrid energy storage: The merging of battery and supercapacitor chemistries. *Chem. Soc. Rev.* **2015**, *44*, 1777–1790. [[CrossRef](#)] [[PubMed](#)]
4. Zhang, L.; Hu, X.; Wang, Z.; Sun, F.; Dorrell, D.G. A review of supercapacitor modeling, estimation, and applications: A control/management perspective. *Renew. Sustain. Energy Rev.* **2018**, *81*, 1868–1878. [[CrossRef](#)]
5. Conway, B.E. Transition from “supercapacitor” to “battery” behavior in electrochemical energy storage. *J. Electrochem. Soc.* **1991**, *138*, 1539. [[CrossRef](#)]

6. Castaings, A.; Lhomme, W.; Trigui, R.; Bouscayrol, A. Comparison of energy management strategies of a battery/supercapacitors system for electric vehicle under real-time constraints. *Appl. Energy* **2016**, *163*, 190–200. [[CrossRef](#)]
7. Faggioli, E.; Rena, P.; Danel, V.; Andrieu, X.; Mallant, R.; Kahlen, H. Supercapacitors for the energy management of electric vehicles. *J. Power Sources* **1999**, *84*, 261–269. [[CrossRef](#)]
8. Tang, Z.; Tang, C.H.; Gong, H. A high energy density asymmetric supercapacitor from nano-architected Ni(OH)₂/Carbon nanotube electrodes. *Adv. Funct. Mater.* **2012**, *22*, 1272–1278. [[CrossRef](#)]
9. Kötz, R.; Hahn, M.; Gallay, R. Temperature behavior and impedance fundamentals of supercapacitors. *J. Power Sources* **2006**, *154*, 550–555. [[CrossRef](#)]
10. Kang, J.; Zhang, S.; Zhang, Z. Three-dimensional binder-free nanoarchitectures for advanced pseudocapacitors. *Adv. Mater.* **2017**, *29*, 1700515. [[CrossRef](#)]
11. Salanne, M.; Rotenberg, B.; Naoi, K.; Kaneko, K.; Taberna, P.L.; Grey, C.P.; Dunn, B.; Simon, P. Efficient storage mechanisms for building better supercapacitors. *Nat. Energy* **2016**, *1*, 1–10. [[CrossRef](#)]
12. Ke, Q.; Wang, J. Graphene-based materials for supercapacitor electrodes—A review. *J. Mater.* **2016**, *2*, 37–54. [[CrossRef](#)]
13. Borenstein, A.; Hanna, O.; Attias, R.; Luski, S.; Brousse, T.; Aurbach, D. Carbon-based composite materials for supercapacitor electrodes: A review. *J. Mater. Chem. A* **2017**, *5*, 12653–12672. [[CrossRef](#)]
14. Lu, Q.; Chen, J.G.; Xiao, J.Q. Nanostructured electrodes for high-performance pseudocapacitors. *Angew. Chem. Int. Ed.* **2013**, *52*, 1882–1889. [[CrossRef](#)] [[PubMed](#)]
15. Wang, C.; Xu, J.; Yuen, M.F.; Zhang, J.; Li, Y.; Chen, X.; Zhang, W. Hierarchical composite electrodes of nickel oxide nanoflake 3D graphene for high-performance pseudocapacitors. *Adv. Funct. Mater.* **2014**, *24*, 6372–6380. [[CrossRef](#)]
16. Chen, X.; Zhang, F.; Yang, Z.; Huang, S. One-pot hydrothermal synthesis of reduced graphene oxide/carbon nanotube/ α -Ni(OH)₂ composites for high performance electrochemical supercapacitor. *J. Power Sources* **2013**, *243*, 555–561. [[CrossRef](#)]
17. Zhao, C.; Wang, X.; Wang, S.; Wang, Y.; Zhao, Y.; Zheng, W. Synthesis of Co(OH)₂/graphene/Ni foam nano-electrodes with excellent pseudocapacitive behavior and high cycling stability for supercapacitors. *Int. J. Hydrog. Energy* **2012**, *37*, 11846–11852. [[CrossRef](#)]
18. Du, H.; Wang, Y.; Yuan, H.; Jiao, L. Facile synthesis and high capacitive performance of 3D hierarchical Ni(OH)₂ microspheres. *Electrochim. Acta* **2016**, *196*, 84–91. [[CrossRef](#)]
19. Yin, T.; Zhang, W.; Yin, Y.; Yan, Y.; Zhan, K.; Yang, J.; Zhao, B. Co(OH)₂ nanoflakes grown on 3D graphene foam as a binder-free hybrid electrode for high-performance supercapacitors. *J. Mater. Sci. Mater. Electron.* **2017**, *28*, 7884–7891. [[CrossRef](#)]
20. Nguyen, T.; Boudard, M.; Carmezim, M.J.; Montemor, M.F. Ni_xCo_{1-x}(OH)₂ nanosheets on carbon nanofoam paper as high areal capacity electrodes for hybrid supercapacitors. *Energy* **2017**, *126*, 208–216. [[CrossRef](#)]
21. Xiong, G.; He, P.; Wang, D.; Zhang, Q.; Chen, T.; Fisher, T.S. Hierarchical Ni–Co Hydroxide Petals on Mechanically Robust Graphene Petal Foam for High-Energy Asymmetric Supercapacitors. *Adv. Funct. Mater.* **2016**, *26*, 5460–5470. [[CrossRef](#)]
22. Liu, X.; Ma, R.; Bando, Y.; Sasaki, T. A general strategy to layered transition-metal hydroxide nanocones: Tuning the composition for high electrochemical performance. *Adv. Mater.* **2012**, *24*, 2148–2153. [[CrossRef](#)] [[PubMed](#)]
23. Armstrong, R.D.; Charles, E.A. Some effects of cobalt hydroxide upon the electrochemical behaviour of nickel hydroxide electrodes. *J. Power Sources* **1989**, *25*, 89–97. [[CrossRef](#)]
24. Nguyen, T.; Boudard, M.; Carmezim, M.J.; Montemor, M.F. Layered Ni (OH)₂-Co (OH)₂ films prepared by electrodeposition as charge storage electrodes for hybrid supercapacitors. *Sci. Rep.* **2017**, *7*, 1–10. [[CrossRef](#)]
25. Chen, J.C.; Hsu, C.T.; Hu, C.C. Superior capacitive performances of binary nickel–cobalt hydroxide nanonetwork prepared by cathodic deposition. *J. Power Sources* **2014**, *253*, 205–213. [[CrossRef](#)]
26. Wang, C.; Zhang, X.; Xu, Z.; Sun, X.; Ma, Y. Ethylene glycol intercalated cobalt/nickel layered double hydroxide nanosheet assemblies with ultrahigh specific capacitance: Structural design and green synthesis for advanced electrochemical storage. *ACS Appl. Mater. Interfaces* **2015**, *7*, 19601–19610. [[CrossRef](#)]
27. Hamal, E.K.; Toroker, M.C. The Effect of Fe and Co Additions on the Efficiency of NiOOH Catalyst Under Strain. *ChemCatChem* **2020**, *12*, 2801–2806. [[CrossRef](#)]

28. Hwang, M.; Kang, J.; Seong, K.D.; Kim, D.K.; Jin, X.; Antink, W.H.; Lee, C.; Piao, Y. Ni-Co hydroxide nanoneedles embedded in graphene hydrogel as a binder-free electrode for high-performance asymmetric supercapacitor. *Electrochim. Acta* **2018**, *270*, 156–164. [[CrossRef](#)]
29. Salunkhe, R.R.; Jang, K.; Lee, S.W.; Ahn, H. Aligned nickel-cobalt hydroxide nanorod arrays for electrochemical pseudocapacitor applications. *RSC Adv.* **2012**, *2*, 3190–3193. [[CrossRef](#)]
30. Yan, T.; Li, R.; Li, Z. Nickel–cobalt layered double hydroxide ultrathin nanoflakes decorated on graphene sheets with a 3D nanonetwork structure as supercapacitive materials. *Mater. Res. Bull.* **2014**, *51*, 97–104. [[CrossRef](#)]
31. Zheng, X.; Gu, Z.; Hu, Q.; Geng, B.; Zhang, X. Ultrathin porous nickel–cobalt hydroxide nanosheets for high-performance supercapacitor electrodes. *RSC Adv.* **2015**, *5*, 17007–17013. [[CrossRef](#)]
32. Li, M.; Ma, K.Y.; Cheng, J.P.; Lv, D.; Zhang, X.B. Nickel–cobalt hydroxide nanoflakes conformal coating on carbon nanotubes as a supercapacitive material with high-rate capability. *J. Power Sources* **2015**, *286*, 438–444. [[CrossRef](#)]
33. Li, H.; Musharavati, F.; Zalenezhad, E.; Chen, X.; Hui, K.N.; Hui, K.S. Electrodeposited NiCo layered double hydroxides on titanium carbide as a binder-free electrode for supercapacitors. *Electrochim. Acta* **2018**, *261*, 178–187. [[CrossRef](#)]
34. Li, J.; Wei, M.; Chu, W.; Wang, N. High-stable α -phase NiCo double hydroxide microspheres via microwave synthesis for supercapacitor electrode materials. *Chem. Eng. J.* **2017**, *316*, 277–287. [[CrossRef](#)]
35. Tao, Y.; Ruiyi, L.; Zaijun, L.; Junkang, L.; Guangli, W.; Zhiquo, G. A free template strategy for the fabrication of nickel/cobalt double hydroxide microspheres with tunable nanostructure and morphology for high performance supercapacitors. *RSC Adv.* **2013**, *3*, 19416–19422. [[CrossRef](#)]
36. He, S.; Li, Z.; Wang, J.; Wen, P.; Gao, J.; Ma, L.; Yang, Z.; Yang, S. MOF-derived $\text{Ni}_x\text{Co}_{1-x}(\text{OH})_2$ composite microspheres for high-performance supercapacitors. *RSC Adv.* **2016**, *6*, 49478–49486. [[CrossRef](#)]
37. Gou, J.; Xie, S.; Liu, Y.; Liu, C. Flower-like nickel-cobalt hydroxides converted from phosphites for high rate performance hybrid supercapacitor electrode materials. *Electrochim. Acta* **2016**, *210*, 915–924. [[CrossRef](#)]
38. Tao, Y.; Ruiyi, L.; Tingting, Y.; Zaijun, L. Nickel/cobalt layered double hydroxide hollow microspheres with hydrangea-like morphology for high-performance supercapacitors. *Electrochim. Acta* **2015**, *152*, 530–537. [[CrossRef](#)]
39. Chen, H.; Hu, L.; Chen, M.; Yan, Y.; Wu, L. Nickel–cobalt layered double hydroxide nanosheets for high-performance supercapacitor electrode materials. *Adv. Funct. Mater.* **2014**, *24*, 934–942. [[CrossRef](#)]
40. Tao, Y.; Zaijun, L.; Ruiyi, L.; Qi, N.; Hui, K.; Yulian, N.; Junkang, L. Nickel–cobalt double hydroxides microspheres with hollow interior and hedgehog-like exterior structures for supercapacitors. *J. Mater. Chem.* **2012**, *22*, 23587–23592. [[CrossRef](#)]
41. Zhang, J.; Cheng, J.P.; Li, M.; Liu, L.; Liu, F.; Zhang, X.B. Flower-like nickel–cobalt binary hydroxides with high specific capacitance: Tuning the composition and asymmetric capacitor application. *J. Electroanal. Chem.* **2015**, *743*, 38–45. [[CrossRef](#)]
42. Yang, M.; Cheng, H.; Gu, Y.; Sun, Z.; Hu, J.; Cao, L.; Lv, F.; Li, M.; Wang, W.; Wang, Z.; et al. Facile electrodeposition of 3D concentration-gradient Ni-Co hydroxide nanostructures on nickel foam as high performance electrodes for asymmetric supercapacitors. *Nano Res.* **2015**, *8*, 2744–2754. [[CrossRef](#)]
43. Lu, P.; Halvorsen, E.; Ohlckers, P.; Müller, L.; Leopold, S.; Hoffmann, M.; Grigoras, K.; Ahopelto, J.; Prunnila, M.; Chen, X. Ternary composite Si/TiN/MnO₂ taper nanorod array for on-chip supercapacitor. *Electrochim. Acta* **2017**, *248*, 397–408. [[CrossRef](#)]
44. Sun, X.; Wang, G.; Sun, H.; Lu, F.; Yu, M.; Lian, J. Morphology controlled high performance supercapacitor behaviour of the Ni–Co binary hydroxide system. *J. Power Sources* **2013**, *238*, 150–156. [[CrossRef](#)]
45. Gao, H.; Wang, G.; Yang, M.; Tan, L.; Yu, J. Novel tunable hierarchical Ni–Co hydroxide and oxide assembled from two-wheeled units. *Nanotechnology* **2011**, *23*, 015607. [[CrossRef](#)] [[PubMed](#)]
46. Wang, G.; Zhang, L.; Kim, J.; Zhang, J. Nickel and cobalt oxide composite as a possible electrode material for electrochemical supercapacitors. *J. Power Sources* **2012**, *217*, 554–561. [[CrossRef](#)]
47. Sun, Y.; Chen, L.; Wang, Y.; Zhao, Z.; Li, P.; Zhang, W.; Wang, Y.L.; Hu, J. Synthesis of MoO₃/WO₃ composite nanostructures for highly sensitive ethanol and acetone detection. *J. Mater. Sci.* **2017**, *52*, 1561–1572. [[CrossRef](#)]

48. Pu, J.; Tong, Y.; Wang, S.; Sheng, E.; Wang, Z. Nickel–cobalt hydroxide nanosheets arrays on Ni foam for pseudocapacitor applications. *J. Power Sources* **2014**, *250*, 250–256. [[CrossRef](#)]
49. Liu, F.; Chu, X.; Zhang, H.; Zhang, B.; Su, H.; Jin, L.; Wang, Z.; Huang, H.; Yang, W. Synthesis of self-assembly 3D porous Ni(OH)₂ with high capacitance for hybrid supercapacitors. *Electrochim. Acta* **2018**, *269*, 102–110. [[CrossRef](#)]
50. Xue, T.; Wang, X.; Lee, J.M. Dual-template synthesis of Co(OH)₂ with mesoporous nanowire structure and its application in supercapacitor. *J. Power Sources* **2012**, *201*, 382–386. [[CrossRef](#)]
51. Roy, A.; Jadhav, H.S.; Thorat, G.M.; Seo, J.G. Electrochemical growth of Co(OH)₂ nanoflakes on Ni foam for methanol electro-oxidation. *New J. Chem.* **2017**, *41*, 9546–9553. [[CrossRef](#)]
52. Jiang, C.; Zhao, B.; Cheng, J.; Li, J.; Zhang, H.; Tang, Z.; Yang, J. Hydrothermal synthesis of Ni(OH)₂ nanoflakes on 3D graphene foam for high-performance supercapacitors. *Electrochim. Acta* **2015**, *173*, 399–407. [[CrossRef](#)]
53. Jing, M.; Hou, H.; Banks, C.E.; Yang, Y.; Zhang, Y.; Ji, X. Alternating voltage introduced NiCo double hydroxide layered nanoflakes for an asymmetric supercapacitor. *ACS Appl. Mater. Interfaces* **2015**, *7*, 22741–22744. [[CrossRef](#)] [[PubMed](#)]
54. Wang, T.; Zhang, S.; Yan, X.; Lyu, M.; Wang, L.; Bell, J.; Wang, H. 2-Methylimidazole-derived Ni–Co layered double hydroxide nanosheets as high rate capability and high energy density storage material in hybrid supercapacitors. *ACS Appl. Mater. Interfaces* **2017**, *9*, 15510–15524. [[CrossRef](#)]
55. Fan, X.; Sun, Y.; Ohlckers, P.; Chen, X. Porous Thin-Wall Hollow Co₃O₄ Spheres for Supercapacitors with High Rate Capability. *Appl. Sci.* **2019**, *9*, 4672. [[CrossRef](#)]
56. Wu, J.; Mi, R.; Li, S.; Guo, P.; Mei, J.; Liu, H.; Lau, W.M.; Liu, L.M. Hierarchical three-dimensional NiCo₂O₄ nanoneedle arrays supported on Ni foam for high-performance supercapacitors. *RSC Adv.* **2015**, *5*, 25304–25311. [[CrossRef](#)]
57. Fan, X.; Ohlckers, P.; Chen, X. Tunable Synthesis of Hollow Co₃O₄ Nanoboxes and Their Application in Supercapacitors. *Appl. Sci.* **2020**, *10*, 1208. [[CrossRef](#)]
58. Cheng, Y.; Zhang, H.; Varanasi, C.V.; Liu, J. Improving the performance of cobalt–nickel hydroxide-based self-supporting electrodes for supercapacitors using accumulative approaches. *Energy Environ. Sci.* **2013**, *6*, 3314–3321. [[CrossRef](#)]
59. Hu, Z.A.; Xie, Y.L.; Wang, Y.X.; Wu, H.Y.; Yang, Y.Y.; Zhang, Z.Y. Synthesis and electrochemical characterization of mesoporous Co_xNi_{1-x} layered double hydroxides as electrode materials for supercapacitors. *Electrochim. Acta* **2009**, *54*, 2737–2741. [[CrossRef](#)]
60. Xie, L.; Hu, Z.; Lv, C.; Sun, G.; Wang, J.; Li, Y.; He, H.; Wang, J.; Li, K. Co_xNi_{1-x} double hydroxide nanoparticles with ultrahigh specific capacitances as supercapacitor electrode materials. *Electrochim. Acta* **2012**, *78*, 205–211. [[CrossRef](#)]
61. Liu, Y.; Fu, N.; Zhang, G.; Xu, M.; Lu, W.; Zhou, L.; Huang, H. Design of Hierarchical Ni–Co@Ni–Co Layered Double Hydroxide Core–Shell Structured Nanotube Array for High-Performance Flexible All-Solid-State Battery-Type Supercapacitors. *Adv. Funct. Mater.* **2017**, *27*, 1605307. [[CrossRef](#)]
62. Wang, Q.; Wang, X.; Liu, B.; Yu, G.; Hou, X.; Chen, D.; Shen, G. NiCo₂O₄ nanowire arrays supported on Ni foam for high-performance flexible all-solid-state supercapacitors. *J. Mater. Chem. A* **2013**, *1*, 2468–2473. [[CrossRef](#)]
63. Wang, Y.; Lei, Y.; Li, J.; Gu, L.; Yuan, H.; Xiao, D. Synthesis of 3D-nanonet hollow structured Co₃O₄ for high capacity supercapacitor. *ACS Appl. Mater. Interfaces* **2014**, *6*, 6739–6747. [[CrossRef](#)] [[PubMed](#)]
64. Tang, Y.; Liu, Y.; Yu, S.; Guo, W.; Mu, S.; Wang, H.; Zhao, Y.; Hou, L.; Fan, Y.; Gao, F. Template-free hydrothermal synthesis of nickel cobalt hydroxide nanoflowers with high performance for asymmetric supercapacitor. *Electrochim. Acta* **2015**, *161*, 279–289. [[CrossRef](#)]
65. Lu, P.; Ohlckers, P.; Müller, L.; Leopold, S.; Hoffmann, M.; Grigoras, K.; Ahopelto, J.; Prunnila, M.; Chen, X. Nano fabricated silicon nanorod array with titanium nitride coating for on-chip supercapacitors. *Electrochem. Commun.* **2016**, *70*, 51–55. [[CrossRef](#)]
66. Bai, X.; Liu, Q.; Zhang, H.; Liu, J.; Li, Z.; Jing, X.; Yuan, Y.; Liu, L.; Wang, J. Nickel-cobalt layered double hydroxide nanowires on three dimensional graphene nickel foam for high performance asymmetric supercapacitors. *Electrochim. Acta* **2016**, *215*, 492–499. [[CrossRef](#)]

67. Le, K.; Wang, Z.; Wang, F.; Wang, Q.; Shao, Q.; Murugadoss, V.; Wu, S.; Liu, W.; Liu, J.; Gao, Q.; et al. Sandwich-like NiCo layered double hydroxide/reduced graphene oxide nanocomposite cathodes for high energy density asymmetric supercapacitors. *Dalton Trans.* **2019**, *48*, 5193–5202. [[CrossRef](#)]
68. Cai, X.; Shen, X.; Ma, L.; Ji, Z.; Xu, C.; Yuan, A. Solvothermal synthesis of NiCo-layered double hydroxide nanosheets decorated on RGO sheets for high performance supercapacitor. *Chem. Eng. J.* **2015**, *268*, 251–259. [[CrossRef](#)]



© 2020 by the authors. Licensee MDPI, Basel, Switzerland. This article is an open access article distributed under the terms and conditions of the Creative Commons Attribution (CC BY) license (<http://creativecommons.org/licenses/by/4.0/>).

Article IV

Fan, X., & Chen, X. (2019). Facile synthesis of NFL-ZnWO₄ for pseudocapacitor applications. *MATEC Web of Conferences*, 272, 01005. DOI: 10.1051/matecconf/201927201005

Facile synthesis of NFL-ZnWO₄ for pseudocapacitor applications

Xiao Fan, and Xuyuan Chen*

Department of Microsystems, University of South-Eastern Norway, Campus Vestfold, Raveien 215, 3184Borre, Norway

Abstract. In this report, NFL-ZnWO₄ was synthesized by a hydrothermal route and investigated for application in supercapacitors for the first time. The physical and chemical characterizations of the prepared nanomaterial were analyzed by SEM, EDS, XRD and XPS, respectively. Supercapacitors study of CV, GCD and EIS revealed that NFL-ZnWO₄ exhibits good electrochemical properties. The high specific capacitance value of 107.7 F g⁻¹ was achieved at 5 mV s⁻¹. These findings demonstrated that ZnWO₄ could be a promising electrode material candidate and highly desirable for application of high property supercapacitors in the future.

1 Introduction

With the development of human society, a large amount of energy sources have been consumed, such as coal, petroleum, and natural gas [1]. Therefore, novel and suitable energy storage devices need to be developed. Supercapacitors(SCs), the new devices between conventional physical capacitors and lithium-ion batteries, have been extensively studied to serve as one of the most promising candidates for energy storage because of their high power density, long cycling lifespan and fast charge/discharge process [2]. In general, supercapacitors can be divided into two categories according to the energy storage mechanism: one is the electric double layer capacitors(EDLCs), in which carbonaceous materials have been widely utilized and the other is the Faradaic redox reaction pseudocapacitors(PsCs) usually containing transition metal oxides as the electrode materials [3]. In comparison with electric double layer capacitors, pseudocapacitors show much higher specific capacitance performance, making it is of far-reaching significance to focus research on [4].

So far, nanostructured metal oxides have been intensively explored in order to use them as electrode materials. However, the high cost of some transition metal oxides limited their practical use in commercial supercapacitors. Hence, searching for a low cost pseudocapacitive material and economically affordable generation systems has been a major challenge in supercapacitors research [5, 6]. In recent years, Zinc tungstate(ZnWO₄), an environmentally friendly low cost transition metal oxide and both its constituent elements being relatively earth-abundant [7], with high technological applications in

* Corresponding author: Xuyuan.Chen@usn.no

various fields, such as photocatalysts, optical fibers and gas sensors [8, 9], have been reported. Because both Zn and W elements can take part in the Faradaic redox reactions, ZnWO_4 is of great potential for electrode materials [10]. Unfortunately, ZnWO_4 is rarely reported as the composite materials for supercapacitors [11].

Herein, we employed a simple, facile and effective hydrothermal route to synthesize nanoflower-like ZnWO_4 (NFL- ZnWO_4) and to the best of our knowledge, there are no reports on this morphology. Moreover, its application in supercapacitors was systematically studied. The present results demonstrated the NFL- ZnWO_4 can be considered as a promising candidate for pseudocapacitor applications. In addition, to fulfill the increasing demands, a rational modification of ZnWO_4 nanostructure and compositing ZnWO_4 with other electrode materials are both advisable.

2 Experimental

2.1 Chemicals

Zinc nitrate hexahydrate ($\text{Zn}(\text{NO}_3)_2 \cdot 6\text{H}_2\text{O}$), sodium tungstate dehydrate ($\text{Na}_2\text{WO}_4 \cdot 2\text{H}_2\text{O}$), ammonium fluoride (NH_4F), hydrogen chloride solution, absolute ethanol, acetylene black, polyvinylidene fluoride (PVDF) and potassium hydroxide (KOH) were purchased from Sigma-Aldrich. All the chemicals were of analytical grade and were used as received without further purification.

2.2 Sample preparation

The ZnWO_4 was obtained by a simple and facile hydrothermal method. Briefly, 1 mmol of $\text{Zn}(\text{NO}_3)_2 \cdot 6\text{H}_2\text{O}$, 1 mmol of $\text{Na}_2\text{WO}_4 \cdot 2\text{H}_2\text{O}$, and 8 mmol of NH_4F were dissolved in 50 mL deionized (DI) water and stirred vigorously for 60 min to form a milky suspension. Then, the suspension was transferred into a Teflon-lined stainless steel autoclave. Subsequently, the sealed autoclave was heated at 120 °C for 8 h. After cooling to room temperature naturally, the collected precipitate was washed with DI water and dried at 90 °C for 12 h. Finally, the as-prepared product was heat treated at 600 °C for 6 h in a muffle furnace.

2.3 Electrodes fabrication

Before the fabrication, the nickel foam (NF) was carefully cleaned with 3 M HCl, absolute ethanol and DI water for 30 min in an ultrasonic bath, respectively, and dried in a vacuum oven at 50 °C. The working electrode was prepared by mixing an electro-active material, acetylene black and PVDF with a ratio of 75:15:10. The mixture were continuously grinded for 10 min in a mortar and pressed on NF finally.

2.4 Materials characterization

X-ray powder diffraction (XRD) characterization was performed using a DRIGC-Y 2000A with $\text{Cu-K}\alpha_1$ radiation ($\lambda = 1.5406 \text{ \AA}$) and the scanning speed was 6° min^{-1} . A Hitachi SU-3500 scanning electron microscope (SEM) equipped with an energy-dispersive X-ray spectrometer (EDS) was used to observe the morphologies and analyse the element compositions of material. X-ray photoelectron spectroscopy (XPS) measurement was carried out on an ESCALAB 250Xi.

2.5 Electrochemical measurement

Three-electrode system was employed to study the supercapacitor behavior of fabricated working electrode using a Zahner IM6 electrochemical workstation, in which Pt wire and Ag/AgCl (in saturated KCl) were used as a counter electrode and a reference electrode, respectively. Cyclic voltammogram(CV), galvanostatic charge/discharge(GCD) and electrochemical impedance spectra (EIS) measurements were conducted in 2M KOH electrolyte.

The gravimetric specific capacitance (C_s) based on CV is defined as

$$C_s(CV) = \frac{1}{2mv\Delta V} \int i(V)dV \quad (1)$$

The gravimetric specific capacitance based on GCD is given by

$$C_s(GCD) = \frac{It}{m\Delta V} \quad (2)$$

$\int i(V)dV$ is the integrated area of CV curve, and m , ΔV , v , I , t are the mass of active materials, potential window, scan rate, discharge current and discharge time.

3 Results and discussion

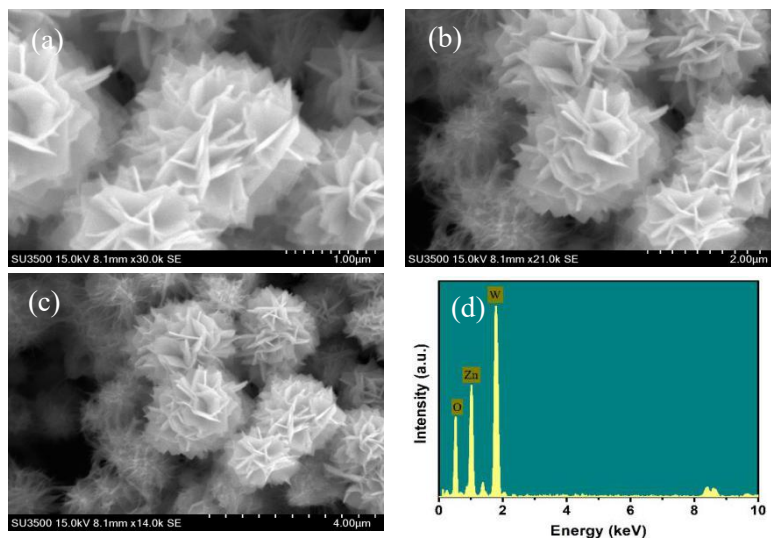


Fig. 1. SEM images(a-c) and EDS spectrum(d) of the synthesized $ZnWO_4$.

Figure 1a-c presents the typical SEM images with different magnification to illustrate the morphologies of the synthesized $ZnWO_4$. It clearly reveals that the $ZnWO_4$ exhibits a well-defined flower-like structure and was composed of layered and uniform nanoflakes. Meanwhile, the nanoflakes with diameters ranging from 1 to 2 μm intersect among each other. The macropores of the nanoflower structure, which are formed by stacking of the nanoflakes, are very suitable for ionic transport in the electrode of a supercapacitor [12]. In addition, the elemental composition was characterized by EDS, as shown in Figure 1d. The peaks correspond to O, Zn, and W elements. No other impurity element was observed, indicating the high purity of the samples.

The crystal structure of the obtained $ZnWO_4$ was analyzed by XRD, as shown in Figure 2. The obvious and typical reflection diffraction peaks correspond to (010), (100), (011), (110), (111), (021), (200), (121), (130), (-221) and (113) planes respectively. All the peaks can be indexed and well-matched to the monoclinic wolframite $ZnWO_4$ with the standard card (JCPDS card no.15-0774, space group $P2/c$), which also indicates that no other

impurities exist. Moreover, the strong and sharp peaks at (1 1 1), (1 0 0), and (0 2 1) planes suggest that the as-prepared ZnWO₄ samples are highly crystalline [13].

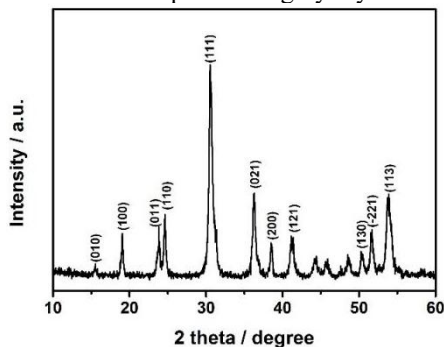


Fig. 2. XRD patterns of the as-prepared ZnWO₄ sample.

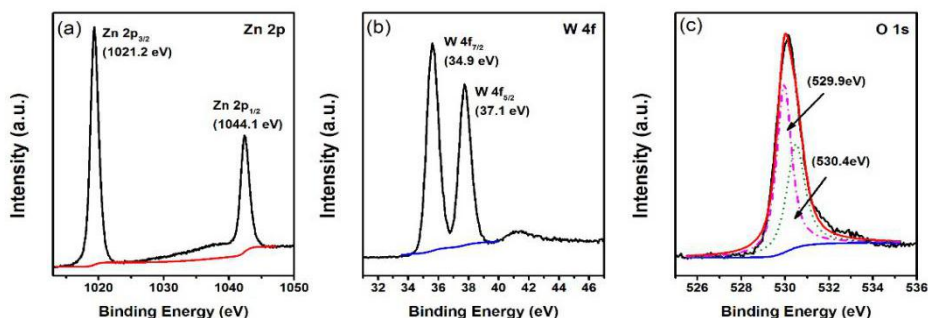


Fig. 3. High-resolution XPS survey spectra of ZnWO₄: (a) Zn 2p region, (b) W 4f region, and (c) O 1s region.

To further determine the elemental composition and chemical valance state, XPS was conducted on the ZnWO₄. The Zn 2p, W 4f, O 1s core-level XPS spectra of the ZnWO₄ are plotted in Figure 3. The Zn 2p_{3/2} and Zn 2p_{1/2} peaks at binding energies of ~ 1021.2eV and ~ 1044.1eV on a high resolution scan are shown in Figure 3a. This splitting is due to spin orbit coupling of Zn 2p states [8]. Similarly, Figure 3b illustrates the high-resolution spectrum of W 4f. The doublets of W 4f_{7/2} and W 4f_{5/2} peaks appears at binding energies of ~ 34.9eV and ~ 37.1eV respectively. Figure 3c displays the O 1s spectrum. The O 1s region can be fitted by two peaks located at ~ 529.9eV and ~ 530.4eV, which can be ascribed to the O²⁻ in the ZnWO₄ and hydroxyl groups on the surface of the sample [14]. All peaks at specific binding energies are well consistent with previous works [15] and clearly confirm the successful synthesis of ZnWO₄ nanomaterial.

The electrochemical performances of the fabricated electrode were deeply investigated. Figure 4a reveals the CV curves within the potential window of 0–0.5 V at various scan rates ranging from 5 to 100 mV s⁻¹. As expected, the CV at different scan rates exhibits a similar shape and a pair of strong redox peaks, which indicates the ideal capacitive behaviors and the capacitance characteristics are mainly governed by Faradaic redox reactions. This reaction is based on the reversible redox of Zn²⁺–Zn³⁺. The specific capacitance of 107.7 F g⁻¹ can be calculated by equation(1) at scan rate of 5 mV s⁻¹ further. Obviously, the anodic and the cathodic peaks shift to higher and to lower potentials with the increase of scan rate, respectively. It can be explained by the kinetic limitation of the redox reaction [16], which leads to a lower specific capacitance, as shown in Figure 4b.

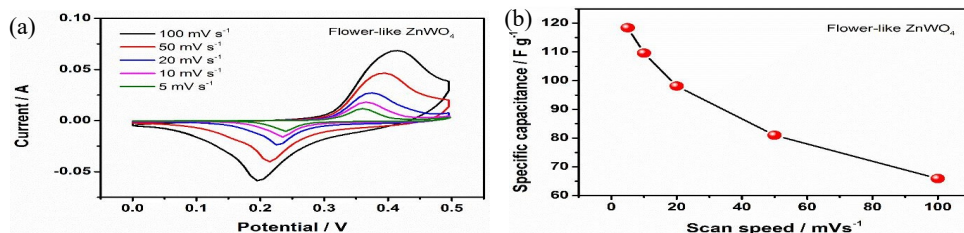


Fig. 4. (a) CV curves and (b) specific capacitance based on CV.

Figure 5a demonstrates the GCD measurements conducted at various current densities to get more information about the capacitive property. In comparison with a straight and flat line, the discharge curves displayed a significant deviation and plateau. It suggests the typical pseudocapacitive characteristics. Due to the incremental potential drop and the relatively insufficient active material involved in redox reaction under higher current densities [7], the specific capacitances achieved by equation(2) gradually decreases with the increase of current density, as can be observed from Figure 5b. The ions(OH⁻) at a low current density have adequate time to transfer at the interface between the electrode and electrolyte than at a high current density [5].

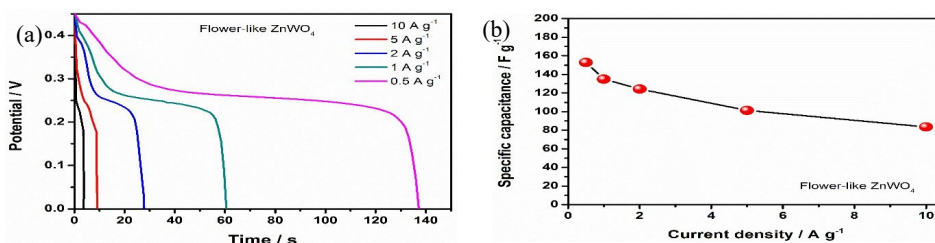


Fig. 5. (a) GCD curves and (b) specific capacitance based on GCD

EIS study was performed in Figure 6 to determine the conductive nature. At the high frequency regions, the Nyquist plot exhibits a negligible semicircle, suggesting a low charge transfer resistance and interfacial resistance between current collector and electroactive material [8]. In the low frequency regions, the plot presents a straight line with a quasi slope of 45°, indicating the more electrolyte ion diffusion to the electroactive materials [8]. In general, all features of the Nyquist plot declare the good conductivity and capacitive behavior.

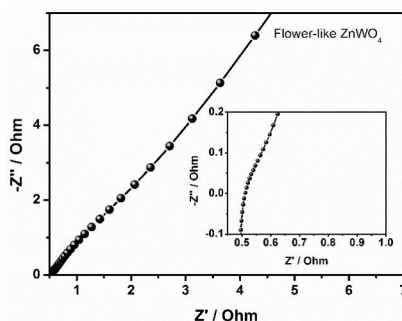


Fig. 6. EIS study.

4 Conclusion

In summary, a NFL-ZnWO₄ material with a unique and open-up network structure formed by interconnected nanoflakes was prepared via a hydrothermal method following an

appropriate heat treatment for the first time. The physical and chemical properties were carried out by SEM, EDS, XRD and XPS, respectively. A series of electrochemical tests including CV, GCD and EIS were conducted. It was demonstrated that the NFL-ZnWO₄ exhibits good electrochemical behaviors with a high specific capacitance of 107.7 F g⁻¹ at 5 mV s⁻¹. In the future, efforts of morphology tunings or synergies with other materials on ZnWO₄ can be made to match the superior electrochemical properties need. In view of this, ZnWO₄ as an electrode material is well worth being applied to supercapacitors.

Acknowledgements

Fruitful discussions with Professor Per Ohlckers and Professor Einar Halvorsen are acknowledged. Financial support from the Norwegian PhD Network on Nanotechnology for Microsystems sponsored by the Research Council of Norway, Division of Science is acknowledged. Financial support from the China Scholarship Council is acknowledged.

References

1. Pu J, Tong Y, Wang S, Sheng E and Wang Z 2014 *Journal of Power Sources*. **250** 250-256
2. Wang C, Zhou E, He W, Deng X, Huang J, Ding M, Wei X, Liu X and Xu X 2017 *Nanomaterials*. **7(2)** 41
3. Wang Q, Wang X, Liu B, Yu G, Hou X, Chen D and Shen G 2013 *Journal of Materials Chemistry A*. **1(7)** 2468-2473
4. Qiu M, Sun P, Shen L, Wang K, Song S, Yu X, Tan S, Zhao C and Mai W 2016 *Journal of Materials Chemistry A*. **4(19)** 7266-7273
5. Kumar R D, Andou Y and Karuppuchamy S 2016 *Journal of Physics and Chemistry of Solids*. **92** 94-99
6. Yang Y, Zhu J, Shi W, Zhou J , Gong D, Gu S, Wang L, Xu Z and Lu B 2016 *Materials Letters*. **177** 34-38
7. Guan B, Hu L, Zhang G, Guo D, Fu T, Li J, Duan H, Li C and Li Q 2014 *RSC Advances*. **4(9)** 4212-4217
8. Ede S R, Ramadoss A, Nithiyantham U, Anantharaj S and Kundu S 2015 *Inorganic chemistry*. **54(8)** 3851-3863
9. Shim H W, Cho I S, Hong K S, Lim A H and Kim D W 2011 *Journal of Physical Chemistry C*. **115(32)** 16228-16233
10. Luo L, Liu T, Zhang S, Ke B, Yu L, Hussain S and Lin L 2017 *Ceramics International*. **43(6)** 5095-5101.
11. Han S, Lin L, Zhang K, Luo L, Peng X and Hu N 2017 *Materials Letters*. **193** 89-92
12. Tang Y, Liu Y, Yu S, Zhao Y, Mu S and Gao F 2014 *Electrochimica Acta*. **123** 158-166
13. Huang Y, Gao Y, Zhang Q, Cao J J, Huang R J, Ho W and Lee S C 2016 *Applied Catalysis A: General*. **515** 170-178
14. Yu C and Jimmy C Y 2009 *Materials Science and Engineering: B*. **164(1)** 16-22
15. Khyzhun O Y, Bekenev V L, Atuchin V V, Galashov E N and Shlegel V N 2013 *Materials Chemistry and Physics*. **140(2-3)** 588-595
16. Lu P, Müller L, Hoffmann M and Chen X 2017 *Nano Energy*. **41** 618-625